7. VALIDATION

This section describes models and data used to validate the Drift Scale thermal-hydrological-chemical (THC) process model and input for the Drift Scale THC Seepage Model. The primary means of validation of the Drift Scale THC Seepage Model is the Drift Scale Test (DST) THC Model and the data collected from the DST. The DST THC Model and validation of model simulation results to measurements are presented in Section 7.1. The validation of the THC models by comparison to chemical data on water and gas samples is subject to a variety of uncertainties. These uncertainties are discussed in detail throughout Section 7, but can be summarized as follows. First, TH processes can lead to differences in the chemistry of water and gases by a few orders of magnitude (e.g., see Section 7.1.10.2) over very small increments in temperature as a result of boiling and mineral-water reactions. In contrast, temperature exhibits much less variation in space, because it is governed mainly by conduction in the rock matrix. Second, strong differences in aqueous species concentrations that develop in pore water in fractures and the adjacent matrix can be maintained owing to the slow rates of diffusion of aqueous species (e.g., see Section 7.1.11.3). Third, changes that the samples undergo during their extraction from the rock (e.g., cooling, degassing, condensation) have the potential for shifting the aqueous species compositions by a few orders of magnitude.

Reaction-transport experiments and associated modeling used to validate specific aspects of the Drift Scale THC models are presented in Sections 7.2 and 7.3. Sources of data used for model validation are shown in Table 7-1.

Table 7-1. Sources of Data Used for Model Validation or Corroboration

DTNs	Description
Plug Flow Reactor Data	
LB0011THCDISSX.001 [153380]	Experimental Data
Fracture Seal Experiment	
LB0101THCPRCPX.001 [154577]	Experimental data
Mineralogical Data (DST)	
LA0201SL831225.001 [158426]	Sidewall core sample mineralogical analyses
Analytical Water and Gas Chemistry Data	
LB0102CO2DST98.001 [159306]	CO_2 gas analyses (1st, 2nd, 3rd and 7th Qtr.)
LB990630123142.003 [111476]	4th, 5th, and 6th Qtr. DST CO_2 data
LB000121123142.003 [146451]	DST CO_2 data (Aug. '99 – Nov. '99)
LB0011CO2DST08.001 [153460]	DST CO_2 data (Nov. '99 – Aug. 2000)
CRWMS M&O 2001 [153814]	DST CO_2 data (July '98)
LB0208ISODSTHP.001 [161638]	DST CO_2 and isotopic data (combined)
MO0005PORWATER.000 [150930]	Analyses of pore waters from Alcove 5 core samples in the ESF (HD-PERM-2 and HD-PERM-3 samples)
LL990702804244.100 [144922]	Aqueous chemistry of water sampled from the DST (6/4/98 to 3/30/99)
LL001100931031.008 [153288]	Aqueous chemistry of water sampled from the DST (collected 10/27/99 to 1/25/00)

Table 7-1. Sources of Data Used for Model Validation or Corroboration (continued)

DTNs	Description
MO0207AL5WATER.001 [159300]	DST Field measurements
SN0203F3903102.001 [159133]	DST Field measurements
LL020405123142.019 [159307]	DST Aqueous chemistry
LL020302223142.015 [159134]	DST Aqueous chemistry
LL001200231031.009 [153616]	Aqueous chemistry of water sampled from the DST (8/9/99 and 8/10/99)
MO0101SEPFDDST.000 [153711]	Field pH of water sampled from DST on 5/23/00 and 6/29/00

7.1 THE DRIFT SCALE TEST THC MODEL

The DST is the second underground thermal test to be carried out in the Exploratory Studies Facility (ESF) at Yucca Mountain, Nevada. The purpose of the test is to evaluate the coupled thermal, hydrological, chemical, and mechanical processes that take place in unsaturated fractured tuff over a range of temperatures (approximately 25°C to 200°C). Details regarding the DST layout, borehole orientations, operation of the test, and measurements performed (as well as their uncertainties) are discussed in Section 6.3 of the *Thermal Testing Measurements Report* (BSC 2002 [160771]) and in *Drift Scale Test As-Built Report* (CRWMS M&O 1998 [111115]). Information on these aspects of the DST is not repeated in this report unless directly related to the geochemical data collected and used for model validation.

In brief, the DST consists of an approximately 50 m long drift that is 5 m in diameter. Nine electrical floor canister heaters were placed in this drift (the Heated Drift) to simulate nuclear-waste-bearing containers. Electrical heaters were also placed in a series of horizontal boreholes (wing heaters) drilled perpendicular outward from the central axis of the Heated Drift. These heaters were emplaced to simulate the effect of adjacent emplacement drifts. The DST heaters were activated on December 3, 1997, with a planned period of 4 years of heating, followed by 4 years of cooling. After just over 4 years, the heaters were switched off on January 14, 2002, and since that time the test area has been slowly cooling.

This section describes the DST THC Model, discusses simulations of THC processes during the DST, and presents comparisons to geochemical measurements performed on gas, water, and mineral samples collected from the DST. The DST THC Model is a forward numerical model used to gain insight into THC processes taking place during heating of the unsaturated devitrified tuffs. The DST THC Model provides the main validation test for the extension of the Drift-Scale THC conceptual model to the Drift Scale THC Seepage Model. The Drift-Scale THC conceptual models are described in Sections 6.1 to 6.4. The DST THC Model is compared with, but not calibrated to geochemical data collected from the DST. The calibrated drift-scale hydrological properties and thermal properties used as inputs are based on Yucca Mountain site data and not data specific to the DST. Some modifications were made to the thermodynamic data to capture aspects of the ambient-system pore-water chemistry (discussed in Section 4.1.4). The rationale for using hydrological and thermal properties that are not specific to the DST is discussed in Section 7.1.1. Model adjustments specific to the DST are made only to the connectivity of the

Heated Drift to the Access Drift, in order to capture (approximately) the heat losses through the bulkhead separating these tunnels.

Processes and data collected primarily during the heating phase of the DST are discussed in this Model Report. Simulation results from the DST THC Model REV01 were compared to the first 32 months of measured gas and water chemistry data. REV02 simulations build on the sensitivity studies and analyses performed for REV01, and therefore most REV01 sensitivity simulations were not repeated for REV02. REV02 simulation results are compared to data from the full four-year heating phase (for data that are available) as a part of the model validation.

The DST is not yet complete; it is expected that additional test data, when available, could provide further support to model validation. Specifically, model validation activities are expected to extend beyond the documented completion date for this Model Report, for several reasons. First, this Model Report predominantly treats data collected during the heating phase of the DST, and it is important to extend model validation to include data from the cooling phase with associated modeling. Second, analyses of new cores drilled through the boiling zone are underway, and other boreholes designed specifically for chemical analyses have not been completed. These will provide a much more complete validation for mineral deposition in fractures and compositions and quantities of water imbibed into the rock matrix. Third, there are additional stable and radiogenic isotopic data that have not yet been fully incorporated into the conceptual/numerical models describing THC processes. Such models and data will provide alternative validation methods for assessing the model's ability to represent TH and THC processes in the DST. Although new information and data from the DST will strengthen the model validation, this section will provide numerous comparisons of mineral, water, and gas chemistry that document that the validation criteria have been met.

7.1.1 Modeling Approach

The objectives of this work were to make predictions of the coupled thermal, hydrological, and chemical processes, followed by model refinement and comparison to measured data. The DST THC Model is not calibrated to geochemical measurements from the DST. Comparisons to measured geochemical data are the main method used in this Model Report for model validation. However, a better understanding of coupled processes is more important than matching all measured data, so that the models can be applied to long-term predictions of near-field THC processes. Furthermore, the simulations performed with the DST THC Model did not use site-specific (from the DST test block) thermal or hydrological properties. Therefore, the model provides a good test of whether site-wide hydrological and thermal properties can adequately capture processes that may take place at a specific location.

The modeling approach involves the creation of a numerical grid, as well as the selection and/or development of thermal, hydrological, mineralogical, aqueous, and gaseous species geochemical input data. It also involves the selection of appropriate thermal and hydrological models, as well as chemical, thermodynamic, and kinetic data and models. The approach and input data are described as follows in Sections 7.1.2 to 7.1.5.

7.1.2 Drift Scale Test 2-D Numerical Grid

The two-dimensional dual-permeability numerical grid for the DST represents a vertical cross section through the Heated Drift at a distance approximately 30 m from the bulkhead, separating the Heated Drift from the Access Drift (Figure 7.1-1a).

The REV01 mesh consists of 4,485 gridblocks, including fracture and matrix (DTN: LB0101DSTTHGRD.001 [153687]) (Figure 7.1-1b). The top boundary is approximately 99 m above the drift center, with the bottom boundary at approximately 157 m below the center. Connections between the interior of the Heated Drift and the Heater Test Alcove included gridblocks designed to act as a bulkhead and as insulating material. Within the drift, heat is applied directly to the drift wall instead of explicitly representing the electric heaters and calculating the heat transfer across the air mass inside the drift. The DST includes a plane of linear wing heaters on each side of the drift that are given small gridblocks in the model. Small gridblocks are also employed adjacent to the wing heaters and drift wall to capture the strong gradients in temperature and liquid saturation in these regions (Figure 7.1-1c). Radial mesh blocks in the drift interior were removed from the original mesh and replaced near the drift base by Cartesian gridblocks to represent the concrete invert (Figure 7.1-1c).

Minor modifications to the REV01 mesh were made for REV02 simulations. Gridblocks representing the insulation/bulkhead were removed, and the Heated Drift gridblock was connected directly to the Heater Test Alcove gridblock. The connection area and distance were adjusted so that heat loss from the drift resulted in roughly similar crown temperatures to the maximum observed values. This was done to simulate heat and mass losses through the bulkhead, instead of reducing power by a set factor, as was done in the REV01 simulations. In the approximate location of the observation drift, the gridblock volumes were increased to a large value to represent connection to the atmosphere (Figure 7.1-1b). Gridblocks that were removed previously (to represent a no-flux boundary for the observation drift) were added and connected to adjacent gridblocks. The distances from the drift center gridblock and the connecting elements were modified to represent the true distance, so that heat could be applied to the drift center and not to the elements at the drift walls (method used in REV01).

7.1.3 Heater Power

The DST THC Model employs a 9-month initial period at ambient temperature, corresponding approximately to the time that was required to set up the test. The wing heaters are split into inner and outer zones, with more power applied to the outer zone to approximate the presence of an adjacent parallel drift. In REV01, heat was applied at the drift wall into small gridblocks. In REV02, heat was applied solely to the drift-center gridblock, which is connected to all surrounding gridblocks. The positions of gridblocks representing heaters are shown in Figure 7.1-1c.

The REV01 heating schedule employed in the simulations is based on calibrated heater power measurements from DTN: MO0007SEPDSTPC.001 [153707]. The REV01 simulations were started with a 10% lower baseline power output to account for approximate differences between a 2-D model and heat losses in a 3-D experiment. Three 5% reductions in power during the year 2000 were implemented in the simulations, based on the estimated power reductions (DTN:

MO0012SEPDSTPC.002 [153708]). These simulations included 9 months at ambient temperature followed by 3 years of heating.

The REV02 heating schedule was based on step-wise averages of the 10-day incremented power data (DTN: MO0208RESTRDST.002 [161129]). The sources for this 10-day incremented power data are given in Table 7.1-1. The step-wise power distribution reflects the power output more closely than the simple averages used in REV01. Intentional power reductions were directly accounted from the power data, and more accurate time information gathered from the DTNs listed in Table 7.1-1.

Table 7.1-1. Input DTNs Used for Estimating Times/Dates of Power Reductions and Outages for REV02 Simulations

Power Data Sources	Dates
MO0208RESTRDST.002 [161129]	Heating Phase (10-day increments)
MO9807DSTSET01.000 [113644]	11/7/97 – 5/3/98
MO9810DSTSET02.000 [113662]	6/1/98 – 8/31/98
MO9906DSTSET03.000 [113673]	9/1/98 – 5/31/99
MO0001SEPDSTPC.000 [153836]	6/1/99 – 10/31/99
MO0007SEPDSTPC.001 [153707]	11/1/99 – 5/31/00
MO0012SEPDSTPC.002 [153708]	6/1/00 – 11/30/00
MO0107SEPDSTPC.003 [158321]	12/1/00 – 5/31/01
MO0202SEPDSTTV.001 [158320]	6/1/01 – 1/14/02

The DTNs in Table 7.1-1 were also used to estimate the length of the longer (approximately greater than 1/2 day) temporary power outages. Table 7.1-2 gives the step-wise averaged power data implemented in the REV02 DST THC Model simulations. Each time in Table 7.1-2 represents the initiation of a specific period of heating or power loss that continues until the succeeding time. The simulations were run for the full period of heating plus a 4-year period of cooling (shown by hypothetical end time at the base of Table 7.1-2).

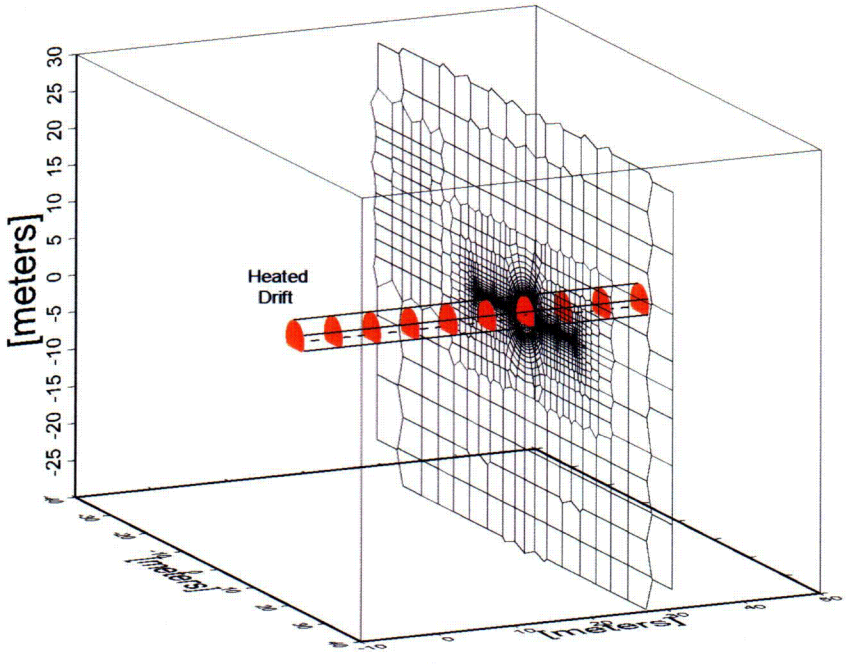

Output-DTN: LB0307DSTTHCR2.001

Figure 7.1-1a. Three-Dimensional Schematic Diagram of the DST Showing Perspective View of Numerical Mesh for DST THC Model Simulations (Mesh Extends In All Directions from Area Shown)

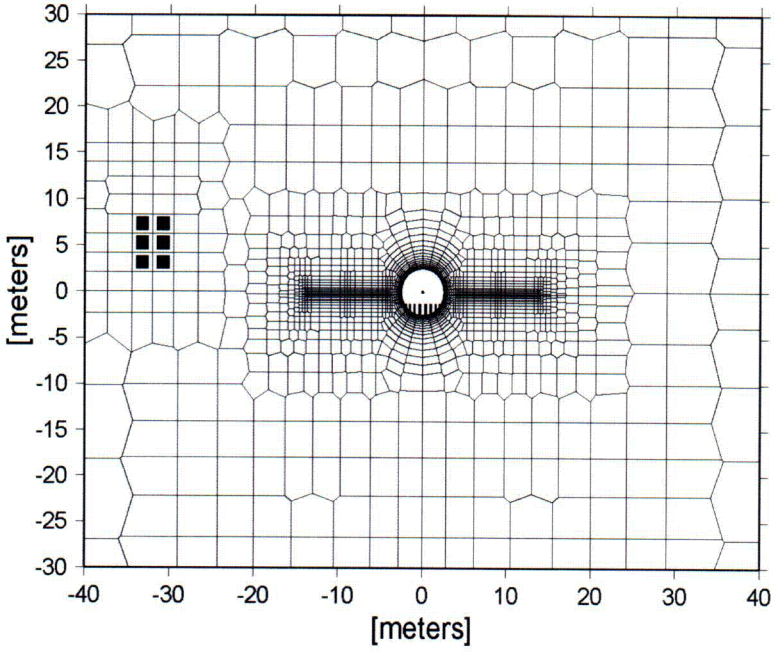

Output-DTN: LB0307DSTTHCR2.001

NOTE: The Observation Drift is shown as black squares. Mesh extends outside the area shown (see text). The Heated Drift is a circular region at the center.

Figure 7.1-1b. Numerical Mesh for DST THC Model Simulations

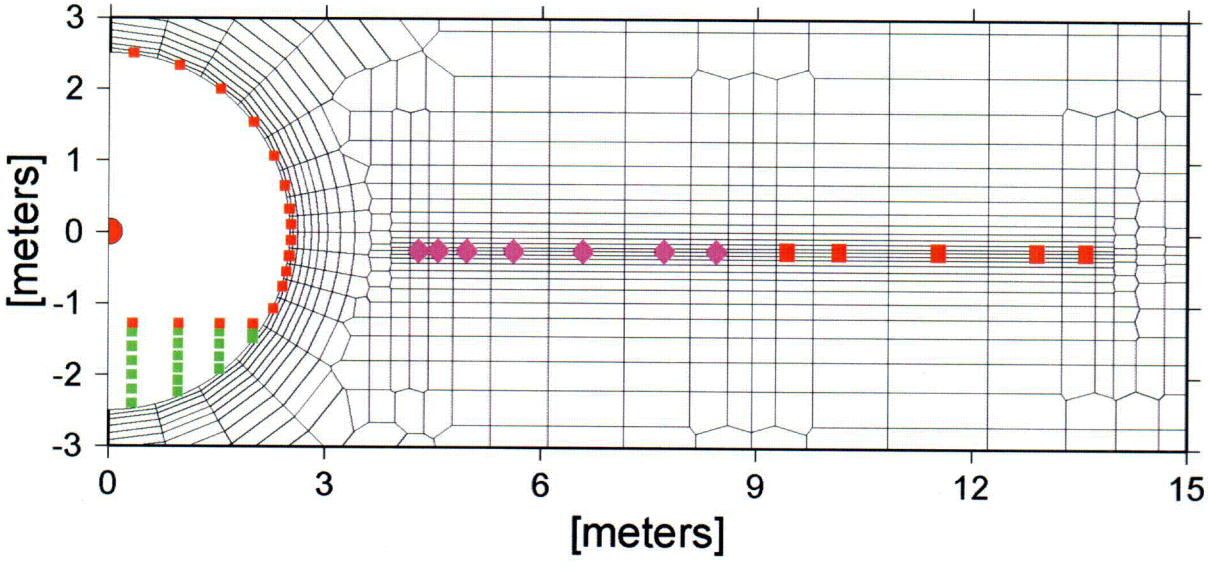

Output-DTN: LB0307DSTTHCR2.001

NOTE: Inner (violet diamonds closer to drift) and outer wing heater (red squares) indicate gridblock coordinates. Heat was applied to gridblocks marked along inside of drift for REV01, and at drift center for REV02. Green squares indicate gridblock locations for the concrete invert.

Figure 7.1-1c. Enlarged View of the Numerical Grid Showing the Locations of Gridblocks Representing the Heated Drift, Wing Heaters, and Concrete Invert

C101

Table 7.1-2. Step-Wise Averaged Power Data for REV02 Simulations

Date	Time (s)	Time (days)	Canister Power (watts)	WH (Inner) Power (watts)	WH (outer) Power (watts)	Comments
3/5/97	0.00000E+00	0.00	0.0000	0.0000	0.0000	pre-test
12/3/97	2.35872E+07	273.00	1091.3740	1232.4007	1626.7690	heaters turned on
3/15/98	3.24000E+07	375.00	1091.3740	0.0000	0.0000	outage - right rib
3/16/98	3.25080E+07	376.25	1091.3740	1232.4007	1626.7690	
4/12/98	3.48192E+07	403.00	1077.9972	1198.5773	1582.1220	
8/10/98	4.51872E+07	523.00	1119.6842	1201.8035	1586.3807	
1/27/99	5.98752E+07	693.00	0.0000	0.0000	0.0000	power outage
1/27/99	5.99400E+07	693.75	1123.5789	1204.4465	1589.8693	
2/16/99	6.16032E+07	713.00	1102.5965	1189.0805	1569.5862	
5/27/99	7.02432E+07	813.00	0.0000	0.0000	0.0000	power outage
5/27/99	7.03080E+07	813.75	1102.5965	1189.0805	1569.5862	
5/29/99	7.04160E+07	815.00	0.0000	0.0000	0.0000	power outage
5/30/99	7.04808E+07	815.75	1087.8653	1155.5245	1525.2923	
6/18/99	7.21440E+07	835.00	0.0000	0.0000	0.0000	power outage
6/19/99	7.22088E+07	835.75	1087.8653	1155.5245	1525.2923	
7/9/99	7.39584E+07	856.00	0.0000	0.0000	0.0000	power outage
7/15/99	7.44768E+07	862.00	1087.8653	1155.5245	1525.2923	
8/27/99	7.81920E+07	905.00	0.0000	0.0000	0.0000	power outage
8/29/99	7.83216E+07	906.50	1087.8653	1155.5245	1525.2923	
11/22/99	8.57088E+07	992.00	1087.8653	0.0000	0.0000	outage - right rib
11/24/99	8.58816E+07	994.00	1087.8653	1155.5245	1525.2923	
2/11/00	9.27072E+07	1073.00	0.0000	0.0000	0.0000	power outage
2/11/00	9.27720E+07	1073.75	1078.8421	1184.6642	1563.7568	
3/2/00	9.44352E+07	1093.00	1029.1930	1115.3660	1472.2831	power reduction
3/12/00	9.52992E+07	1103.00	0.0000	0.0000	0.0000	power loss
3/13/00	9.54072E+07	1104.25	1029.1930	1115.3660	1472.2831	
5/2/00	9.97056E+07	1154.00	964.5263	1040.2813	1373.1713	power reduction
8/15/00	1.08778E+08	1259.00	917.3463	978.7397	1291.9364	power reduction
1/20/01	1.22429E+08	1417.00	0.0000	0.0000	0.0000	power outage
1/21/01	1.22515E+08	1418.00	917.3463	978.7397	1291.9364	
5/1/01	1.31155E+08	1518.00	875.5711	925.4672	1221.6168	power reduction
7/1/01	1.36426E+08	1579.00	0.0000	0.0000	0.0000	power outage
7/1/01	1.36490E+08	1579.75	875.5711	925.4672	1221.6168	
8/22/01	1.40918E+08	1631.00	826.8171	875.8317	1156.0979	power reduction
1/14/02	1.53446E+08	1776.00	0.0000	0.0000	0.0000	heaters turned off
1/14/06	2.79677E+08	3237.00	0.0000	0.0000	0.0000	cooling period end

NOTE: Input DTNs for REV02 power data are listed in Table 7.1-1. Each time represents the initiation of a particular period of heating (or power loss) that continues until the next time in the table. Data are for a 2-D vertical slice.

7.1.4 Hydrological and Geochemical Input Data

Sources of hydrological and geochemical input data are listed in Table 4.1-1 (REV02) and 6.4-2 (REV01). Other details regarding the use or modifications to these data are given in Sections 7.1.5 and 7.1.6.

Thermodynamic data are described in Section 4.1.4 and presented in Attachments V (REV01) and VI (REV02). Kinetic data are given in Table 6.4-3 (REV01) and Table 4.1-4 (REV02). Initial mineral volume fractions for REV01 simulations are given in Attachment I. REV02 mineral volume fractions were modified slightly to reflect the mineralogical assemblage used in the Tptpll THC Seepage Model REV02, i.e., the addition of fluorite and opal to the initial assemblage. In REV02, the mineral names were also modified to be consistent with the name conventions used in the REV02 thermodynamic database. Mineral reactive surface areas are given in Attachment III, again with slight modification to reflect additional minerals in REV02.

7.1.5 Initial and Boundary Conditions: Hydrological and Thermal

Hydrological and thermal initial and boundary conditions were derived from the UZ Flow Model. Input data to these models (hydrological and thermal properties) are qualified and have been taken from the TDMS, and the UZ Flow Model has been calibrated to these data. Models and data for the ambient geochemistry of the UZ at Yucca Mountain (i.e. Cl, Sr, calcite) support the infiltration rates used as boundary conditions for the UZ Flow and Transport Model (Sonnenthal and Bodvarsson 1999 [117127], p. 107; Liu et al. 2003 [162470]; Xu et al. 2003 [162124]). This confidence in the initial and boundary conditions in turn provides confidence in the DST THC model. The methods used to set the initial and boundary conditions are described immediately below.

For REV01 simulations, the steady-state liquid saturations, temperatures, and pressures were obtained using the calibrated drift-scale hydrological parameter set for the present climate (mean infiltration) with a local infiltration rate of 1.05 mm/yr (DTN: LB991091233129.001 [125868]). The REV01 hydrological properties are listed in Table 6.4-1.

Steady-state liquid saturations, temperatures, and pressures were obtained for REV02 simulations using the updated drift-scale thermal-hydrological property set (DTN: LB0208UZDSCPMI.002 [161243]). The REV02 hydrological properties are listed in Table 6.4-1. Modifications were made to the fracture medium void fraction (usually set to 0.99 or 1.0) to be consistent with the revised REV02 fracture porosities (DTN: LB0210THRMLPRP.001 [160799]). This modification has approximately the same effect as changing the relative volumes of the fracture and matrix gridblocks (the usual procedure for implementing fracture porosity).

The top and bottom boundaries were set to constant temperature, pressure, and liquid saturation, based on steady-state values obtained from simulations of a 1-D column extending from the land surface to the water table. The top boundary of the 2-D model extends 150 m above and below the drift center, but does not reach either the land surface or the water table. Under these conditions, the percolation flux at the top boundary is approximately 0.5 mm/yr. The bottom boundary condition is open to gas and to liquid flow. The side boundaries of the domain are located 81.5 m away from the drift center on each side (outside of the test influence area) and are

no-flux for mass and heat. The air pressure and temperature in the observation drift are set to constant values, and therefore do not reflect temporal fluctuations in barometric pressure or tunnel air temperatures. The Heated Drift wall is open to advection and conduction of heat and mass (e.g., air, water vapor, and CO_2).

7.1.6 Initial and Boundary Conditions: Geochemical

Initial and boundary geochemical conditions were set using qualified data, based on pore water and mineralogical analyses and taken from the TDMS. Because these data are qualified, this confidence in the initial and boundary conditions in turn provides confidence in the DST THC model. The methods used to set the initial and boundary conditions are described immediately below.

Initial geochemical data used in the simulations are given in Attachments I–VI (sources in Tables 4.1-1 and 6.4-2). All aqueous and gaseous species concentrations in the rock were initially set to a uniform value (Section 6.2.2.1). The Heater Alcove and Observation Drift CO_2 concentrations were fixed to approximately that of the atmosphere. The Heated Drift CO_2 concentration was initially set to the same value as that in the Observation Drift, but was allowed to exchange CO_2 with the Heater Test Alcove and with the surrounding rock. REV01 simulations were run using the extended-case and base-case geochemical systems described in Section 6.2.2.2 and in Table 6.2-2. REV02 simulations were performed with the updated REV02 extended-case geochemical system (Table 6.2-2).

Both the top and bottom boundary conditions are open to gas and aqueous species transport. The top and bottom boundaries were also set so that no mineral reactions take place (and therefore no changes in aqueous species concentrations occur as a result of mineral-water reactions). Their volumes were set to extremely large values, so that they act essentially as constant concentration boundaries. The side boundaries are no-flux for gas and aqueous-species transport.

7.1.7 Model Validation Methods, Criteria, and Limitations

In the following sections, data and predictions are reviewed to demonstrate that the criteria specified in the TWP have been met for the DST THC Model. Because the THC Seepage Model uses the same conceptualization and mathematical treatment of THC coupled processes as the DST THC Model, including the same thermodynamic and kinetic data, DST model validation effectively validates the THC Seepage Model. Additional validation of the THC model is presented in Sections 7.2 and 7.3, where results of laboratory plug-flow and fracture boiling experiments are compared to simulations. It is important to recognize that although the DST THC Model validates the methodology and inputs used in the THC Seepage Models, the time-scales of interest are different by several orders of magnitudes and thus the relative importance of various reaction-transport processes can lead to different long-term behavior.

The models were validated—that is, needed confidence in the models was gained—by the following methods listed in AP-SIII.10Q, Section 5.4.1 (c). These are: Method 1, Corroboration with Experimental Data; and Method 3, Corroboration with Refereed Journal Literature (AP-SIII.10Q, 5.4.1(d)). These validation methods provide the most confidence in the conceptual and numerical models and their outputs.

While this model report has been independently reviewed under LBNL procedure, YMP-LBNL-QIP-6.1, *Document Review* as planned in the TWP (BSC 2002 [160819], Section 2.8 and Attachment I, Section I-3-4-1), this review is not considered to be one of the methods of validation for this model report.

7.1.7.1 Validation Method 1—Corroboration with Experimental Data

Data from the DST used for comparison consist of analyses of water and gas samples from borehole intervals between packers and observations of mineral precipitation in boreholes. Intervals were selected for comparison based upon the availability of a long, continuous sample record and the absence of confounding factors, such as the sampling interval being too long to compare with a particular gridblock or pair of gridblocks, or boreholes being near either end of the DST and affected by three-dimensional transport (see below). The locations of the hydrology boreholes, sampling intervals, and temperature sensors are shown in Figure 7.1-2.

Differences between the DST THC Model predictions and the DST measurements are important to this validation. There are several reasons (listed below) why observations may disagree with predictions, and yet be consistent with validation of the DST THC Model. Individual data points may not agree closely with model predictions, but model validation requirements can be met. It is important that these considerations are kept in mind when reviewing the model comparisons to measured data.

1. The DST THC model is a continuum model, using average hydrological, thermal, and mineralogical properties for individual hydrostratigraphic units at Yucca Mountain, rather than specifically for the DST.

2. The continuum model does not simulate individual fractures, which may intersect boreholes near sampling points, their aperture and frequency resulting in different flow rates and temperatures, thus affecting the chemistry of the gas and water samples in that interval.

3. All samples were taken from long borehole intervals (approximately 8-10 m long), which cross regions of large gradients in gas species concentrations (up to a few orders of magnitude) and exhibit temperature variations of tens of degrees. Furthermore, the samples are only known to have been derived from the borehole itself and may not have the same composition as the gas and liquid flowing in fractures. In addition, waters collected from boreholes have resided in the boreholes for different lengths of time, interacting with the surface of the borehole, interchanging components with the matrix, affected by gas flow and condensation in the borehole, and interacting with engineered materials. In contrast, the model results represent compositions in fractures or matrix at an instant in time.

4. The model represents a two-dimensional slice taken approximately at mid-length of the DST; it does not simulate transport in the third dimension. A 3-D model at the minimum resolution required for a reactive-transport simulation would have in excess of 100,000 gridblocks, which would be computationally infeasible (several months or more of computation time). Because the initial permeabilities and geochemical

properties are unknown at every point inside the rock, a 3-D model would not be expected to significantly improve matches to geochemical data, because the model would still rely on average properties. Although a 3-D model would reduce some of the uncertainty because of slight improvements in capturing the distribution of heat, fluid, and chemical species transport, it would not yield any significant improvement in the conceptual understanding or validation of the model approach and input data.

5. The model does not consider all deviations from planned operation. These deviations include the exact time periods of power losses, variations or uncertainty in heat losses through the bulkhead, changes in pressure owing to forced ventilation, the effect of the many boreholes on the behavior of the system, and barometric pressure changes. Because of this, and reasons 1, 2, and 4 above, the changes occurring at a particular time in the model may be shifted from that occurring in the DST by several months or more, depending on the time when the temperatures are similar or the point at which water completely evaporates.

6. Gas and water samples are affected by condensation of water vapor as the sample cools in the collection tubes from the borehole interval to the sample containers. This results in a variety of changes to the gas and water compositions. CO_2 concentrations in the gas can increase dramatically as the water vapor is preferentially removed from the gas. Many aqueous species concentrations will become lower as the sample is diluted by pure water condensed in the tubes and mixed with the water being sampled. The pH of the water may drop as the pure condensate formed under an elevated partial pressures of CO_2 is mixed with the water from the borehole.

Given these considerations, and the model requirements in mind, the criterion for model validation is that any two of these three criteria be satisfied for a majority of the samples collected (but not all samples if conditions as given above are expected to be important):

- Observed concentrations of gas and aqueous species match predicted concentrations within an order of magnitude (e.g., one pH unit). This range is reasonable because chemical potential is proportional to the logarithm of concentration.

- The simulated trend of CO_2 over time in the sampling interval is clearly followed. "Clearly followed" is understood to mean that model and observations show the same initial trend of increase or decrease, and any observed reversal is predicted. Simulated CO_2 concentrations will be within one order of magnitude of measured data

- Observations of mineral precipitation shall agree qualitatively with predictions of locations where mineral precipitation is most likely to occur.

7.1.7.2 Validation Method 3—Corroboration with Refereed Journals or Literature

This validation has been corroborated by publication in a refereed technical journal as allowed by AP-SIII.10Q, Section 5.4.1(d) (Xu et al. 2001 [161864]).

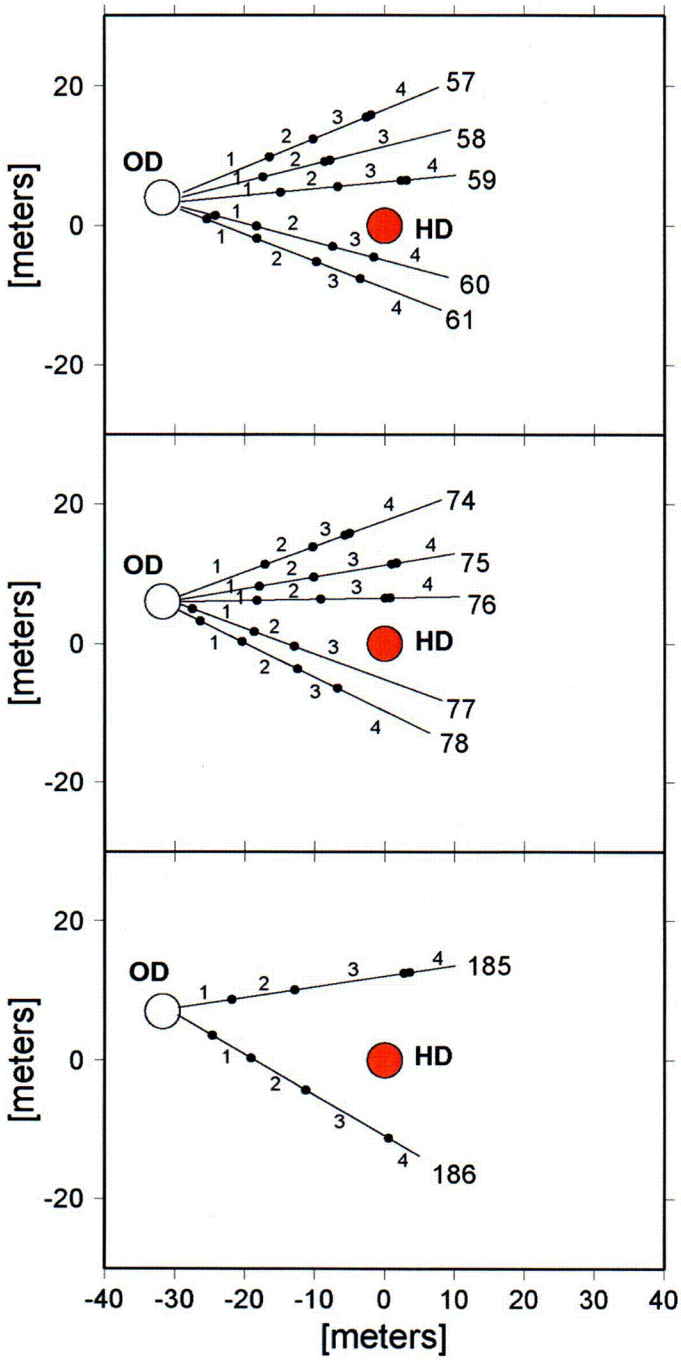

(coordinates from DTN: MO0002ABBLSLDS.000 [147304])

NOTE: Borehole intervals are designated as 1, 2, 3, and 4 moving away from the Observation Drift (open circle designated "OD"). Temperature sensors (not labeled) are shown as the small closed circles, and are designated similarly to the intervals (i.e., sensor 60-4 is the 4th sensor from the Observation Drift).
OD = Observation Drift; HD = Heated Drift.

Figure 7.1-2. Locations of Hydrology Boreholes, Sampling Intervals (numbered) and Temperature Sensors

C102

7.1.8 THC Simulations

In the following sections, simulations performed for REV01 and REV02 of this Model Report are described. Several sensitivity runs were performed for REV01 that show the effects of changing various geochemical model parameters. In REV02, other sensitivity simulations were performed to complement those done in REV01. In some cases where the results are similar to those presented for REV01, only REV02 simulation results are shown, with discussion on any differences observed. The specific updates and simulations are listed in the following subsections.

7.1.8.1 REV01 Simulations

Six THC simulations of the DST were performed to investigate various aspects of the DST THC model thermodynamic and kinetic data and conceptual models for mineral reactions. All REV01 simulations were performed using TOUGHREACT V2.3 (LBNL 2001 [153101]). All were run for 9 months of ambient open-drift conditions, followed by 3 years of heating. The maximum time step was one day, using the sequential noniterative approach. Coupling of permeability to fracture aperture changes was employed; however, the changes to flow are very minor over the short time of the DST. Based on differences in the geochemical system and treatment of important mineral reaction rates, the simulations are designated in the figures as follows:

1. Base-case CC Kin: Base case, including fluorite (Table 6.2-2). Calcite (CC) is treated as a kinetic mineral with the published value of the kinetic-rate constant.

2. Extended CC Kin: Extended case (Table 6.2-2, includes aluminosilicates and iron oxides). Calcite is treated as a kinetic mineral with the published value of the kinetic rate constant.

3. Base-case CC Eq: Base case, including fluorite. Calcite is treated as an equilibrium mineral.

4. Extended CC Eq: Extended case. Calcite is treated as an equilibrium mineral.

5. Extended An Full: Extended case. The full reactive surface area is used for anorthite (1000 times larger than in (2) and (4) above). Calcite is treated as a kinetic mineral with the published value of the kinetic rate constant.

6. Base-case No CC: Base case, including fluorite. Calcite was removed from this simulation to address observations of lower pH waters that may have condensed in or near the walls of boreholes where water was collected without interacting with calcite.

All input and output data files for the REV01 simulations are given in Attachment X.

7.1.8.2 REV02 Updates and Simulations

Several updates were made for the simulations in REV02 of this Model Report. They include:

1. Revisions to the numerical mesh to account for heat input at the drift center and heat and mass transfer across the Heated Drift and Observation Drift walls (see Section 7.1.2).

2. Revision of input heater power (see Section 7.1.3).

3. Use of REV02 calibrated thermal-hydrological properties (see Table 6.4-1).

4. Use of REV02 thermodynamic data (see Attachment VI).

5. Use of REV02 kinetic data (see Section 4.1.5 and Table 4.1-4).

6. Added nitrate to aqueous species (see HD-PERM water, Table 6.2-1).

7. Added fluorite and opal to the primary mineral assemblage and sepiolite as a potential precipitating phase (see Section 6.2.2.2 and Table 6.2-2).

8. Added various salt minerals as potential precipitating phases (or as phases formed during flow into dry blocks; see Section 6.4.5).

9. Use of an improved method for mineral precipitation at the boiling front that was implemented in TOUGHREACT V3.0 (LBNL 2002 [161256]).

Three additional THC simulations and two TH simulations were performed for REV02 of this Model Report using TOUGHREACT V3.0 (LBNL 2002 [161256]).

1. Extended Case (REV02), EOS3, higher CO_2 diffusion coefficient (value used in most REV02 THC Seepage Model simulations) [simulation dstrev2_thc7].

2. Extended Case (REV02), EOS4, REV01 CO_2 diffusion coefficient [simulation dstrev2_thc8].

3. Extended Case (REV02), EOS3, REV01 CO_2 diffusion coefficient [simulation dstrev2_thc9].

4. EOS3 TH simulation [simulation dstrev2_th12].

5. EOS4 TH simulation [simulation dstrev2_th13].

The REV02 extended-case geochemical system was used for all THC simulations performed for REV02 because the THC Seepage Model considered only this geochemical system. Results from the "high" diffusion coefficient Simulation "1" are not shown because validation is based on the parameter values within the range expected. All input and output data files for the REV02 DST THC simulations are given in Attachment X.

7.1.9 Simulation Results: Thermal and Hydrological Evolution

The main driving force for changes in the hydrological and chemical behavior of the system is the strong thermal load applied to the system. The resulting changes in temperature, liquid

saturation, and gas-phase composition lead to changes in the chemistry of water and gas, as well as mineral dissolution and precipitation. A more complete discussion of thermal-hydrological processes is presented in BSC (2003 [161530]). Key aspects of the thermal-hydrological behavior of the DST that drive the chemical evolution of the system are discussed briefly in this section.

The simulation results for the TH evolution of the DST, as well as all other simulation results shown in this section, are based on Simulation "2" above, performed using the EOS4 module in TOUGHREACT V3.0 (LBNL 2002 [161256]). TH (and chemical) results were nearly identical to those not using the vapor-pressure-lowering (EOS3) in Simulation "3," and the latter are therefore not shown. Outputs from all simulations are, however, included in the data submittal to the TDMS. The relatively minor difference in the results is largely related to the implementation of revised capillary pressure curves in the REV02 hydrological parameter set. The REV02 property set has a maximum capillary pressure of 10^8 Pa, which results in a relatively small change in the saturation-temperature history in the rock as it is heated. Low matrix permeabilities in the REV02 parameter set lead to higher matrix pore pressure, thus delaying boiling more substantially than the capillary-pressure-lowering effect. In addition, coupled effects of mineral precipitation/dissolution on flow did not significantly affect the TH evolution of the DST.

The modeled temperatures in the drift reflect the heat input at the drift center (at the approximate location of the electrical canister heater) and subsequent heat transfer to the drift wall (Figure 7.1-3). Differences in temperature between the drift center and the drift wall (Figure 7.1-3) near the top (drift crown) are approximately 20°C, similar to the differences observed between electrical canister temperatures and drift-crown temperature measurements (e.g., DTN: MO0007SEPDSTPC.001 [153707]). Sharp temperature drops are the result of power losses, heater failures, and/or intentional power reductions.

Drift-wall temperatures predicted by the two-dimensional model eventually exceed the maximum measured values by about 20°C. However, predicted temperatures in the rock are typically closer to measured values (Figure 7.1-4). There are several reasons for the elevated temperature in the drift. First, the 2-D cross section can only approximate the exchange of heat through the rock along the axis of the DST. Second, heat lost through the bulkhead by a combination of advection and diffusion is uncertain and can only be approximated using porous flow equations in a basically one-dimensional manner and with a 2-D model. Therefore, this model is most applicable to areas near the center of the test—away from both the bulkhead and the opposite end of the Heated Drift.

Other factors that control the temperature response of the drift wall include thermal properties (conductivity, heat capacity) of the rock and the representation of heat transfer processes in the drift (approximate treatment of thermal radiation and convection). The rate of temperature increase at the drift wall could only be approximated because the model employs a temperature-independent rock heat capacity, does not consider thermal radiation, and does not include a rigorous model for gas convection in the drift. However, the comparison of temperatures measured in the rock, compared to the modeled temperatures, provides the true test of the validity of the model for heat transfer to the rock. Confidence in the approximations employed is gained through the closeness of the modeled temperatures to those measured in the rock (Figure 7.1-4).

The modeled distributions of fracture and matrix liquid saturation (with temperature contours overlain) are shown in Figures 7.1-5a–d. The plots correspond to one and four years from the initiation of the heating phase. The extent of the dryout zone increases over the heating period and is larger in the fractures than the matrix. A wider spatial interval between the 90°C and 100°C isotherms indicates the presence of an isothermal boiling/condensation (heat pipe) zone, which is especially well developed above the wing heaters. An extensive drainage zone extending several tens of meters in the fractures below the heaters contrasts with a very narrow high-saturation zone above the heaters, where water is continuously diverted around the heated zone. The narrow band of increased fracture saturation above the heaters is characterized by temperatures of about 90–95°C. Typically, water was collected from hydrology boreholes when this heat-pipe zone intersected the borehole intervals (BSC 2003 [161530]).

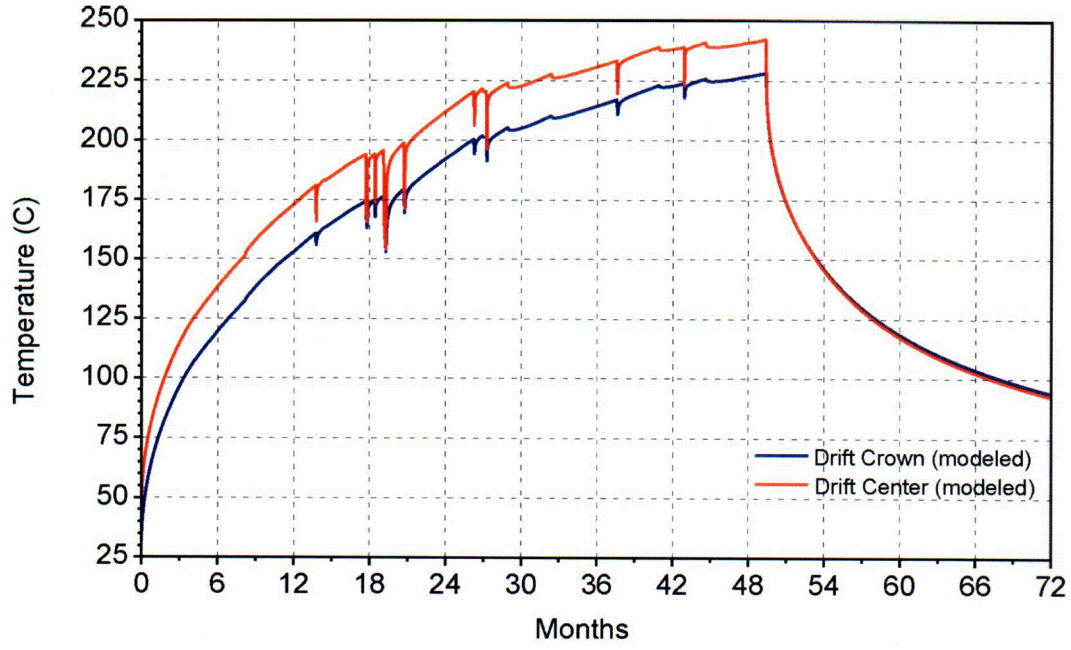

Output-DTN: LB0307DSTTHCR2.001

Figure 7.1-3. Drift Center and Drift Crown Modeled Temperatures over the First Six Years of the DST

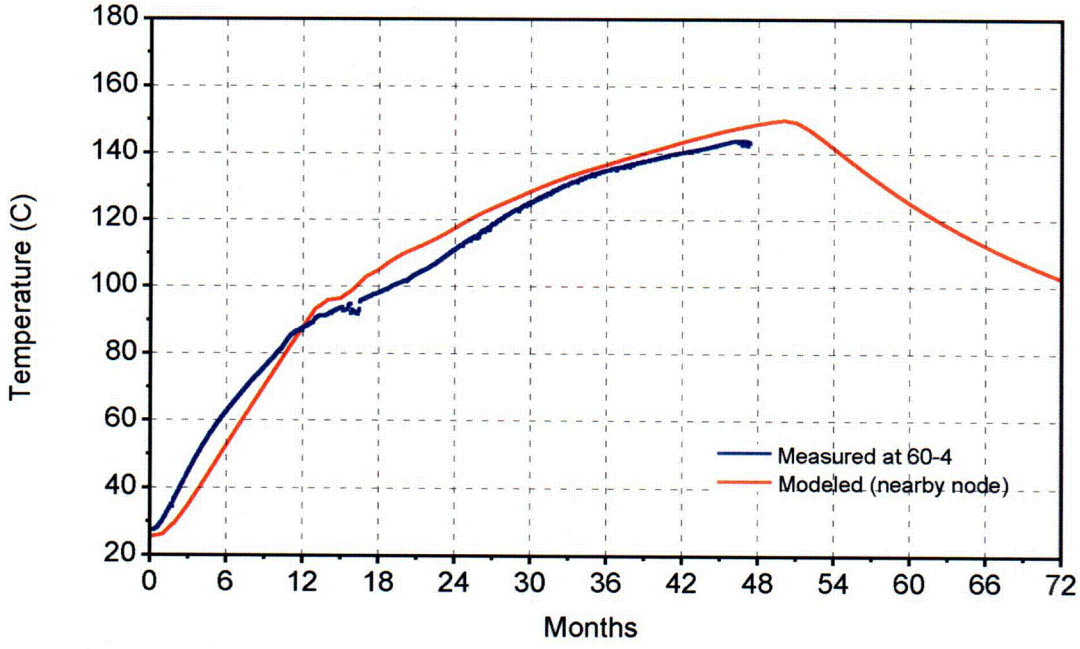

Output-DTN: LB0307DSTTHCR2.001 (modeled)
Table 7.1-1 (DTNs for measured temperatures)

NOTE: Modeled Temperatures are for a Nearby Grid Node. Location of temperature sensor is on Figure 7.1-2.

Figure 7.1-4. Comparison of Modeled and Measured Temperatures over Time for the Sensor Located at Hydrology Borehole Packer 60-4

C103

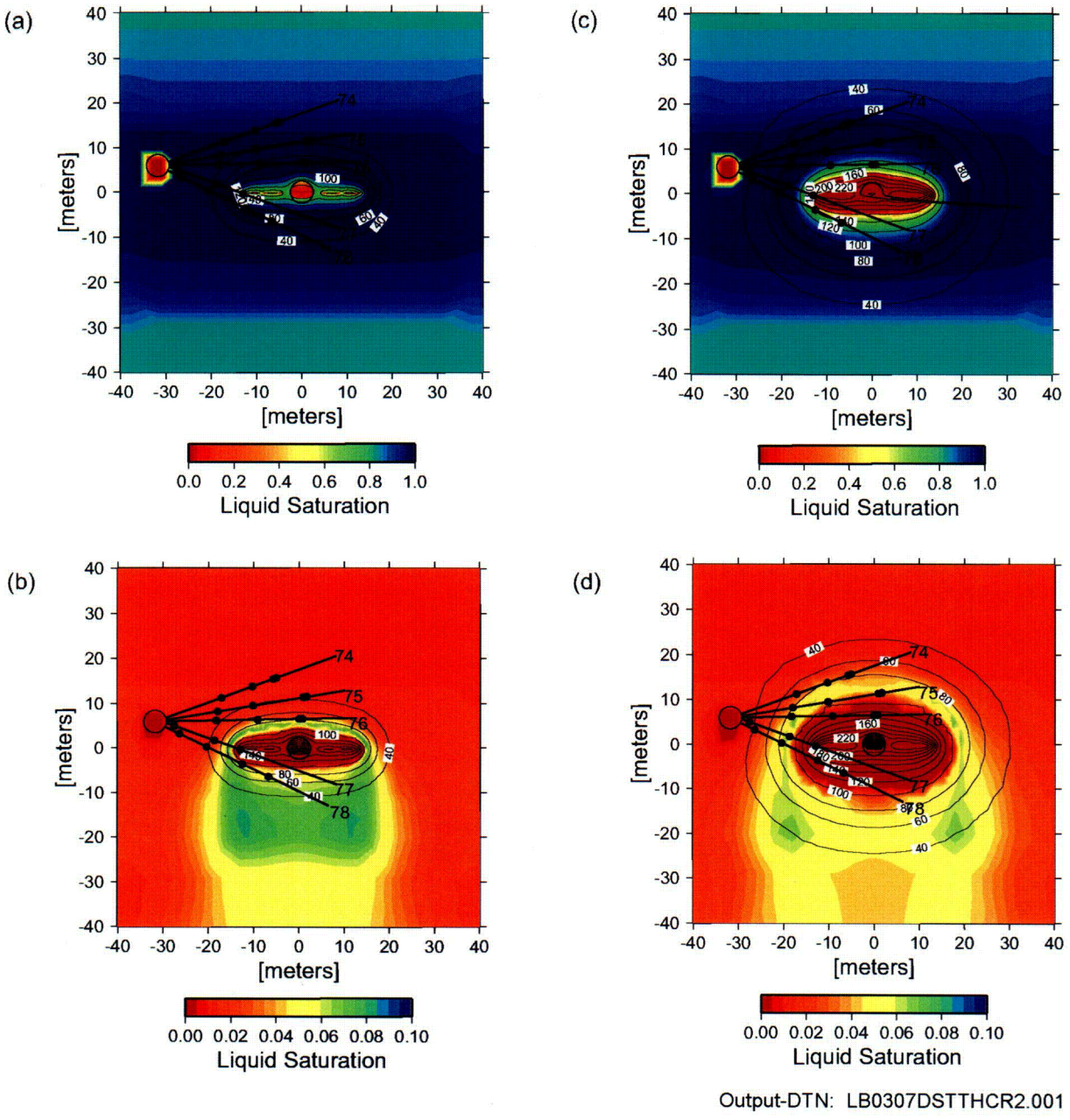

Output-DTN: LB0307DSTTHCR2.001

Figure 7.1-5. Liquid Saturation (Colors) and Temperature (Contour Lines) in the DST (Base Case) at One Year (Matrix – a, Fracture – b) and at Four Years (Matrix – c, Fracture – d)

C104

7.1.10 Gas-Phase CO_2 Evolution: Measured Compositions and Simulation Results

The evolution of CO_2 concentrations in the gas phase is discussed in this section. Simulation results are compared to concentrations measured in gas samples taken from boreholes during the entire heating phase of the DST. The concentration of CO_2 in the gas phase is a function of temperature, pressure, aqueous-phase chemistry, mineral-water reactions, and advective and diffusive transport. From a model validation standpoint, the strong effect of CO_2 partial pressure on water pH and the final brine composition formed upon evaporation make the analysis of CO_2 distributions in the DST important. Numerous measurements of CO_2 concentrations in gas collected from the DST have been made as a function of space and time, and therefore, a more complete comparison of the model results to CO_2 data can be made than to the relatively fewer number of water-chemistry measurements. CO_2 concentrations in gases collected from the DST also provide a qualitative measure of the influence of atmospheric gas on the system, because of the relatively low and constant value in the atmosphere ($\approx$ 400 ppmv). Isotopic compositions of CO_2 (discussed in Section 7.1.14) yield insight into the sources of CO_2.

7.1.10.1 Gas Sampling and CO_2 Measurements

Gas sampling, analytical methods, and compositional data are discussed in Section 6.3.4.2 of BSC (2002 [160771]). Gas samples were taken from several meter-long borehole intervals that spanned a wide range of temperatures as a result of their orientation relative to the heaters. As part of the sampling procedure, the gas samples had much of their water vapor removed before analyses were performed, and therefore measured CO_2 concentrations are for the noncondensible gas fraction. The noncondensible gas fraction is very high (>95%) at the ambient temperature of about 25°C, but may drop to extremely low values (< 1%) under boiling conditions. Hence, reported CO_2 concentrations at temperatures close to boiling are much higher than if the measurements were made on a "complete" gas composition (air + CO_2 + H_2O). This effect must be considered when comparing model results to measured values.

An example of the distributions of measured CO_2 concentrations (DTNs listed in Table 7-1) after one year and after 15 months of heating is shown in Figure 7.1-6. Comparison of the 15-month to the one-year data shows that in nearly all of the boreholes, the CO_2 concentrations are higher at 15 months, owing to heating of pore water and exsolution of CO_2 into the gas phase. Areas that have maintained CO_2 concentrations close to the ambient value in the "rock' of around 1,000 ppmv (log ppmv = -3) can be seen near the observation drift. However, very close to the Observation Drift, some of the values are lower, suggesting that mixing with atmospheric gas may have taken place.

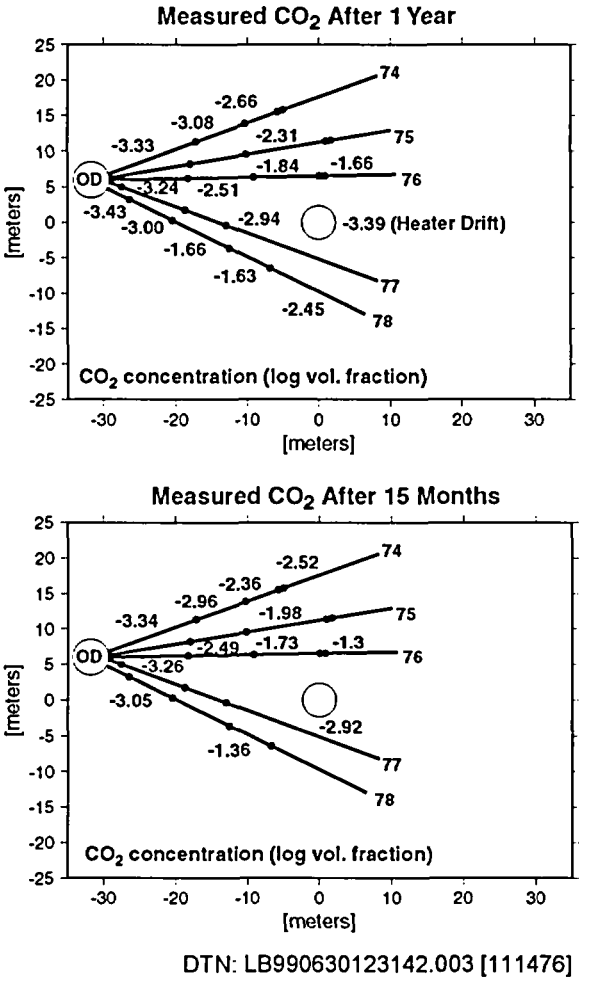

DTN: LB990630123142.003 [111476]

NOTE: Concentrations refer to intervals between pairs of points.

Figure 7.1-6. Measured Concentrations of CO_2 (Log Volume Fraction) in Gas Phase around the DST at 1 Year and at 15 Months

7.1.10.2 Modeled Spatial Distribution of CO_2

Model results are presented for the REV02 extended system (described in Table 6.2-2). Modeled distributions of CO_2 concentrations (log ppmv) in fractures are shown at yearly intervals during the heating phase (Figure 7.1-7) and during the cooling phase (Figure 7.1-8). Over the heating phase of 4 years, a region of highly elevated CO_2 concentrations, centered approximately at the 60°C isotherm, is seen to move gradually outward from the heaters. Outside this region, CO_2 concentrations gradually decrease to the ambient value in equilibrium with pore water (approximately 1,000 ppmv). Maximum CO_2 concentrations of around 50,000 ppmv are located above and below the wing heaters and the Heated Drift. Towards the heaters, CO_2 concentrations drop off more sharply with increasing temperature, decreasing to values below 10 ppmv. This sharp decline takes place as a result of the CO_2 degassed during heating of the pore water, its transport outward, and the displacement of air and CO_2 by steam generated during boiling.

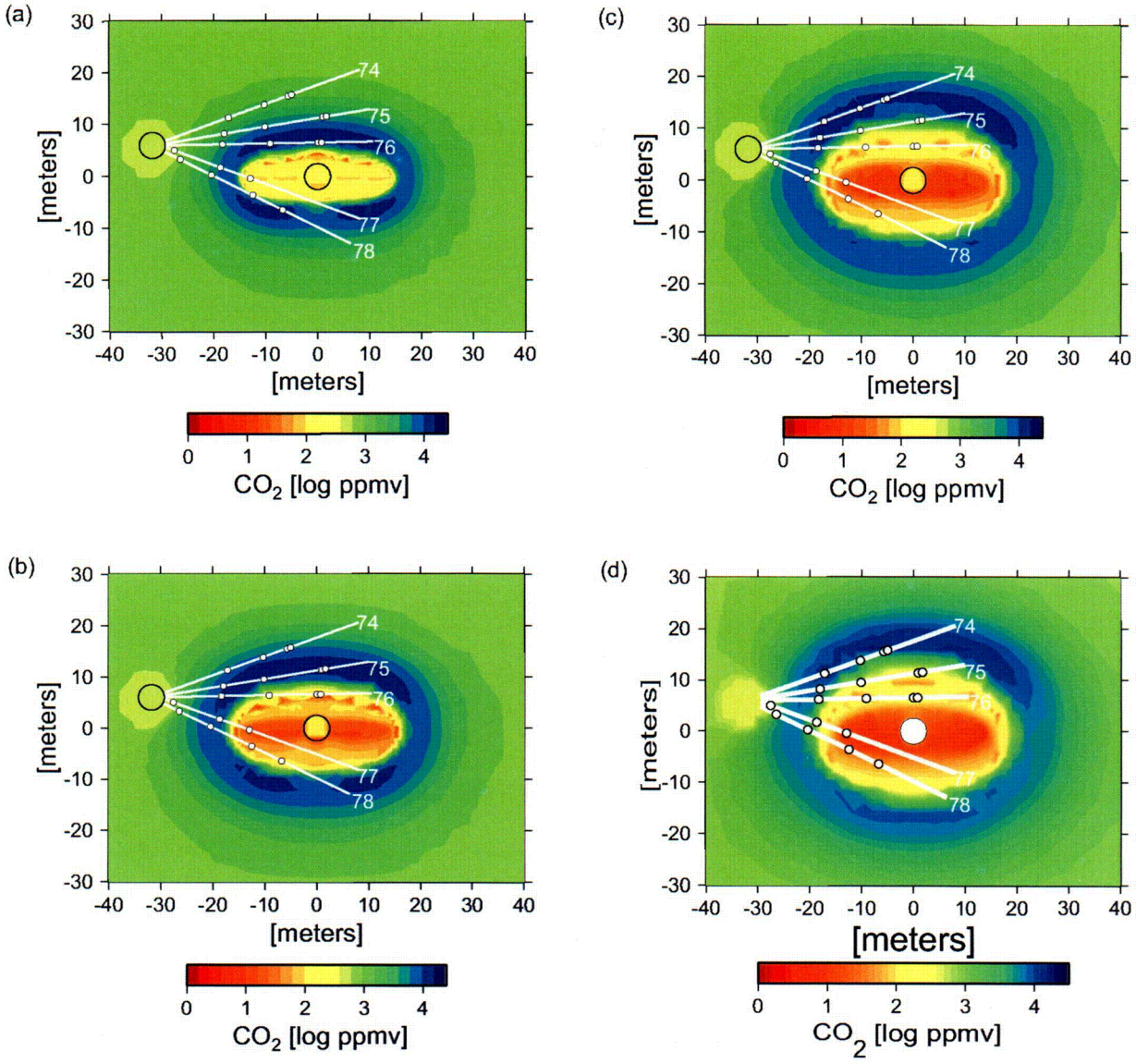

Output-DTN: LB0307DSTTHCR2.001

Figure 7.1-7. Modeled Gas Phase CO_2 Concentrations (Log ppmv) in Fractures during the Heating Phase of the DST at 1, 2, 3, and 4 years

The zone of maximum CO_2 concentrations also transects the hydrology borehole intervals as it migrates outwards, with some intervals registering a two order-of-magnitude variation between them.

The effect of the atmospheric CO_2 concentration of the gas in the Observation Drift on its surroundings is evident up to about 10 m from the drift wall. However, effects on the fracture gas composition are relatively minor beyond about 5 m from the drift wall. Carbon dioxide concentrations in the Heated Drift stay close to the atmospheric value, owing to transport (advection and diffusion) between the Heater Test Alcove (set to atmospheric CO_2) and the Heated Drift.

The modeled cooling phase of the DST (Figure 7.1-8) is characterized by a gradual re-equilibration of CO_2 concentrations throughout the DST area, via cooling, gas-phase diffusion, and flow of gas and water. Exchange of atmospheric gas among the Heated Drift, the Heater Test Alcove, and the rock around the Heated Drift is clearly evident.

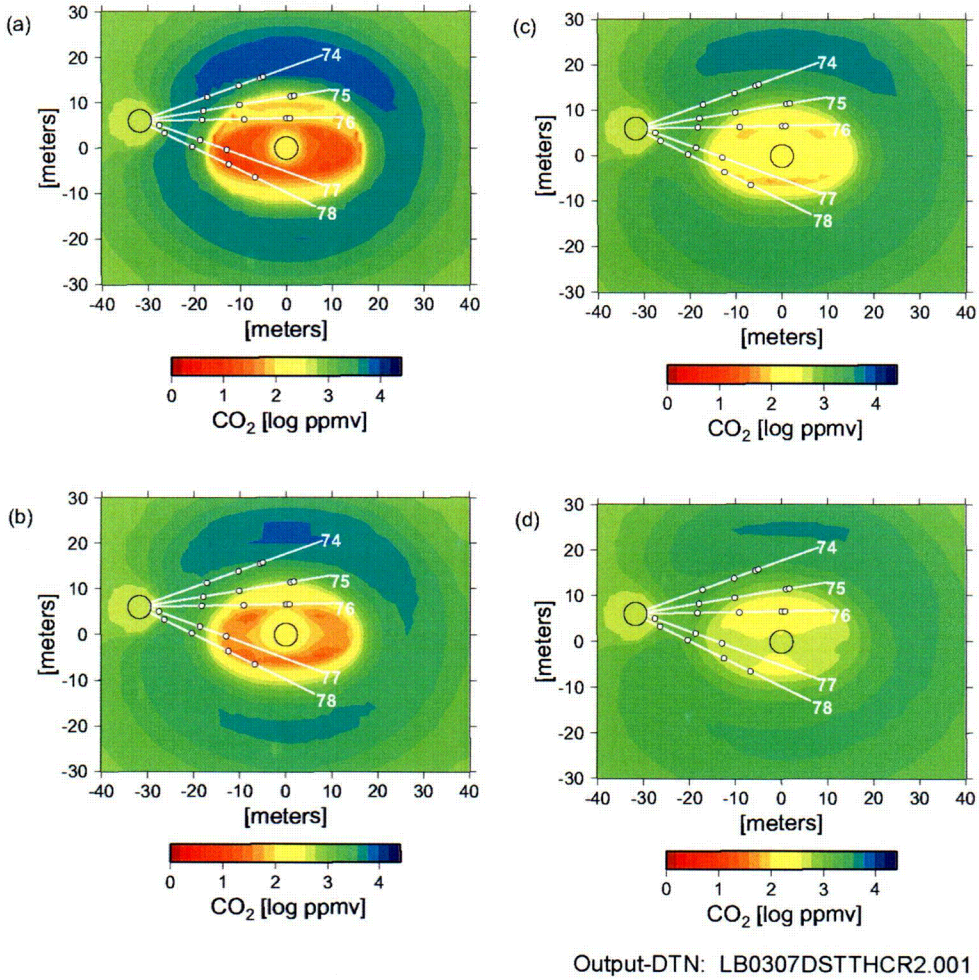

Output-DTN: LB0307DSTTHCR2.001

Figure 7.1-8. Modeled Gas Phase CO_2 Concentrations (Log ppmv) in Fractures during the Cooling Phase of the DST at 5, 6, 7, and 8 years

7.1.10.3 Modeled and Measured CO_2 Concentrations Over Time

Validation of the DST THC Model for the prediction of the temporal evolution of CO_2 concentrations was performed by comparison of measured values from intervals repeatedly sampled from February 1998 through January 2002 (DTNs listed in Table 7-1) to model results. The locations of the gridblock central coordinates relative to the gas collected in borehole intervals from which the gas samples were taken are illustrated in Figure 7.1-9. Because the measured concentrations come from borehole intervals that are several meters long, and not from a specific location, model data are chosen from the gridblock closest to the center of the interval. If a gridblock is not centered on the borehole, a gridblock closest to the center is chosen on the outer (cooler) side of the borehole. Gridblocks on the cooler side should compare more closely to the measured data because the 2-D model, having no heat loss in the rock perpendicular to the drift, produces temperatures that are somewhat higher than the measured temperatures after approximately the first year of heating. However, measured temperatures may be higher prior to that time (refer back to the temperature comparison in Figure 7.1-4).

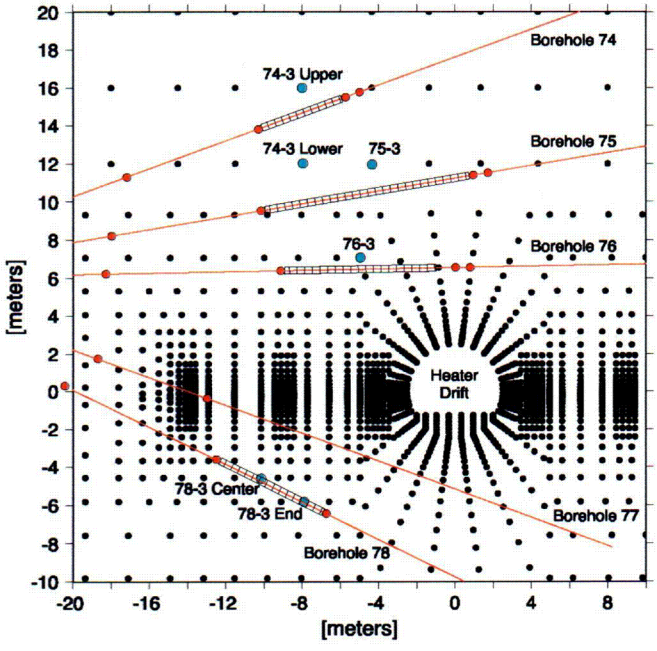

DTN: LB991200DSTTHC.002 [142162]

NOTE: Borehole intervals from which gas samples were taken are shown in the hachured regions.

Figure 7.1-9. Close-Up of DST Grid, Showing Nodes Used to Extract Model Data for Comparison to Concentrations Measured in Gas Samples

The results obtained using the REV01 parameters for the base-case and extended-case systems are shown in Figure 7.1-10. The measured concentrations have not been corrected for the loss of water owing to condensation of steam in these plots. These corrections were applied to the more complete data set shown later in this section and compared to REV02 model results. Measured CO_2 concentrations in borehole 74 interval 3 (hereafter, referred to as "borehole-interval 74-3" or just 74-3) shown in Figure 7.1-10a (the uppermost, lowest-temperature interval) are well-

C107

bracketed by the two geochemical systems. The base-case simulations yield the highest concentrations of CO_2, owing to differences in water chemistry (e.g., generally lower pH) and their effect on the equilibrium partial pressure of CO_2. The measured concentrations show a sharp increase at 24 months. This is partly a result of the relatively low value around 21 months, which apparently was affected by an earlier temporary power loss (see Table 7.1-2 for dates of power losses). After 24 months, the measured concentrations declined moderately, whereas the modeled concentrations continued to rise, albeit more slowly. This decrease in measured CO_2 concentrations may reflect the power reductions that were implemented during 2000. The trend in modeled CO_2 concentrations for 75-3 is similar to the measured trend, with a sharp reduction in concentration after 24 months (Figure 7.1-10b). The upper interval closest to the heaters is 76-3, in which the measured data (Figure 7.1-10c) shows a large decline after 21 months, which has predicted to occur earlier than actually observed. This difference may between prediction and observation result from the gridblock being closer to the interval in 76-3 than in 74-3 and 75-3, and therefore slightly hotter at a given time. In borehole interval 78-3 (Figure 7.1-10d), the simulated trends in CO_2 concentrations in the early and late time periods are similar to the measured values, but the maximum measured values are higher. Because of the steep angle of the borehole relative to the temperature isotherms, mixing of higher and lower concentrations likely took place in this interval.

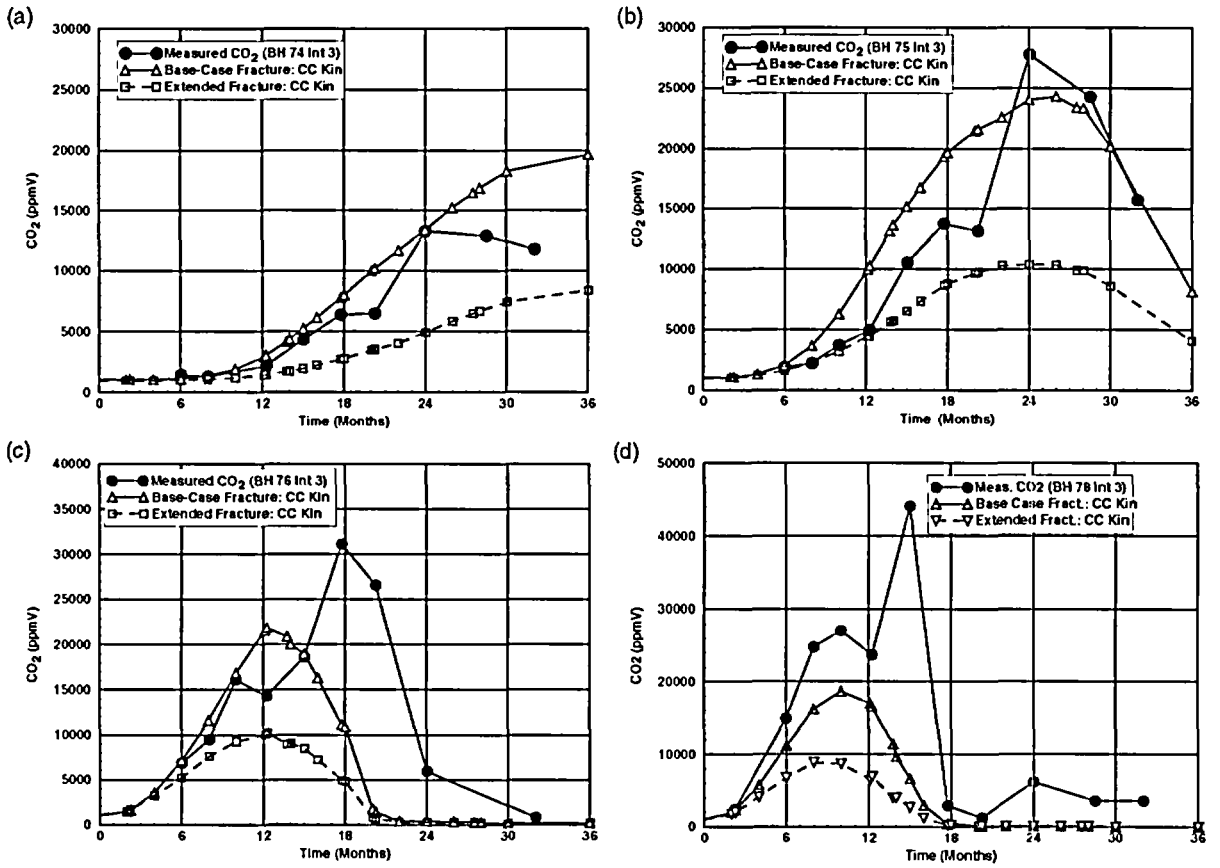

DTNs: LB0011DSTTHCR1.002 [161282] (simulated), LB0102CO2DST98.001 [159306] (measured), LB990630123142.003 [111476] (measured), LB000121123142.003 [146451] (measured), LB0011CO2DST08.001 [153460] (measured), CRWMS M&O 2001 [153814] (measured)

Figure 7.1-10. Comparison of Modeled CO_2 Concentrations (Base Case CC Kin and Extended Case CC Kin) in Fractures to Measured Concentrations in Boreholes: (a) Borehole Interval 74-3 at Node Above Interval; (b) Borehole Interval 75-3; (c) Borehole Interval 76-3; (d) Borehole Interval 78-3 at Node Near End of Interval

The strong increase in measured CO_2 concentrations in 76-3 and 78-3 to values significantly higher than the predicted concentrations, after an apparent earlier maximum, occurs at different times in the two intervals. This difference cannot be explained simply by a change in the heater power output. The measured CO_2 concentrations in gas samples collected at close to boiling temperatures are significantly affected by the amount of water vapor in the gas phase. The samples are "dried" by condensing much of the water out at a low temperature (~ 4°C), and therefore, the measured concentrations reflect the CO_2 in the air after water has been condensed out. The model results include the water-vapor component and which may be very different from the measured value, once the air-mass fraction drops to a low value and the CO_2/air ratio increases through the condensation of the water vapor. Therefore, modeled and measured compositions become less directly comparable at higher temperatures. The second peak in the measured concentrations in 76-3 and 78-3 may therefore be explained by the rapid decline in the air mass fraction during boiling.

Differences in the calculated CO_2 concentrations in the extended geochemical system (compared to the base case) are a result of dissolution and precipitation of various aluminosilicate minerals, such as stellerite, heulandite, anorthite, and smectite. Feldspar dissolves to form zeolites, thus increasing the pH through hydrolysis reactions. This, in turn, decreases the CO_2 partial pressures through aqueous species reactions involving carbonate species (CO_2 is more soluble at elevated pH). Another controlling factor is the flux of aqueous species through percolation and of CO_2 through gas-phase diffusion, relative to the rates of mineral reactions. The percolation flux has little effect over a few years, so that for comparison of the model results, the relative rates of reaction remain as the main reason for the difference between base-case and extended-case CO_2 concentrations.

Some shifts in the ambient system CO_2 concentrations over a relatively short time (away from the areas of thermal effects) indicate that either the relative mineral-water reaction rates are somehow dissimilar to the real system, or that calculated starting water bicarbonate concentration (via charge balance) was off, or the measured pH was altered through the sample collection procedure. Because the starting water was supersaturated in calcite, the latter scenario is a distinct possibility. In addition, the uncertainties in thermodynamic data for the aluminosilicates (e.g., zeolites and clays), the unknown reaction rates for many of the minerals, and the use of endmember minerals rather than solid solutions must play a role in the evaluation of the results. However, increases in CO_2 concentrations as a result of pore water degassing far exceed the changes due to ambient system disequilibrium.

The base-case geochemical system appears to compare more closely than the extended system for CO_2 concentrations. However, the increasing water-vapor fraction in the gas phase over time means that actual CO_2 concentrations in the vapor phase are increasingly depressed in comparison with measured values. This fact may be used to infer that the extended system CO_2 values could be closer to the actual values, if the measured concentrations were corrected for the vapor that was removed during sample collection. Yet, evidence that the base-case geochemical system may actually yield CO_2 concentrations closer to the measured values comes from the better match to pH values measured in waters collected from boreholes.

Figure 7.1-11 shows measured CO_2 concentrations that have been corrected for the effect of water-vapor condensation during sample collection. More details regarding the effect and the process involved in the correction procedure are given following the discussion of REV02 results in this section. Additional measured and modeled data are presented up to the end of the heating phase of the DST (including a few measurements performed about 1 month into the cooling phase). Simulated CO_2 concentrations obtained for the REV02 extended case are similar to those for REV01 (Figure 7.1-11). In the hottest interval (76-3) the concentrations remained low from 2 years after heating was initiated until after the cooling phase had begun. Except for one sample that may have been predominantly water vapor, similar but delayed behavior took place in 75-3. Modeled compositions shown for 74-3 are given as an average of the values from the "upper" and "lower" gridblocks shown in Figure 7.1-9. Maximum CO_2 concentrations in the model simulations are closer to the REV01 base-case concentrations and the measured concentrations, even though the REV02 model input also included aluminosilicates. This result suggests that the REV02 geochemical input data (thermodynamic and kinetic data) are improved overall. Also, because the thermal and hydrological properties have changed, as well as the heat input function, factors leading to the improved result cannot be directly pinpointed.

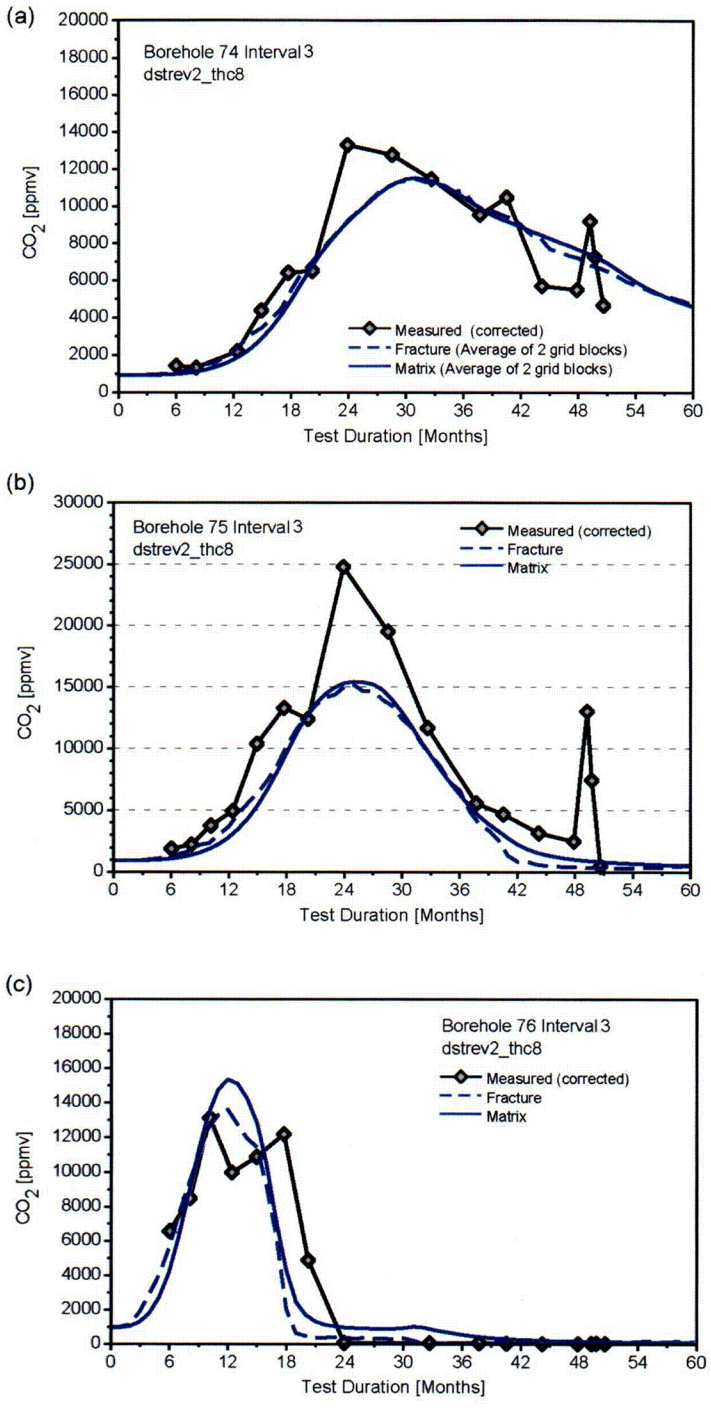

DTNs: LB0208ISODSTHP.001 [161638] (measured CO_2 uncorrected), LB0307DSTTHCR2.001 (modeled)

Figure 7.1-11. Comparison of REV02 Modeled CO_2 Concentrations (extended case) in Fractures to Measured (Corrected) Concentrations in Boreholes: (a) Borehole Interval 74-3 (Average of Bounding Gridblocks); (b) Borehole Interval 75-3; (c) Borehole Interval 76-3

C108

To assess the effect of water extraction from the gas during collection, CO_2 concentrations were corrected for the approximate amount of water removed during chilling of the gas sample from the temperature of the sampling interval to 25°C. The method assumes that the gas is vapor-saturated, removes the appropriate amount of water vapor to the amount at saturation at 25°C, and adds some of the CO_2 into solution (the condensate) as HCO_3^-, based on the equilibrium partitioning of CO_2 into H_2O. The actual temperature of the chiller was 4°C; however, the efficiency of the unit was such that not all water was taken out when the gas was at boiling temperatures (BSC 2003 [161530]). Therefore, for consistency, the chill temperature was set to 25°C for all samples. Because the difference in water-vapor content between 25°C and 4°C is small, this approximation is valid. For samples with temperatures below approximately 60°C, the correction is very small; however, at temperatures near boiling, the correction may be close to an order of magnitude. The corrections are documented in Wang (2003 [161665], SN-LBNL-SCI-112-V2, pp. 60–63).

The effect of the correction on the measured CO_2 concentrations is a gradual (but increasing) reduction up to the boiling temperature, where the sharp "second" spike in the uncorrected data largely disappears. It is clear that the correction to the measured concentrations substantially improves the comparison to the modeled data at higher temperatures. Figure 7.1-12 shows an example of the effect of the correction on the CO_2 concentrations for borehole interval 75-3.

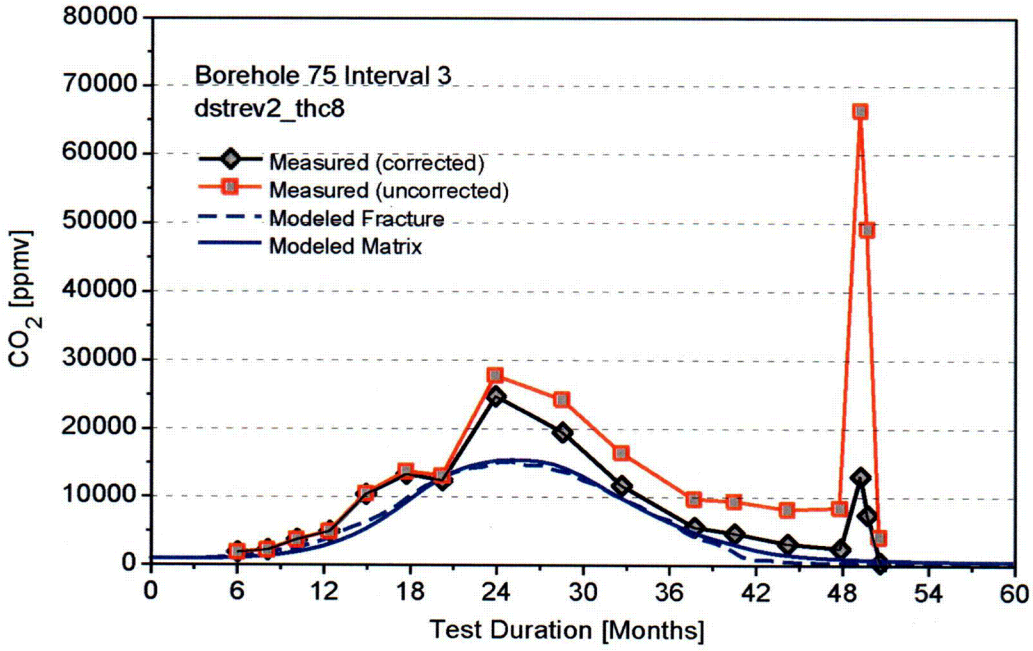

DTNs: LB0208ISODSTHP.001 [161638] (measured CO_2 uncorrected), LB0307DSTTHCR2.001 (modeled)

Figure 7.1-12. Comparison of Measured and Corrected Concentrations for Borehole Interval 75-3 and the REV02 Model Simulation Results

Trends in modeled CO_2 concentrations are clearly followed for all borehole intervals evaluated. Deviations in concentrations for certain samples can be attributed to the factors discussed in Section 7.1.7. The comparison of simulated and measured (corrected) CO_2 concentrations are

C109

generally within a factor of 2, and in most cases within an order of magnitude, except for very low concentration samples where the values are strongly affected by condensation of water vapor and for the various reasons discussed in Section 7.1.7. Therefore, the validation criteria (1 and 2) discussed in Section 7.1.7 have been met.

7.1.11 Aqueous Species Evolution

7.1.11.1 Chemistry of Waters Sampled during the Drift Scale Test

Water samples were collected from several hydrology boreholes during the heating phase of the DST. Collection dates, volumes, and field measurements (e.g., pH) for all water samples are presented in Table 6.3.4.1-1 of BSC (2002 [160771]). Cation and anion analyses of the water samples are given in Table 6.3.4.1-2 (DTN: LL020709923142.023 [161677]) of the same report. The latter table lists all samples that were analyzed, regardless of their origin. In particular, many samples were collected from borehole intervals above boiling temperatures and were clearly derived from water vapor that condensed in the tubing leading out of the interval. In most cases such samples are clearly recognizable from the water samples pumped directly out of boreholes (and in contact with rock), based on (1) their significantly lower pH (most below pH 5) relative to "true" water samples (nearly all above pH 6), (2) their extremely low anion and cation content (total dissolved solids around 10 ppm or less), and (3) very low total Si concentrations (most much less than 10 mg/L) compared to water samples having total Si concentrations mostly greater than 40 mg/L.

Specific exceptions to these criteria are those samples collected from intervals at high temperatures (> 140°C) that have relatively low pH values (< pH 4), elevated F^- concentrations (> 10 mg/L) and relatively high total Si values, but contain few other measurable constituents. Experimental studies confirmed the hypothesis that the breakdown of fluoroelastomer packer materials at elevated temperatures was responsible for the unusual water compositions that formed as high-temperature vapor condensed in tubing and was collected as water (BSC 2002 [160771]). In addition, some waters may have been affected by the degradation of neoprene packers in sub-boiling zones, such as the high Cl water collected from Borehole 59, interval 4 (Williams 2003 [163765]). Also note that samples of water from boreholes may be affected in subtle ways by the above processes.

In this report, chemical analyses of water samples that have compositions indicating that they were wholly or mostly derived from water that had resided in a borehole (rather than formed during condensation of water vapor in the collection tube) are given in Table 7.1-3. The intervals where these waters were collected are shown as the blue shaded zones in Figure 7.1-13. The water samples collected during the test were obtained from zones that were hotter than the temperatures given for the samples, because the samples cooled substantially as they were pumped out of the rock through the sample collection tubing, and into the sample containers. Also listed in Table 7.1-3 are the compositions of pore waters that had been ultracentrifuged out of the rock matrix from a dry-drilled borehole near the DST ("HD-PERM" designations).

Table 7.1-3. Measured Concentrations in Tptpmn Pore Water from Alcove 5 and Chemistry of Water Samples from Hydrology Boreholes

SMF No. (SPC0...)	1002488	1002586	1002525	05279699	05279689	0527915[6]	0527977[6]	0527916[6]	0541804[6]	0541804[6,6]	05043968	0529637-#1[6]	0529637-#2[6]
Collection Date	Pre-Htng.	Pre-Htng.	Pre-Htng.	06/04/98	06/04/98	08/12/98	06/04/98	8/12/98	11/12/98	11/12/98	01/26/99	03/30/99	03/30/99
Collection Time												9:50 AM	9:55 AM
Sample ID	PERM-1[4]	PERM-2[4]	PERM-3[4]	BH 60-2	BH 60-2	BH 60-2	BH 60-3	BH 60-3	BH 60-3	BH 60-3	BH 60-3	BH 60-3	BH 60-3
Field pH[2]	7.79	8.32	8.31	7.5	na	6.9	7.7	6 8	6.92	6.92	7.4	8 0	na
Metals / Cations													
Na (mg/L)	60.5	61.0	61 5	20 0	na	20.4	24 0	17.2	10.1	20 3	19.1	11 2	11 0
Si (mg/L)	37	31	35	56	na	51.8	41	43 5	60 0	53 8	65 0	62.8	59 8
Ca (mg/L)	98 17	106.17	96 67	20	na	19.9	25	18.7	15.3	13.9	5.93	2.06	2.27
K (mg/L)	6.0	7.0	9 0	6 0	na	5 4	4 5	4 5	8.7	7.8	4 1	2 4	2 4
Mg (mg/L)	25.65	16.55	17.35	2 9	na	1.21	5.7	4 0	3 35	3 00	1.17	0.27	0 26
Al (mg/L)	< 0.06	< 0.06	< 0 06	0.12	na	< 0 06	0.017[5]	0.003[5]	0 033[5]	0 033[5]	< 0 06	0.36, 0.27[5]	0.36, 0.27[5]
B (mg/L)	3 05	2.75	2.75	1.2	na	1.84	0.92	1.14	1.58	1.41	1.75	2.10	2.11
S (mg/L)	42.25	38 6	38 65	5 5	na	4.5	9.2	5.2	11.6	10.5	6 4	1.83	1 82
Fe (mg/L)	< 0.02	< 0.02	< 0.02	0 04	na	0 02	< 0 02	0.12	0 02	< 0 02	< 0 02	< 0 02	< 0.02
Li (mg/L)	0.1	0 45	0.05	0.07	na	0.03	0.07	0.040	0.040	0.040	0.02	0.02	< 0.01
Sr (mg/L)	1.4	1	1 05	0.18	na	0.11	0.34	2.21	0 22	0 20	0 09	0 02	0 02
Anions													
HCO_3 (mg/L)[3]				na	na	na	na	na	na	na	41	25 0	na
F (mg/L)	0.36	0 96	0.76	na	1.00	0.71	0.82	0.43	0.49	0.50	1.27	1.02	0 97
Cl (mg/L)	122.73	109 93	123 13	na	10	6.14	16	5 52	19 5	19 6	10 3	4 15	3 92
Br (mg/L)	0.6	0.76	1.2	na	0 84	0 05	0.73	0 21	0 6	0 51	0 15	< 0 04	< 0 04
SO_4 (mg/L)	124.18	111.38	119.78	na	17	4 88	30	8.81	30 6	30.8	13.5	3.83	3.75
PO_4 (mg/L)	< 0 07	< 0 07	< 0 07	na	< 0 07	0 25	< 0 07	0 16	< 0 2	< 0 2	< 0 05	< 0 05	< 0 05
NO_2 (mg/L)	< 0 04	< 0 04	< 0.04	na	< 0.01	< 0.04	< 0.01	< 0.04	< .10	< .10	< .03	< 0 03	< 0 03
NO_3 (mg/L)	21.72	2.52	10.40	na	3.00	0.46	3.6	0.60	3.38	3.17	2.56	0 92	0 84

Table 7.1-3. Measured Concentrations in Tptpmn Pore Water from Alcove 5 and Chemistry of Water Samples from Hydrology Boreholes (continued)

SMF No. (SPC0...)	0551159[6]	0551160[6]	0557029[6]	0557032	0557033[6]	0557080	0557081	0557083	0557022	0550671	0550673	0550681	0550682
Collection Date	08/09/99	08/09/99	10/27/99	10/27/99	10/27/99	11/30/99	11/30/99	11/30/99	01/25/00	01/25/00	01/25/00	05/23/00	05/23/00
Collection Time													
Sample ID	BH 59-2(AC)	BH 59-2(BC)	BH 59-2	BH 59-2	BH 59-2	BH 59-2	BH 59-2	BH 59-2	BH 59-2	BH 59-2	BH 59-2	BH 59-2	BH 59-2
Field pH[2]	na	na	na	5 93	6 08	6.86	7.24	na	7 07	6 68	na	6 96	6.96
Metals / Cations													
Na (mg/L)	30	24	na	9.2	9.2	6.6	7.7	na	8 1	6 6	na	17	18
Si (mg/L)	78	81	na	44.5	44 9	38 0	39.9	na	42.8	41.7	na	59 4	59 2
Ca (mg/L)	47	39	na	7.53	7.47	4 33	5 63	na	7.54	2.89	na	4.7	4.4
K (mg/L)	8	6	na	3 4	3 6	2.6	3.0	na	3.6	2 8	na	4 3	4 4
Mg (mg/L)	13	11	na	1.81	1.72	1 02	1 38	na	1.78	0.72	na	1.1	1.1
Al (mg/L)	< 0 2	< 0.2	na	0.033[7]	0 033[7]	0 030	0.030	na	< 0.05	0 043	na	< 0 053	< 0 053
B (mg/L)	0.8	0.6	na	0 27	0.21	0.14	0 17	na	0 29	0 21	na	na	na
S (mg/L)	22	17	na	2 52	2 50	0.76	1.33	na	6 44	0 65	na	na	na
Fe (mg/L)	0 41	0 32	na	0.20	0.19	0 09	0 14	na	0.07	< 0.02	na	< 0 038	< 0 038
Li (mg/L)	< 4	< 4	na	0.16	0 01	0.01	0.01	na	< 0 01	< 0 01	na	0 021	0.022
Sr (mg/L)	0 54	0 45	na	0.11	0 08	0 06	0.08	na	0.091	0.036	na	< 0 013	< 0 013
Anions													
HCO_3 (mg/L)[3]	na	na	23 5	na	23.5	na	na	22 3	na	na	22.8	31.4	31.4
F (mg/L)	0 725	0.575	0.27	na	0 27	na	na	0 35	na	na	0 73	0 58	0 55
Cl (mg/L)	88.3	71 0	9 5	na	9.1	na	na	5 0	na	na	3.8	10.15	10 6
Br (mg/L)	0.515	0.46	0 61	na	0 58	na	na	< 0 03	na	na	< 0.1	< 0.1	0.38
SO_4 (mg/L)	64 2	53 5	6 2	na	6.3	na	na	2 8	na	na	1.8	2.9	3.18
PO_4 (mg/L)	< 0 02	< 0.02	< 0.02	na	< 0 02	na	na	< 0.02	na	na	0 62	< 0 2	< 0.2
NO_2 (mg/L)	< 0.007	< 0 007	< 0 007	na	< 0.007	na	na	< 0 007	na	na	< 0.05	< 0.06	< 0.06
NO_3 (mg/L)	3.79	2 83	1 32	na	1.40	na	na	< 0 02	na	na	0.77	0.56	0.54

Table 7.1-3. Measured Concentrations in Tptpmn Pore Water from Alcove 5 and Chemistry of Water Samples from Hydrology Boreholes (continued)

SMF No. (SPC0...)	0550684	0550693	0550694	0550691	0550689	0550690	0530398	0557036[a]	0557038[a]	0552575	0557043	0541803[a]	0541803[a,4]
Collection Date	05/23/00	06/29/00	06/29/00	06/29/00	06/29/00	06/29/00	01/23/01	10/27/99	10/27/99	11/30/99	11/30/99	11/12/98	11/12/98
Collection Time													
Sample ID	BH 59-2	BH 59-2	BH 59-2	BH 59-2	BH 59-2	BH 59-2	BH 59-2	BH 59-3	BH 59-3	BH 59-3	BH 59-3	BH 59-4	BH 59-4
Field pH[2]	6 95	6 99-7.08	6.99-7.08	7.00	na	na	na	na	6.64	7.47	na	6 63	6 63
Metals / Cations													
Na (mg/L)	17	16	15	< 4 8	na	na	29	na	19.3	15 6	na	22 6	135
Si (mg/L)	59 3	62.7	57.5	36.3	na	na	84 5	na	84.2	92.5	na	33 5	44 2
Ca (mg/L)	4.5	4 3	3 8	2.0	na	na	7 8	na	13 2	2 86	na	476	450
K (mg/L)	4 4	4.7	4.2	2.5	na	na	5 8	na	5.6	3.9	na	29 5	37 8
Mg (mg/L)	1.1	1.1	1.0	0.54	na	na	1 8	na	1.49	0.29	na	64.1	83.9
Al (mg/L)	< 0 053	< 0.053	< 0 053	< 0 11	na	na	< 0 053	na	0.040	0 071	na	0 01[5]	< 0 06
B (mg/L)	na	na	na	na	na	na	na	na	0 86	1 06	na	4.47	4.13
S (mg/L)	na	na	na	na	na	na	na	na	14 48	3 25	na	50.7	64.8
Fe (mg/L)	< 0 038	< 0.038	< 0.038	< 0 076	na	na	< 0 038	na	< 0.02	< 0 02	na	< 0 02	< 0 02
Li (mg/L)	0.021	0 019	0 018	0.010	na	na	0 033	na	0 02	0 02	na	0.21	0.20
Sr (mg/L)	< 0.013	< 0 013	< 0 013	< 0 026	na	na	< 0.013	na	0.13	0 03	na	4.02	3.71
Anions													
HCO_3 (mg/L)[3]	31.4	na	na	na	29 4	29 4	na	12.4	12.4	na	20 7	na	na
F (mg/L)	0 49	na	na	na	0.18	0.15	0.78	0 64	0 73	na	1.3	0.8	4.3
Cl (mg/L)	10.15	na	na	na	0.90	0.32	25.20	12.9	12 9	na	8 8	1,130	1,250
Br (mg/L)	< 0.1	na	na	na	0 62	0.48	< 0.1	0.89	0.51	na	< 0 03	1.13	< 0.07
SO_4 (mg/L)	3.1	na	na	na	0.5	0.42	9.5	40 7	40.3	na	8.2	226	213
PO_4 (mg/L)	< 0.2	na	na	na	< 0 2	< 0 2	< 0.2	< 0.04	< 0 04	na	< 0 02	< 5	< 0 2
NO_2 (mg/L)	< 0.06	na	na	na	< 0.06	< 0 06	< 0 06	< 0 01	< 0 01	na	< 0 007	< 3	< 10
NO_3 (mg/L)	0.71	na	na	na	0.65	0 48	0 99	3 06	3 05	na	2.4	3.12	7.81

Table 7.1-3. Measured Concentrations in Tptpmn Pore Water from Alcove 5 and Chemistry of Water Samples from Hydrology Boreholes (continued)

SMF No. (SPC0...)	0504397[4]	0551169[4]	0559464	0559458	0559456	1016082	0557040[6]	0552578	0552579	0550697	0541805[6]	0541805[6,8]	0527961[6]
Collection Date	01/26/99	08/10/99	04/17/01	04/17/01	04/17/01	01/07/02	10/27/99	11/30/99	11/30/99	05/23/00	11/12/98	11/12/98	01/26/99
Collection Time													
Sample ID	BH 59-4	BH 61-3	BH 76-2	BH 76-2	BH 76-2	BH 76-2	BH 76-3	BH 76-3	BH 76-3	BH 76-3	BH 186-3	BH 186-3	BH 186-3
Field pH[2]	na	na	7 68	8 22	8.29	7.8	6.14-6.46	6 94	na	6 92-6 96	6 83	6 83	7 2
Metals / Cations													
Na (mg/L)	219	19	9	9	9	na	64 5	28 2	na	29	105	17.0	25 9
Si (mg/L)	12.0	67	42 6	44.1	45.6	na	133.4	92.8	na	96 0	16 0	27.2	49 3
Ca (mg/L)	429	14	1.3	1.1	1.3	na	59.5	22 3	na	7.1	11.5	20.2	2.92
K (mg/L)	29.7	5	1 6	1.6	1.9	na	13.4	7.4	na	6 5	3 5	3.9	5 9
Mg (mg/L)	164	3.2	0.27	0 22	0 23	na	13 8	4.71	na	1.4	5.1	5.68	6.32
Al (mg/L)	0 086[5]	< 0 2	0 42	0 43	0 45	na	0.010	0 031	na	< 0 053	< 0.003[5]	< 0.003[5]	< 0 06
B (mg/L)	6 68	1.5	na	na	na	na	2.38	0 81	na	na	0.51	0.58	0.84
S (mg/L)	109	3.1	na	na	na	na	34.55	9.46	na	na	8 47	9 42	7 9
Fe (mg/L)	< 0 02	1.2	0.40	0 40	0 39	na	< 0 02	0.10	na	< 0.038	0.02	< 0.02	0.09
Li (mg/L)	0.33	< 4	0 0098	0 010	0.0076	na	0.13	0 04	na	0 045	0 05	0 05	0 05
Sr (mg/L)	5.84	0.14	< 0 013	< 0 013	< 0 013	na	0.78	0.26	na	< 0.013	0.30	0.34	0.37
Anions													
HCO_3 (mg/L)[3]	na	na	na	na	na	< 5	na	na	82 3	na	na	na	116
F (mg/L)	0.51	0.835	na	0 38	0 47	0 4	1.11	na	1.3	0.76	0.56	0.62	1 20
Cl (mg/L)	1,160	24.1	na	1.9	1.71	2.75	81 9	na	19	14.5	18.7	18.6	23.3
Br (mg/L)	1.51	0 35	na	< 0.1	< 0.1	< 0.2	0 97	na	< 0 03	< 0 1	0 67	0 60	0.32
SO_4 (mg/L)	240	9.13	na	0 89	0 85	1 02	94 6	na	26.0	4.98	26.3	26.2	21
PO_4 (mg/L)	< 0 5	< 0 02	na	< 0 2	< 0.2	< 0.3	< 0.02	na	< 0.02	< 0 2	< 0 2	< 0 2	< 0.1
NO_2 (mg/L)	< 3	< 0 007	na	< 0.06	< 0.06	< 0 2	< 0 007	na	< 0 007	< 0 06	< .1	< .1	< 0.05
NO_3 (mg/L)	11 6	0 825	na	< 0.09	< 0.09	< 0 2	6 42	na	2 5	1 47	7 47	7.27	6.73

NOTES: [1] na = not available; < = not detected (less than "practical reporting limit"); Field chemistry of samples for high fluoride study (11/8/01 to 12/5/01) are reported in Table 6.3.4.5-1 of BSC (2002 [160771]).

[2] See entry in Table 6.3.4.1-1 of BSC (2002 [160771]) for temperature of pH measurements.

[3] HCO_3^- - field measurement.

[4] Pore water samples (baseline): sample ultracentrifuged from borehole core.

[5] Low detection limit analysis - sample filtered to 0.10 mm and acidified.

[6] Sample filtered in the field and laboratory (LLNL) prior to analyses.

[7] Sample ID SPC0057028 submitted for low detection for Al analysis.

[8] Analytical results are corroborating data (as defined in Section 3.6 of AP-SIII.3Q) and non-qualified.

See Table 7-1 for Source DTNs.

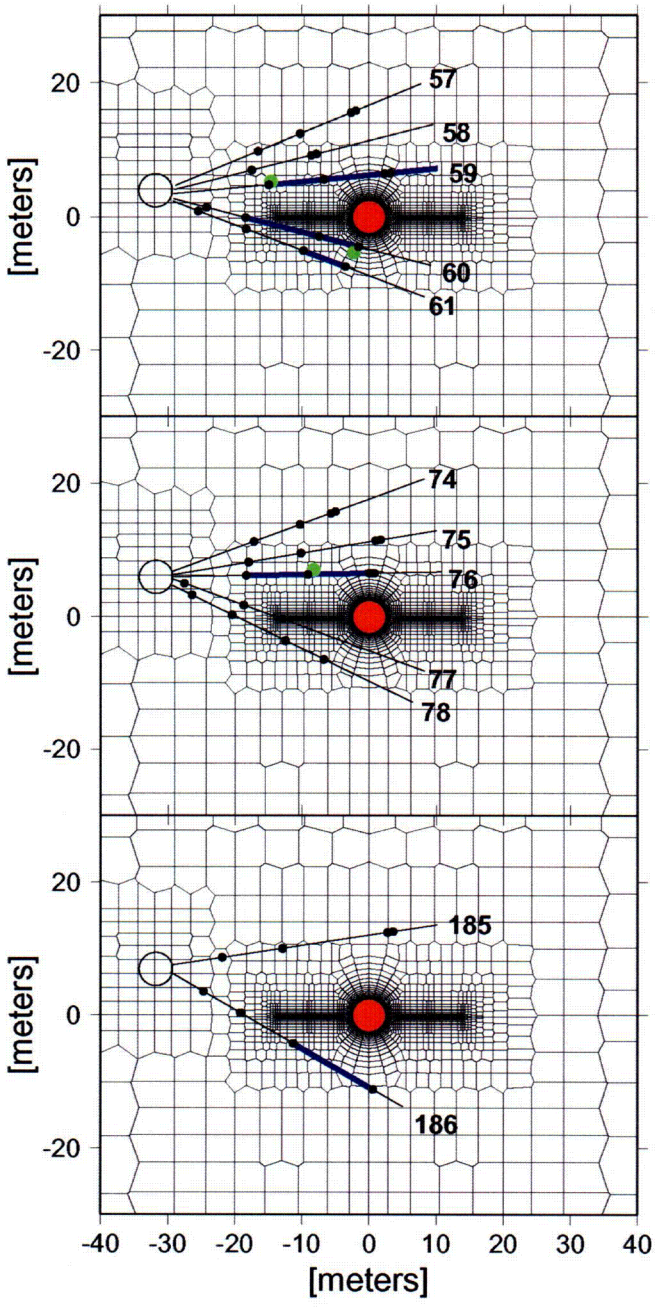

DTNs: LB0307DSTTHCR2.001 (mesh—Output-DTN), MO0002ABBLSLDS.000 [147304] (sensors and boreholes)

Source: BSC (2002 [160771]) - water collection locations.

NOTE: Only those waters having the distinct criteria discussed in this section were considered to have been liquid in the borehole. Locations where comparisons were made to measured compositions are shown as green circles. The Heater Drift is shown in red.

Figure 7.1-13 Zones Where Water Was Collected from Hydrology Boreholes Superimposed (Thick Shading in Blue) on the Model Grid

C110

Some of the processes that could explain the water chemistry of samples collected in the hydrology boreholes include mixing of pure condensate water with fracture pore waters, equilibration of condensate waters with matrix pore waters via molecular diffusion, reaction of condensate waters with fracture-lining minerals, and mineral precipitation. Waters that were collected from the hydrology boreholes at elevated temperatures are generally more dilute (lower Cl^- and SO_4^{2-}) and lower in pH than the initial pore water. Aqueous silica concentrations are similar to or much higher than in the pore water, indicating that these waters are not simple mixtures of pore water and pure condensate water. Some clear trends in water chemistry of the condensate waters over time are increases in pH and SiO_2 (aq) concentration and a drop in Ca^{2+}. The higher silica concentration in the waters collected at later times in several boreholes (and at higher temperatures), relative to chloride and the initial pore-water silica concentration, is consistent with dissolution of a silicate phase, rather than with increased concentration via boiling. Concentrations of K^+, Mg^{2+}, and Na^+ are also higher than what would be expected by dilution of original pore water (as evidenced by the low chloride concentrations). Therefore, the silicate phases that dissolved must have been some combination of silica polymorphs (i.e., opal, cristobalite, tridymite, and quartz) and feldspar, clays, or zeolites, rather than just a pure silica phase. Many of the waters show a drop in Ca^{2+} over time, consistent with calcite precipitation as the water was heated further and underwent CO_2 degassing.

These water samples are considered to be representative of fracture waters produced by THC processes in the region around the DST. However, the borehole intervals from which the waters were collected are approximately 8-10 m in length and at times have temperatures several tens of degrees different at each end (also see Section 7.1.7). Therefore, vapor flow from the hot end to the cool end of an interval, accompanied by condensation and reaction with the rock lining the borehole, could account for some of the water found in the boreholes. Because the borehole surface mineralogy is not identical to the fracture surface mineralogy, the water chemistry in the borehole may have some differences to the chemistry of water in the fractures. Yet, because the rock surface in the borehole was freshly drilled, it may be more reactive with respect to silicate mineral reactions, hence potentially producing higher concentrations of species making up the silicate mineral phases. The fresh mineral surfaces in the borehole could therefore result in dissolution rates greater than that in the fractures even though the surface area of the smooth borehole is likely to be less than that of the irregular fracture surface.

Further discussion of water chemistry in the DST and comparisons to model results is given in the following section (Section 7.1.11.2). In REV01, model results were compared to water collected from borehole intervals 59-2 (above the heaters) and 60-3 (below the heaters). In REV02, model results are compared to a more complete data set from these intervals and also to borehole interval 76-3, which is above the heaters in an array closer to the area where the maximum drift crown temperature was reached (30 m from the bulkhead). Waters were collected from other borehole intervals, but on only one or two occasions. Compositional trends from so few samples cannot be discerned, nor is validation of the model by comparison to these samples very useful. However, they do provide additional information on the range of potential water compositions.

7.1.11.2 Evolution in the pH of Waters from the DST

In this section, model simulations of the evolution of pH in space and time are shown, followed by comparisons of pH measurements of waters collected from boreholes and model results at specific locations. The pH of waters in the rock is a function of the coupled thermal, chemical and transport processes taking place in the fractures and matrix as the system undergoes heating. The water chemistry can also be affected near rock interfaces, such as at the drift wall. Here, exchange of atmospheric air with gas in the rock takes place via advective transport and diffusion, or by simple degassing of water owing to barometric pressure changes.

The modeled spatial distribution of pH (using the REV02 input data) in fracture water at various times during the heating phase is shown in Figure 7.1-14. The times correspond approximately to the dates when water was sampled from hydrology borehole intervals, which are also highlighted. Based on the compositions of ambient pore water ultracentrifuged from the rock in the DST block, the pH of waters in the region of the DST likely started out between approximately 7.8 and 8.3 (Table 7.1-3). The initial pH of the water used in the DST THC Model simulation is approximately 8.3. The most obvious effect of heating is a reduction in pH to about 7.2 in the condensate region, corresponding approximately to the increases in CO_2 concentrations shown in Figure 7.1-11. As for the CO_2 concentrations, the low pH zone increases in size and moves outward with time. Close to the dryout zone, the pH of the water increases, owing to boiling, degassing, and outward transport of the CO_2. Another important factor affecting the pH is the reaction rates of certain minerals, such as feldspars, that upon dissolution consume H^+, resulting in a rise in pH. Clearly, the significantly higher pH values of waters sampled from the boreholes, compared to the very dilute low pH waters formed from vapor condensing in the sample collection tubes, attests to the strong effect of mineral-water reactions on the pH.

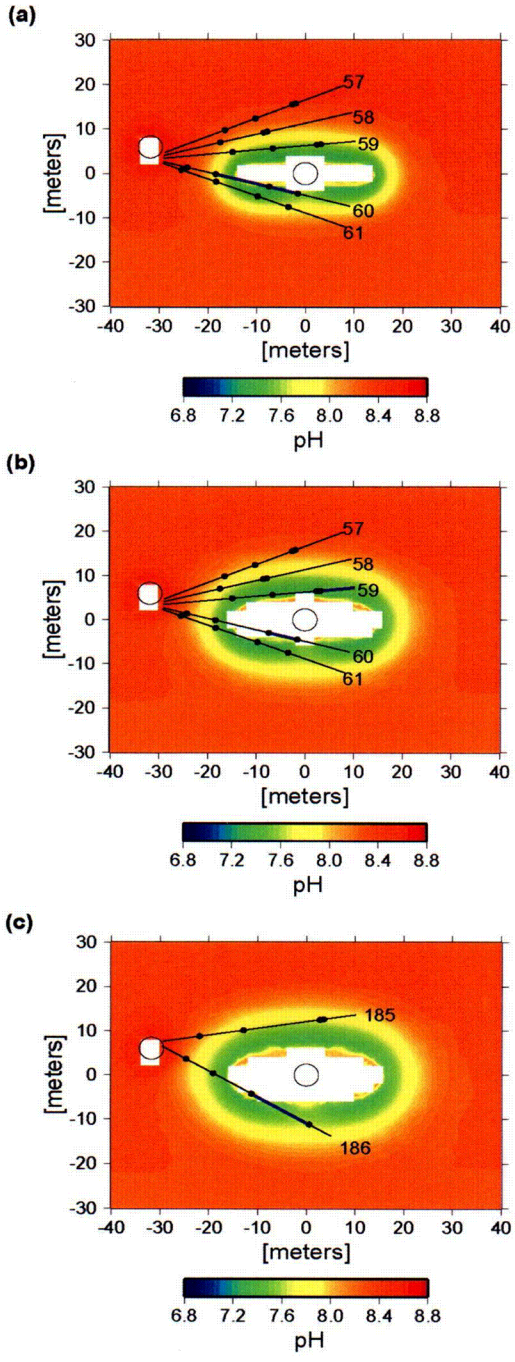

Output-DTN: LB0307DSTTHCR2.001 (modeled)

Source: BSC (2002 [160771], Table 6.3.4.1-1)-water collection locations.

NOTE: The intervals where water was sampled are more thickly shaded (in blue). Areas of zero liquid saturation are blanked out in white.

Figure 7.1-14. Modeled Distribution of pH in Fractures at Various Times When Water Was Sampled from Hydrology Borehole Intervals (REV02 Simulation): (a) 6 Months, (b) 11 Months, and (c) 14 Months

Figures 7.1-15a and b show the evolution of pH in the sampled waters compared to the modeled base-case and extended systems (REV01 simulations). Modeled pH values are given for the temperature in the rock, whereas field measurements of pH are reported for the temperature at the time of the measurement. The temperatures at which the pH was measured were typically much lower than that in the rock where the sample originated (BSC 2002 [160771], p. 6.3-42). This could result in greater differences between modeled and measured pH values, but the effect is uncertain because several competing processes could be taking place as the water is sampled. These processes include (1) degassing of CO_2 from the water leading to an increase in pH, (2) condensation of water vapor under higher partial pressures of CO_2 and mixing with the water leading to a decrease in pH, and (3) equilibration of water in equilibrium with a lower partial pressure of CO_2 than the atmosphere with air in the Observation Drift, leading to an increase in pH. Certainly, some vapor condensation is likely to have affected some samples more than others, as evidenced by the many water samples that formed solely from condensation in the sampling tubes.

The early trend to lower pH is related to the addition of condensate to this area and to increases in CO_2 in the gas phase (caused by boiling closer to the heaters and diffusive and advective gas transport outwards). Later increases in pH are related to boiling of the water in this area, leading to a reduction in CO_2 concentrations as the temperature reaches boiling and the zone finally dries out. The model results for interval 60-3, showing complete dryout at approximately 18 months, are consistent with the observation that water was absent from this interval shortly after the last sample was collected, after 16 months of heating. In spite of these uncertainties (and those discussed in Section 7.1.7), both geochemical systems capture the trend in pH of fracture waters in this region. However, the base-case system captures the drop in pH more closely than the extended system. The system without calcite also shows a reasonable match to the measured pH values compared to the other simulations.

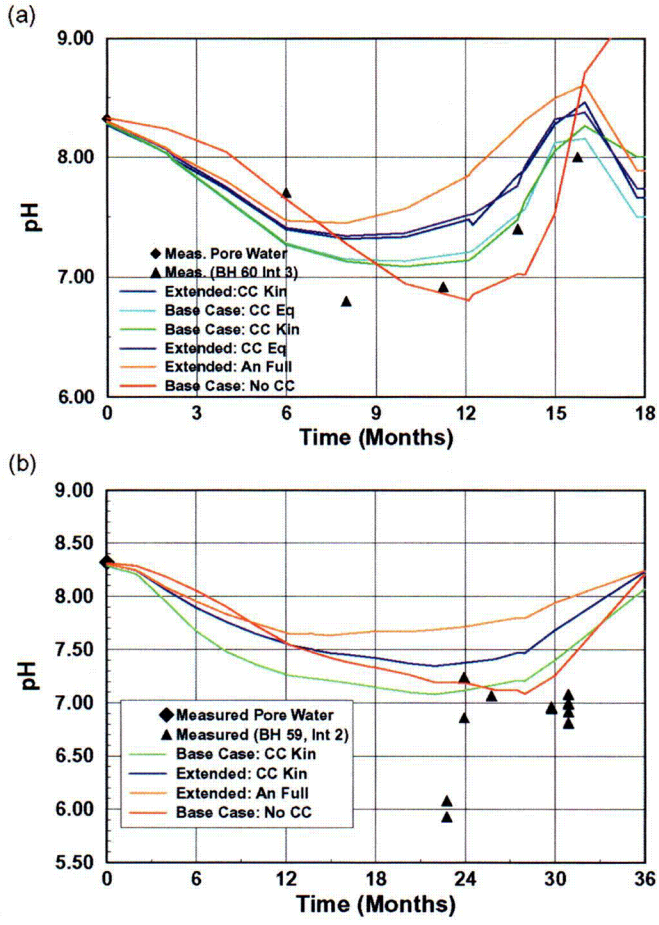

DTNs: LB0011DSTTHCR1.002 [161282] (simulated)
LL020709923142.023 [161677] (measured)

NOTE: The ambient pore-water pH is approximately 8.3. "CC" refers to calcite.

Figure 7.1-15. Changes in pH in Water Samples Collected from Borehole Intervals (a) 60-3 and (b) 59-2 Compared to REV01 Modeled Fracture Water pH at Nearby Model Grid Nodes

C112

Results for the REV02 model system are shown for borehole intervals 60-3, 59-2, and 76-3 in Figure 7.1-16. The modeled trends in pH are similar to those in the REV01 extended case and to the measured pH values. However, the minimum pH is not as low as that measured, nor as low as the base-case pH. Yet the differences between the measured and modeled pH values are generally less than one pH unit, within a fairly narrow range of approximately pH 6 and pH 8. In 59-2 and especially in 76-3, the drop in pH is considerably earlier than in the measured pH values. Part of this discrepancy is related to the higher modeled temperatures after one year (compared to those measured) resulting in an earlier arrival of the condensation "pulse" from the advancement of the boiling zone. Higher pH values may also result from the larger reaction rates for aluminosilicates at higher temperatures. In addition, local permeability heterogeneity could result in earlier or later changes because of the flow of gas and or water preferentially through large fractures. Except for a few samples with lower pH values, the minimum pH values in the model results are within one pH unit of the minimum values measured. Given all of the uncertainties in the collection of water samples, and in the comparison of the model results to measured values (see Section 7.1.7 and previous discussion in this section), the requirements for model validation (one pH unit and trends where observable) have been met.

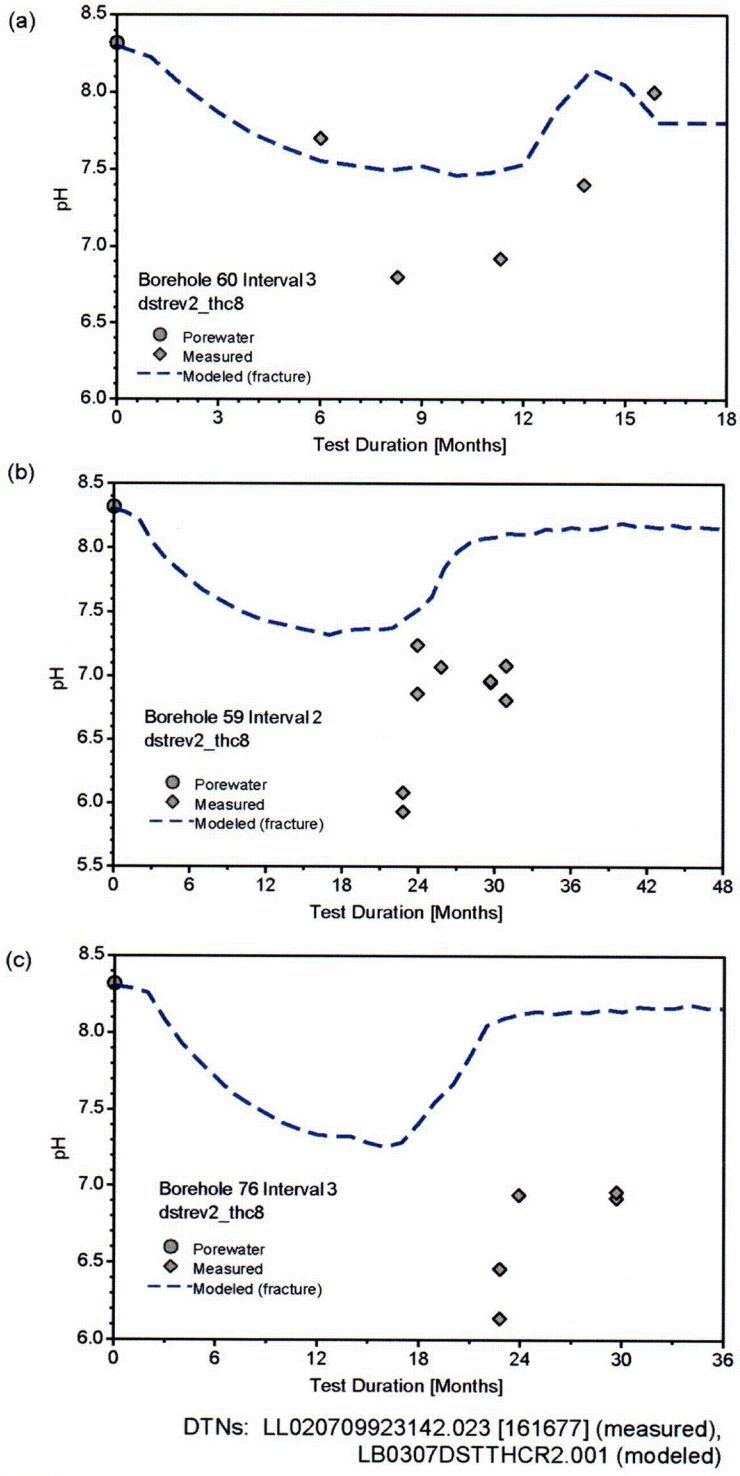

DTNs: LL020709923142.023 [161677] (measured),
LB0307DSTTHCR2.001 (modeled)

NOTE: The ambient pore-water pH is approximately 8.3.

Figure 7.1-16. Comparison of Measured pH in Water Samples Collected from Borehole Intervals (a) 60-3, (b) 59-2, and (c) 76-3 to REV02 Modeled Fracture Water pH at Representative Model GridBlocks

7.1.11.3 Evolution of Anion and Cation Concentrations

The effects of dilution through condensation of pure water vapor, increases in concentration caused by boiling, and fracture-matrix interaction can be assessed by examining the variation in conservative species such as chloride (Cl^-) and sulfate (SO_4^{2-}). These species are conservative because chloride and sulfate-bearing minerals, such as halite and gypsum (or anhydrite), are not present in the rock initially and precipitate under more saline conditions, expected only at the final drying stages of the dilute waters observed in the rock at Yucca Mountain. In this section, results are compared from the REV01 and REV02 model systems to measured concentrations. For conservative anions, the primary differences seen in concentrations between the two revisions should be a result of the different hydrological properties, because the initial water compositions are the same. Primarily, the lower matrix permeability (about one order of magnitude less) in the REV02 hydrological property set resulted in a smaller rate of gas flow out of the matrix into fractures and thus lower fracture saturations.

The modeled spatial variations in Cl^- concentrations in fracture and matrix are plotted in Figure 7.1-17 (REV02 simulation), at times of 1 year and 4 years during the heating phase. The main effect is a marked decrease in Cl^- concentrations within fractures in the condensation and drainage zones. In the matrix, there is significant dilution in the condensation zones, and significant increases in concentration near the edge of the dryout zone. Differences in the hydrological properties used in REV01 did not fundamentally change the spatial pattern of conservative anion concentrations, and therefore REV01 results are not shown as contour plots. However, differences between REV01 and REV02 concentrations are evident in the plots of concentrations over time at particular borehole interval locations, shown below.

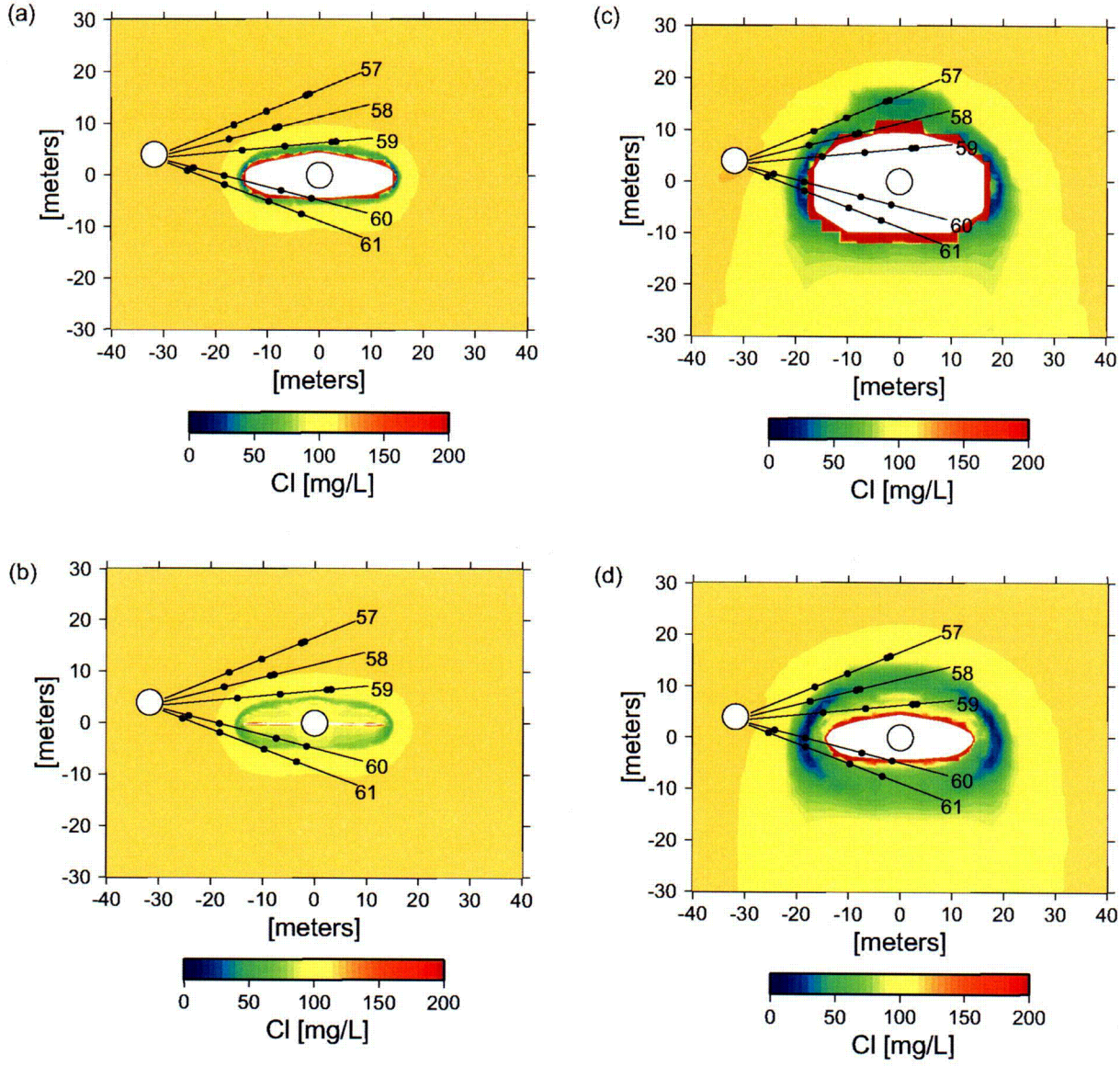

Output-DTN: LB0307DSTTHCR2.001

NOTE: Areas of zero liquid saturation are blanked out in white.

Figure 7.1-17. Modeled Distribution of Cl^- in Fractures and Matrix at One and Four Years during the Heating Phase of the DST (REV02 Simulation): (a) Fracture—1 year, (b) Matrix—1 Year, (c) Fracture—4 years, and (d) Matrix—4 years

C114

REV01 modeled variations in Cl^- are shown in Figure 7.1-18a,b and for SO_4^{2-} in Figure 7.1.19a,b. The model results capture the overall extent of dilution, or fracture-matrix interaction in the system (compared to the initial matrix pore water), for both chloride and sulfate. The largest discrepancy in interval 60-3 is at the earliest time, when the first waters collected are more dilute than the modeled fracture waters. However, compared to the modeled concentrations of Cl^- and SO_4^{2-} in matrix water, the fracture waters are more dilute and quite similar to the samples collected from the boreholes. It is expected that waters found in boreholes should be similar to fracture water and not to matrix water, because the matrix permeability is too low to allow significant water movement. In borehole interval 59-2, the earliest collected samples are more closely matched than the later collected samples, although the overall trend is still captured reasonably well. The sharp increase in modeled concentrations at later times is a result of boiling and evaporative concentration. Ionic strengths eventually reach values greater than those for which accurate aqueous species activities are calculated (maximum ionic strengths of approximately 2 to 6). However, under such conditions, modeled water saturations are generally well below the level (< 1%) where significant amounts of water are present and would be collected.

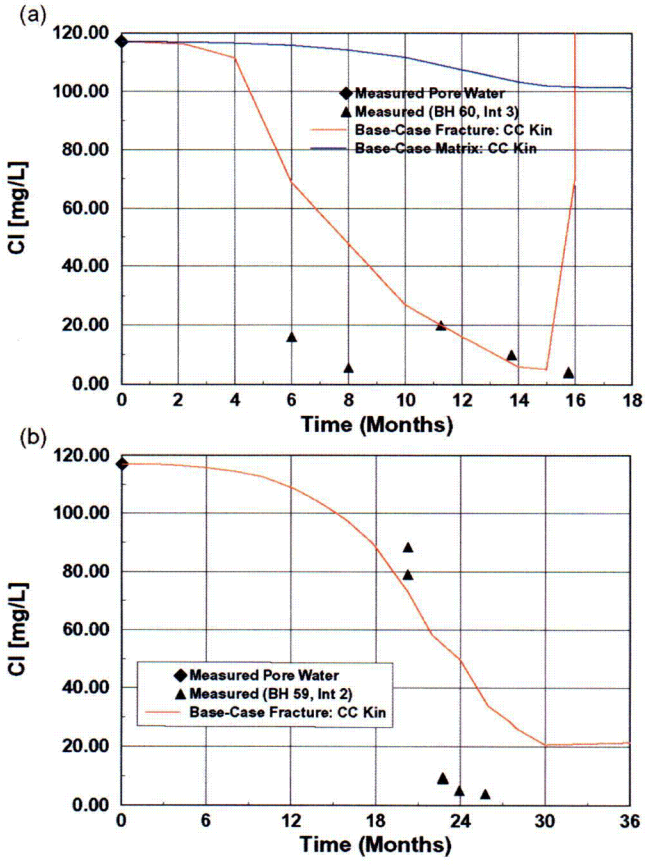

DTNs: LB0011DSTTHCR1.002 [161282] (simulated),
LL020709923142.023 [161677] (measured)

Figure 7.1-18. Changes in Cl^- (mg/L) in Water Samples Collected from Borehole Intervals (a) 60-3 and (b) 59-2, Compared to REV01 Modeled Fracture Water Cl^-

C115

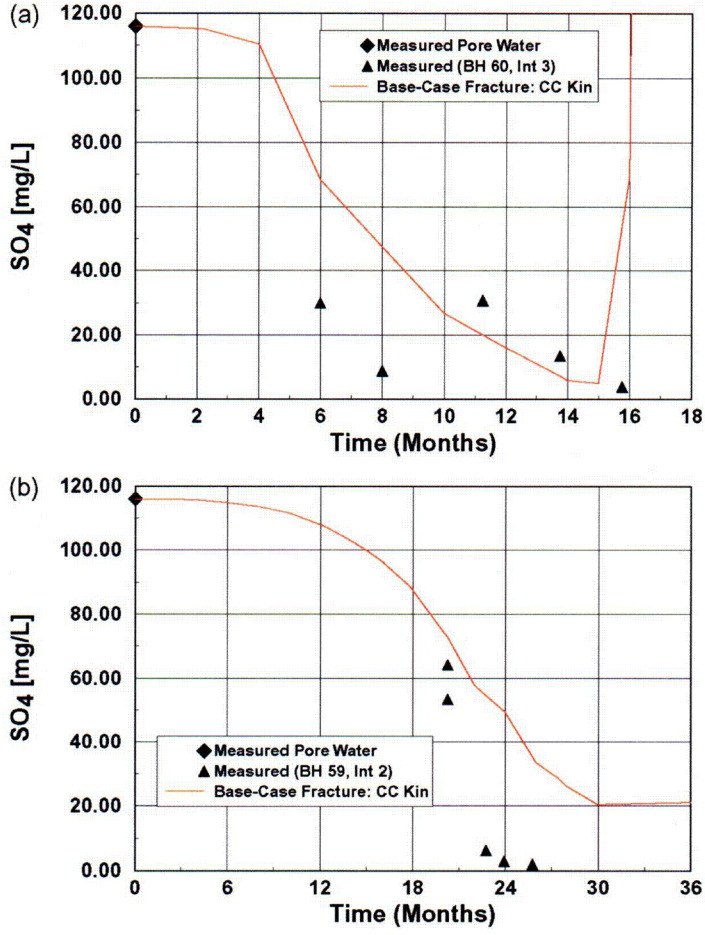

DTNs: LB0011DSTTHCR1.002 [161282] (simulated),
LL020709923142.023 [161677] (measured)

Figure 7.1-19. SO_4^{2-} Concentrations (mg/L) in Water Samples Collected from Borehole Intervals (a) 60-3 and (b) 59-2, Compared to REV01 Modeled Fracture Water SO_4^{2-}

In comparison, Cl^- and SO_4^{2-} concentrations from the REV02 simulation (Figures 7.1-20 and 7.1-21) do not match the pattern of measured concentrations as well as the REV01 results, nor do they reach the low values observed. This can be attributed to the different hydrological properties, which in REV02 led to large pressure buildups in the matrix and less vapor transport out of the matrix. The reduction in vapor transport out of the matrix led to lower liquid saturations in the fractures and a weaker dilution effect on the ambient fracture pore water. Despite these differences, the trends are to more dilute compositions compared to the pore water, and many measured concentrations are within an order of magnitude of the modeled values. Therefore, the DST THC Model meets the model validation requirements for chloride and sulfate concentrations.

C116

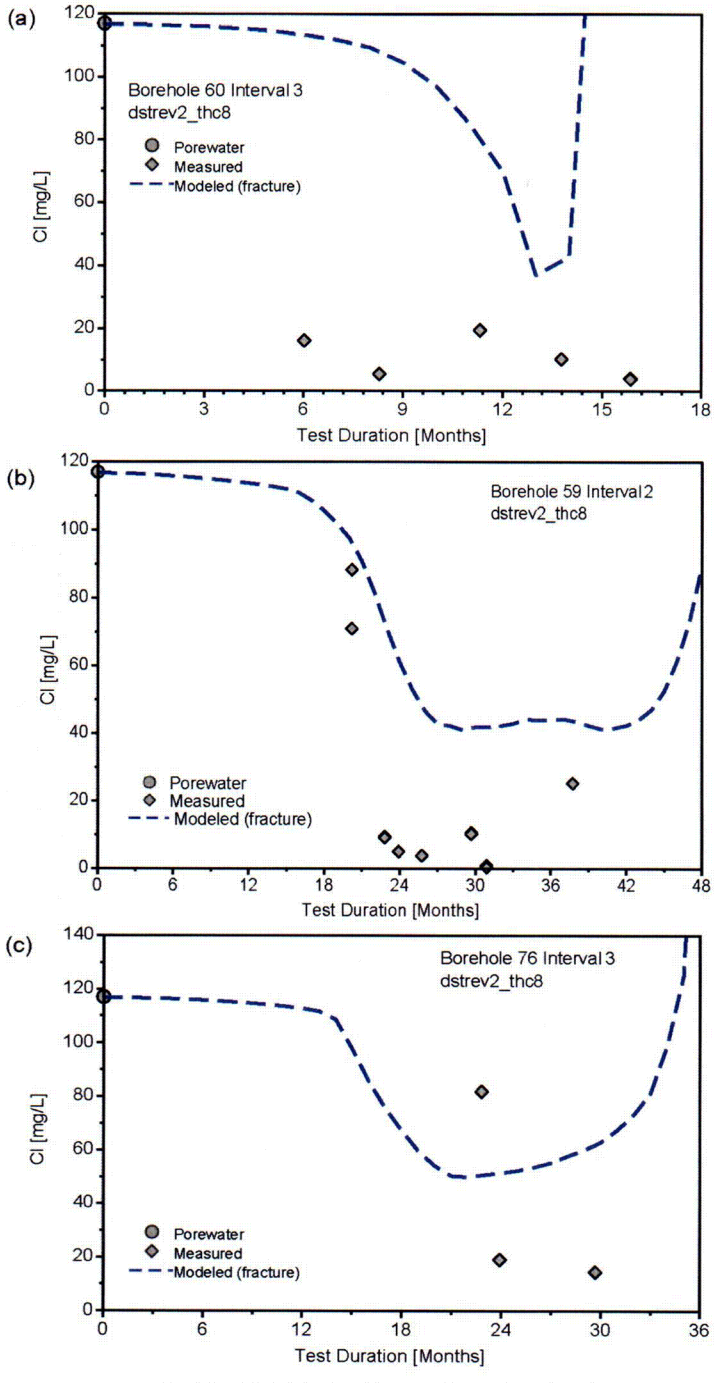

DTNs: LL020709923142.023 [161677] (measured),
LB0307DSTTHCR2.001 (modeled)

Figure 7.1-20. Cl^- Concentrations (mg/L) in Water Samples Collected from Borehole Intervals (a) 60-3, (b) 59-2, and (c) 76-3 Compared to REV02 Modeled Fracture Water Cl^-

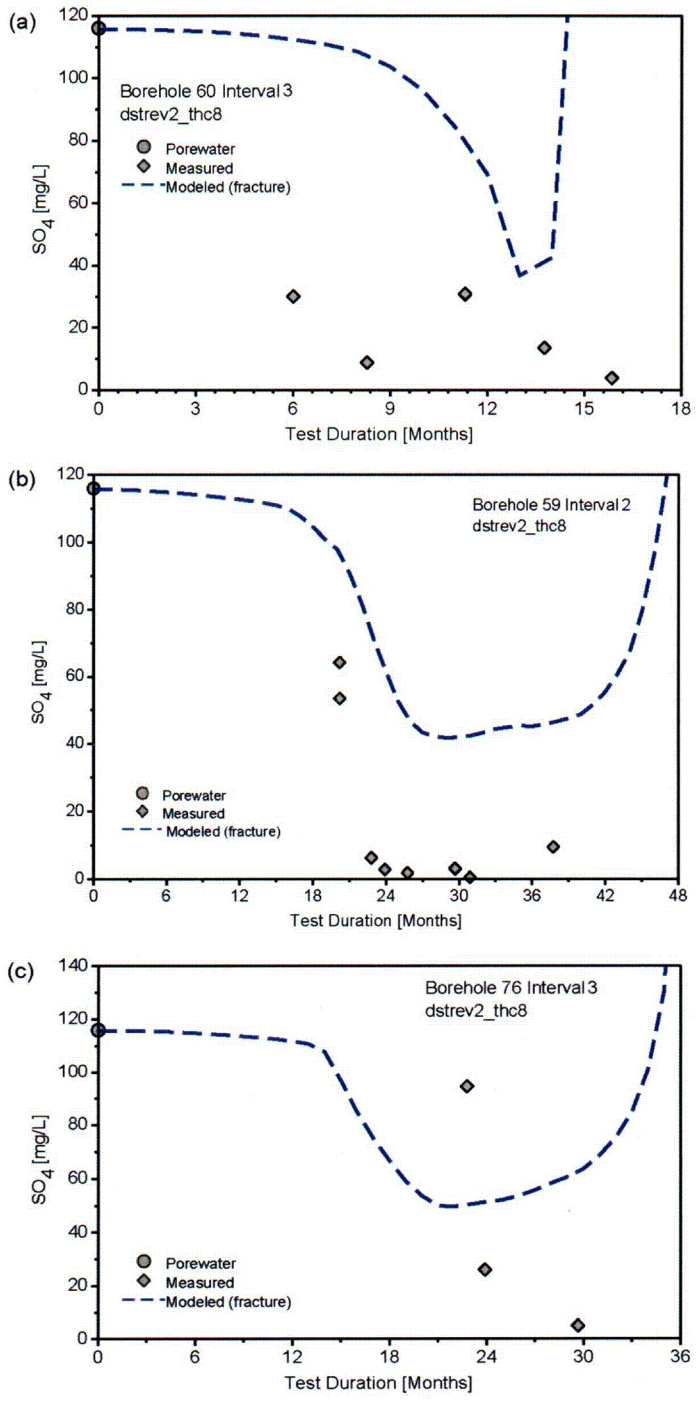

DTNs: LL020709923142.023 [161677] (measured),
LB0307DSTTHCR2.001 (modeled)

Figure 7.1-21. SO_4^{2-} Concentrations (mg/L) in Water Samples Collected from Borehole Intervals (a) 60-3, (b) 59-2, and (c) 76-3 Compared to REV02 Modeled Fracture Water SO_4^{2-}

C118

Measured sodium concentrations (Na^+; Figures 7.1-22a,b) are also much lower than in the initial pore water and are close to the REV01 modeled concentrations. However, the extent of dilution in interval 60-3 is by only a factor of about three to six times, whereas for Cl^- it was from about six to about 20. This difference indicates some contribution of water-rock interaction to the Na^+ concentrations, which is shown in the REV01 extended-case model results as a shift to higher Na^+ concentrations from the base-case results. The origin of the sodium in the DST waters could be alkali feldspar and/or reaction or exchange with clays. In the model simulations, the main source of Na^+ is from alkali feldspar dissolution. As in the Cl^- and SO_4^{2-} variations over time, the sharp rise to higher concentrations at later times is a result of rapid dryout.

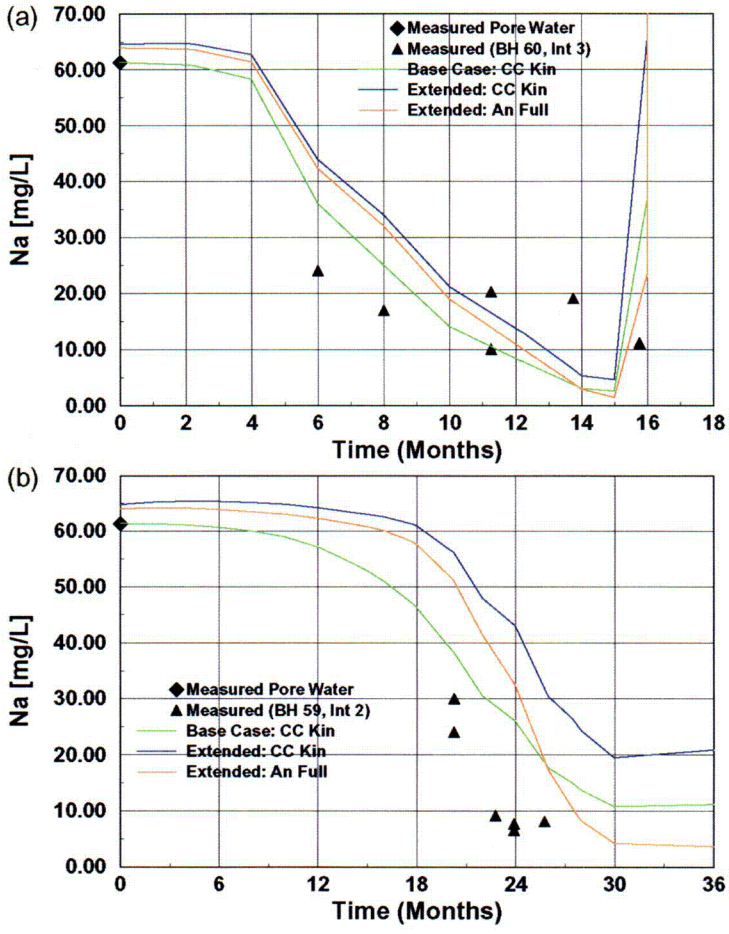

DTNs: LB0011DSTTHCR1.002 [161282] (simulated),
LL020709923142.023 [161677] (measured)

Figure 7.1-22. Na^+ Concentrations (mg/L) in Water Samples Collected from Borehole Intervals (a) 60-3 and (b) 59-2, Compared to REV01 Modeled Na^+ Concentrations in Fractures

Na^+ concentrations in the REV02 simulation (Figure 7.1-23) are elevated with respect to the REV01 results and the modeled concentrations in the 60-3 and 59-2 boreholes, but are closer to the measured values in borehole interval 76-3. The shape of the modeled Na^+ curve shows an increase with temperature, prior to the main condensation pulse, which was absent in the REV01 simulated Na^+ concentrations. This increase clearly results from the higher reactivity of albite, which also leads to increases in pH and a reduction in the partial pressure of CO_2. In the actual rock, it is likely that albite had undergone preferential weathering over several million years of infiltration and is coated by later-formed clays, silica polymorphs, and Ca-rich zeolites. Although the comparisons are not as good as those for REV01, most samples are within the model validation criteria.

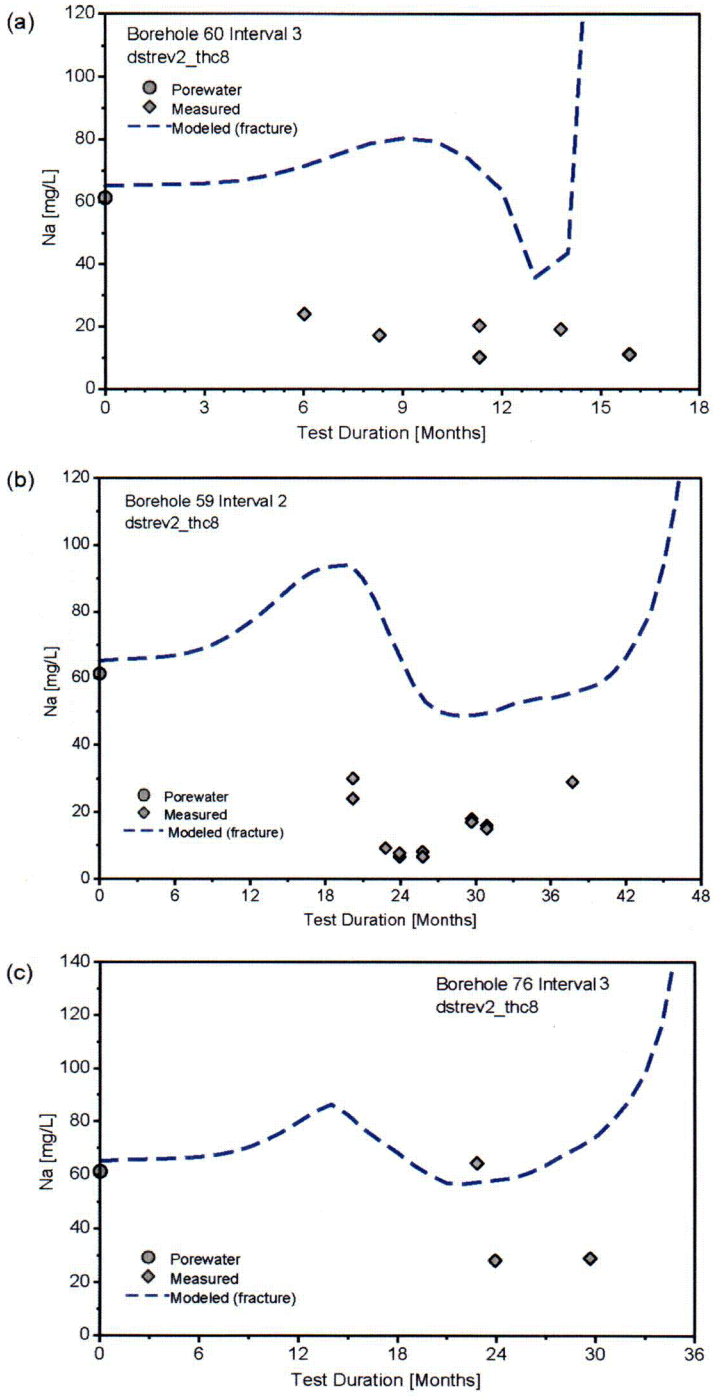

DTNs: LL020709923142.023 [161677] (measured),
LB0307DSTTHCR2.001 (modeled)

Figure 7.1-23. Na^+ Concentrations (mg/L) in Water Samples Collected from Borehole Intervals (a) 60-3, (b) 59-2, and (c) 76-3 REV02 Modeled Na^+ Concentrations in Fractures

Calcium is more sensitive to water-rock interaction than some other species because of the fast reaction rate of calcite, its lower solubility with increasing temperature, and the common occurrence of calcite in fractures. Other potential sources of Ca^{2+} in the rock include Ca-rich zeolites, such as stellerite that are abundant in fractures. Waters collected from intervals 60-3 and 59-2 show a significant drop from the pore-water concentration (about 100 mg/L) to below 10 mg/L, with a consistent decrease over time in 60-3 (Figure 7.1-24a). The continued drop in Ca^{2+} in 60-3 and the very low concentrations in 59-2 (Figure 7.1-24b) may be caused by calcite precipitation, because of its decreased solubility with increasing temperature. The model results in Figures 7.1-24a and b also show a similar, but smaller, reduction in calcium concentration.

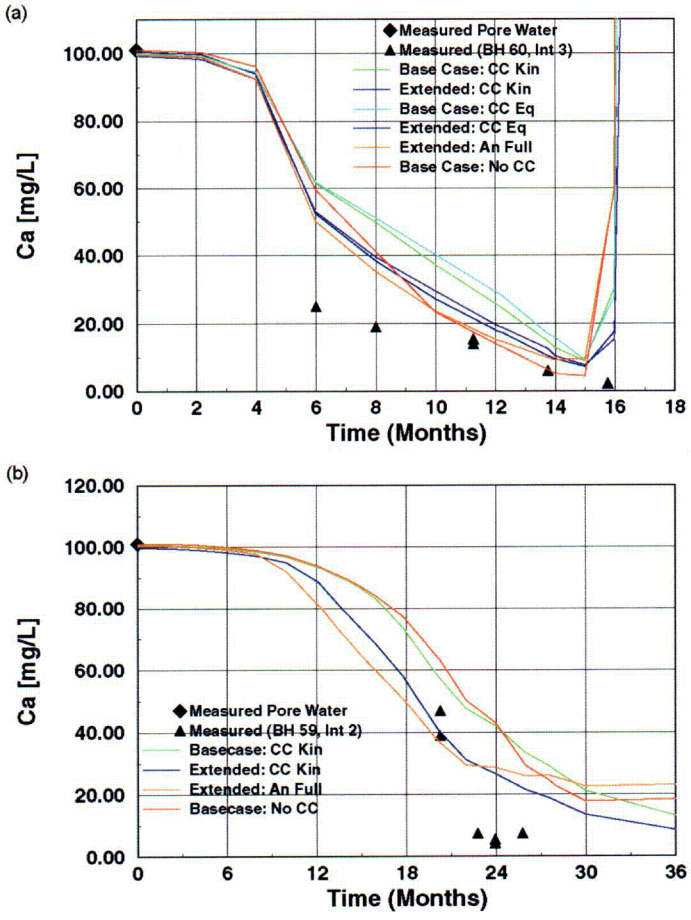

DTNs: LB0011DSTTHCR1.002 [161282] (simulated),
LL020709923142.023 [161677] (measured)

Figure 7.1-24. Ca^{2+} Concentrations (mg/L) in Water Samples Collected from Borehole Intervals (a) 60-3 and (b) 59-2 Compared to REV01 Modeled Ca^{2+} in Fracture Water

Ca^{2+} concentrations in the REV02 simulation (Figure 25a,b,c) are slightly elevated with respect to the REV01 results and the modeled concentrations in the 60-3 and 59-2 boreholes, but are close to the measured values in all the boreholes. The shape of the REV02-modeled Ca^{2+} curve in 60-3 does not exhibit as early an initial dilution-induced drop in concentration; instead, the reduction occurs later, when the strong condensation pulse is encountered and increasing temperature results in calcite precipitation. Similar to the REV01 results, the Ca^{2+} concentration

C121

increases as boiling proceeds and the remaining water is evaporated. The model results capture the trend in the Ca^{2+} concentrations and are, in most cases, within one order of magnitude of the measured values. Therefore, the validation criteria for Ca^{2+} in the DST THC Model have been met.

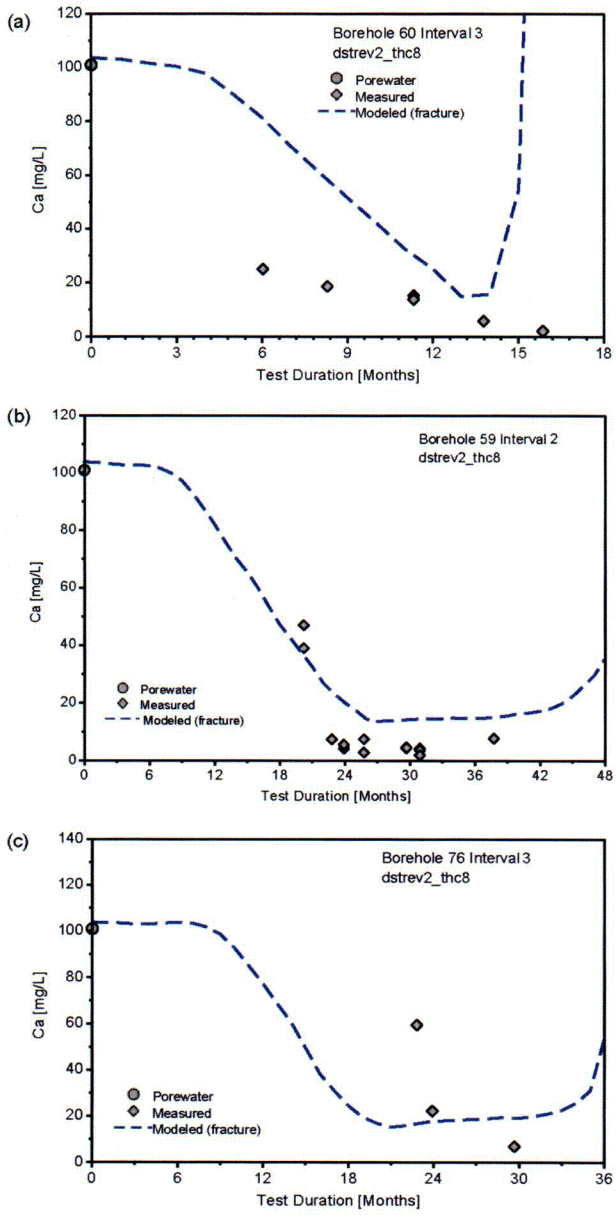

DTNs: LL020709923142.023 [161677] (measured),
LB0307DSTTHCR2.001 (modeled)

Figure 7.1-25. Ca^{2+} Concentrations (mg/L) in Water Samples Collected from Borehole Intervals (a) 60-3, (b) 59-2, and (c) 76-3 Compared to REV02 Modeled Ca^{2+} in Fracture Water

C122

Measured silica concentrations (Figures 7.1-26a,b and 7.1-27a,b,c) show an increase to significantly higher concentrations in the borehole waters compared to the initial pore-water concentration. REV01 model concentrations in borehole interval 60-3 (Figure 7.1-26a) decrease to lower values, although the extent of dilution is moderated by water-rock reaction. In borehole interval 59-2, the extended-case results compare well with concentrations in those waters collected later (Figure 7.1-26b), although the earliest samples also had much higher concentrations. For comparison, modeled matrix silica concentrations for these same locations are similar to the measured values and trends, especially in interval 60-3. Because the concentrations of conservative species, such as chloride and sulfate, are close to the measured values, the possibility of greater fracture-matrix interaction is unlikely. Modeled Na^+ and K^+ concentrations also do not deviate substantially from measured values, suggesting that the additional silica is not likely to have been derived from increased dissolution of feldspars. Thus, the higher measured silica concentrations are likely to be a result of a higher effective reaction rate for a silica phase in the fractures (possibly opal-CT) or reaction of "fresh" mineral surfaces (i.e., cristobalite or quartz) in the borehole walls.

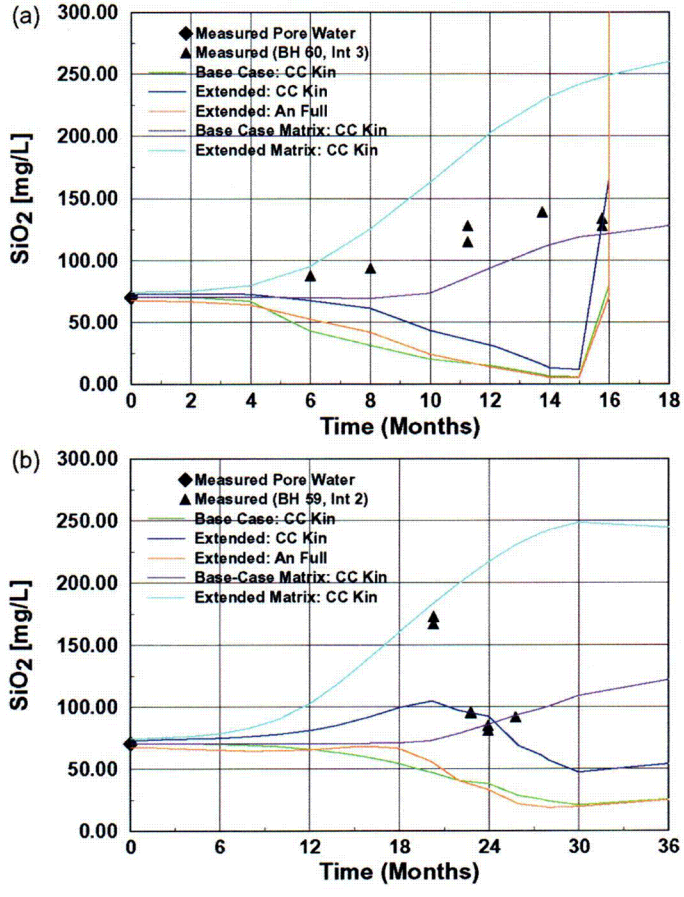

DTNs: LB0011DSTTHCR1.002 [161282] (simulated),
LL020709923142.023 [161677] (measured)

Figure 7.1-26. $SiO_{2(aq)}$ Concentrations (mg/L) in Water Samples Collected from Borehole Intervals (a) 60-3 and (b) 59-2 Compared to REV01 Modeled Fracture Water $SiO_{2(aq)}$ Concentrations

C123

In the REV02 simulations, the initial mineral assemblage was modified to include opal, reflecting its observed association with calcite in fracture coatings. The addition of this phase, along with the increased concentrations of species as a result of a weaker dilution effect and modifications to the thermodynamic data, resulted in much higher modeled aqueous-silica concentrations in the REV02 simulations (Figure 7.1-27a,b,c). The REV02 modeled silica concentrations in fracture waters capture the strong increases observed in the measured compositions, especially those seen in the borehole intervals overlying the heaters (59-2 and 76-3). In 76-3, the first water sample collected had a silica concentration of over 280 mg/L, compared to about 180 mg/L in the model simulation. The two waters collected later had silica concentration around 200 mg/L, which was closer to the REV02 model results. Except for two samples in 60-3, for which the model predicts an earlier rise in concentration, simulated SiO_2 values are within an order of magnitude of the observed ones, and therefore the model results meet the validation requirements.

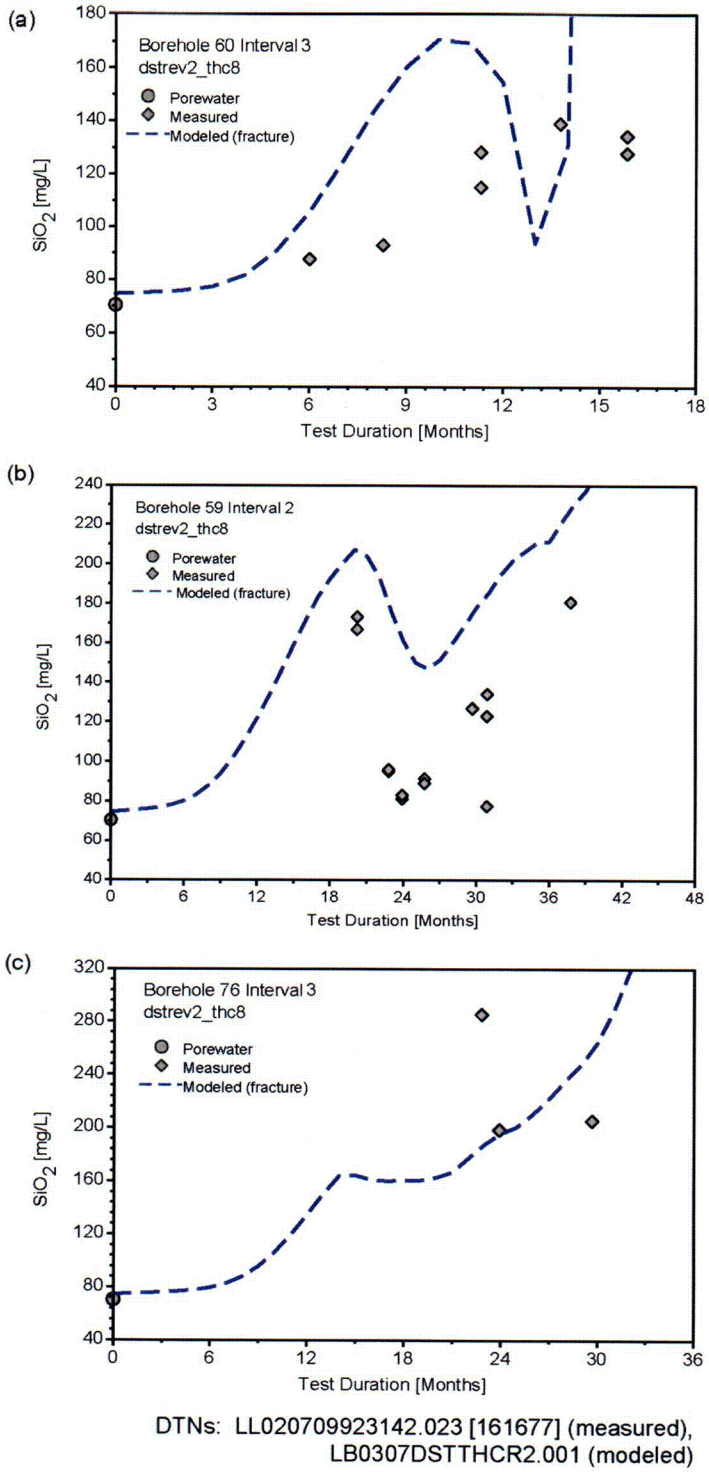

DTNs: LL020709923142.023 [161677] (measured),
LB0307DSTTHCR2.001 (modeled)

Figure 7.1-27. $SiO_{2(aq)}$ Concentrations (mg/L) in Water Samples Collected from Borehole Intervals (a) 60-3, (b) 59-2, and (c) 76-3 Compared to REV02 Modeled Fracture Water $SiO_{2(aq)}$ Concentrations

C124

REV01 modeled and measured potassium (K^+) concentrations are shown in Figures 7.1-28a and b for borehole intervals 59-2 and 60-3. REV01-modeled concentrations, although initially lower, quickly rise during heating and are similar to the measured values. A deviation occurs in K^+ at the initial time, because of some disequilibrium in the initial pore water with the model mineral assemblage. Measured concentrations in waters collected from the boreholes are significantly higher than would be expected from simple dilution of ambient fracture or matrix pore water, indicating that reactions with K-feldspar have likely taken place.

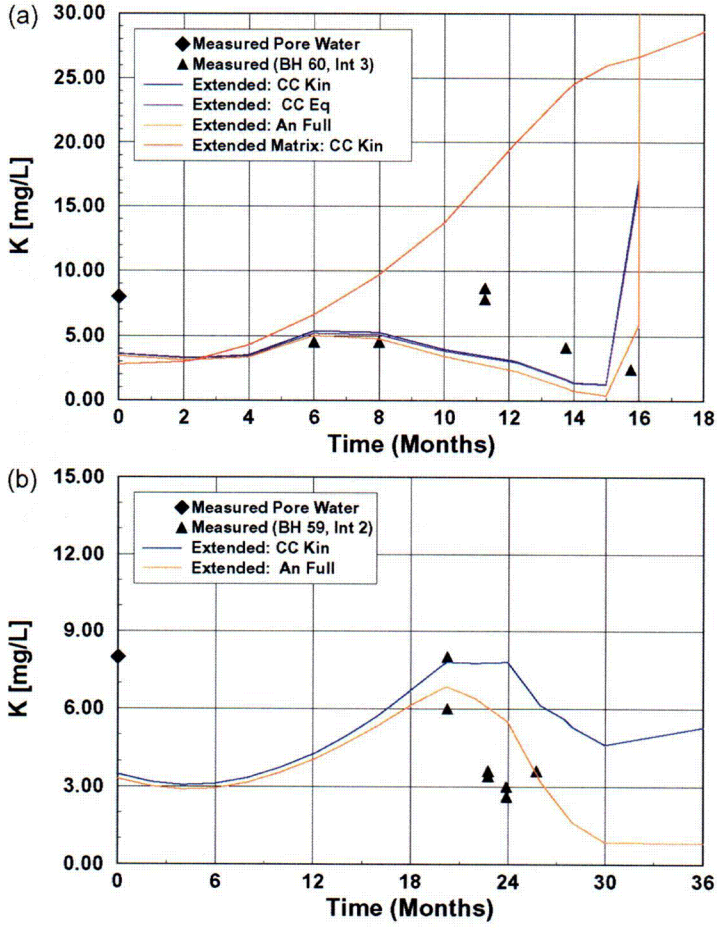

DTNs: LB0011DSTTHCR1.002 [161282] (simulated),
LL020709923142.023 [161677] (measured)

Figure 7.1-28. K^+ Concentrations (mg/L) in Water Samples Collected from Borehole Intervals (a) 60-3 and (b) 59-2 Compared to REV01 Modeled Fracture Water K^+ Concentrations

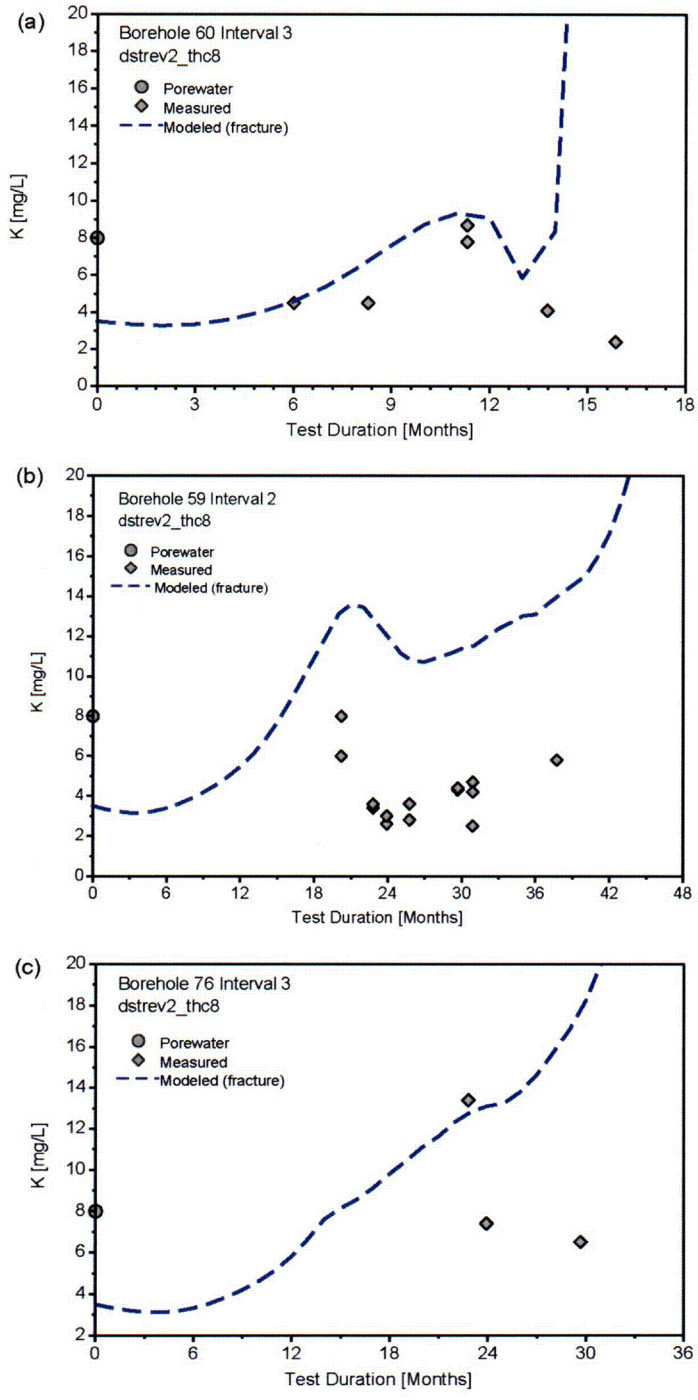

DTNs: LL020709923142.023 [161677] (measured),
LB0307DSTTHCR2.001 (modeled)

Figure 7.1-29. K^+ Concentrations (mg/L) in Water Samples Collected from Borehole Intervals (a) 60-3, (b) 59-2, and (c) 76-3 Compared to REV02 Modeled Fracture Water K^+ Concentrations

C126

REV02-modeled concentrations of K^+, like those of Na^+, increase to values somewhat higher than the measured concentrations. However, trends between modeled and measured data are similar, suggesting that a reduction in the K-feldspar reactivity and an increase in the dilution effect would result in a closer match to the measured concentrations. The modifications to hydrological and thermodynamic (and/or kinetic) data required for such reduction in reactivity would be consistent with the shifts needed for both the conservative species, such as Cl^- and SO_4^{2-}, as well as for Na^+. The lower matrix permeability used in REV02 induces slower transfer of pore water to enter into the fractures, and results in lower dilution of the conservative species. The inclusion of calcite and feldspar phases also increase the concentrations of silica, Na and K in the fractures.

The fact that Na^+ and K^+ show similar trends over time is consistent with their predominance in either an alkali feldspar solid-solution phase, such as sanidine, and/or as closely intergrown exsolved phases from a precursor solid-solution alkali feldspar mineral. All model results meet the validation requirements (trend to higher concentrations than in the initial pore water and within an order-of magnitude).

Fewer bicarbonate (HCO_3^-) concentrations were measured in the borehole waters because of difficulties making the measurements in the field. Available measurements are plotted in Figures 7.1-30a and b compared to the REV01 model results. Measured bicarbonate concentrations are much lower than the initial pore-water concentration, a pattern that is captured well by the model. This trend results from the combined effects of dilution and loss of dissolved CO_2 to the vapor phase at higher temperatures. Given the limited quantity of measured data, it is not possible to distinguish which geochemical system (base case or extended case) better predicts the bicarbonate concentration.

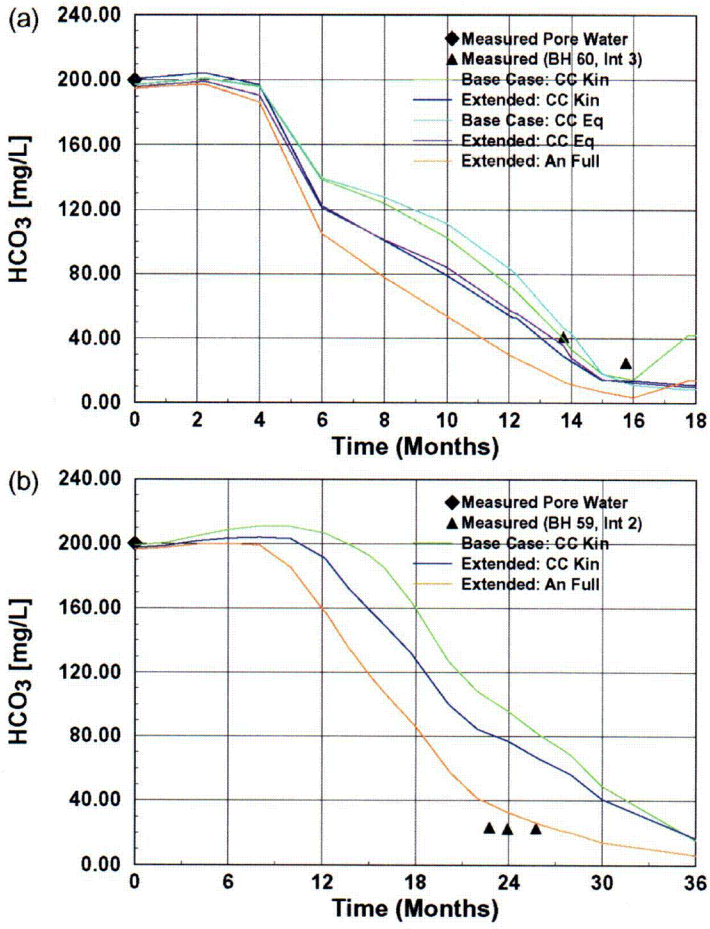

DTNs: LB0011DSTTHCR1.002 [161282] (simulated),
LL020709923142.023 [161677] (measured)

Figure 7.1-30. HCO_3^- Concentrations (mg/L) in Water Samples Collected from Borehole Intervals (a) 60-3 and (b) 59-2 Compared to REV01 Modeled Fracture Water HCO_3^- Concentrations

A few additional HCO_3^- concentrations were measured in borehole interval 59-2 and in interval 76-3 since the last revision of this document. These are plotted in Figure 7.1-31, along with REV02-modeled concentrations. REV02 HCO_3^- concentrations compare well to the measured concentrations. Another important aspect to the validation of the DST THC Model is that the REV01 model results are similar to the concentrations measured in 59-2 after the modeling was documented in the previous (REV01) model report. This prediction of the later measurements also supports the validation of the DST THC Model. Therefore, REV01 and REV02 model results for HCO_3^- meet the model validation criteria.

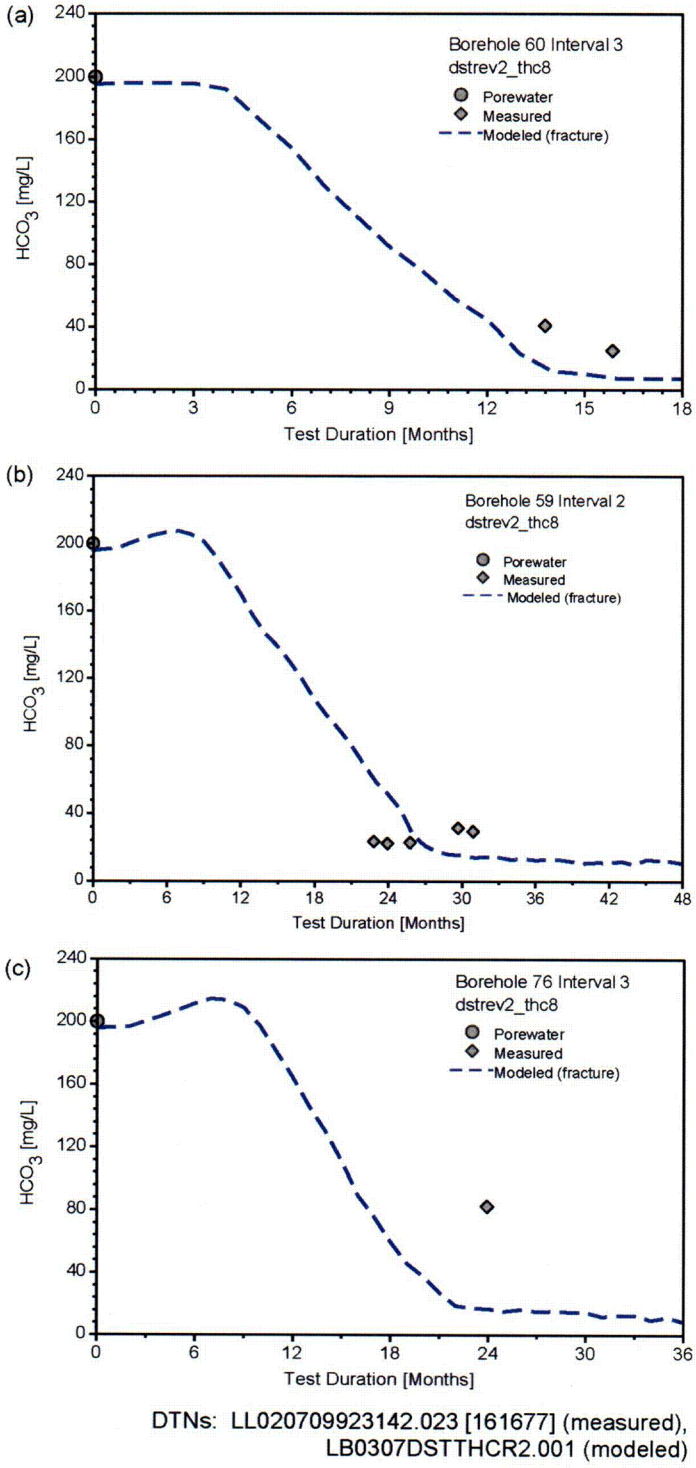

DTNs: LL020709923142.023 [161677] (measured),
LB0307DSTTHCR2.001 (modeled)

Figure 7.1-31. HCO_3^- Concentrations (mg/L) in Water Samples Collected from Borehole Intervals (a) 60-3, (b) 59-2, and (c) 76-3 Compared to REV02 Modeled Fracture Water HCO_3^- Concentrations

C128

Modeled concentrations of some additional aqueous species (Mg^{2+}, NO_3^-, and F^-) in the REV02 simulation are compared to measured compositions from 59-2, 60-3, and 76-3 in Figures 7.1-32 through 7.1-34.

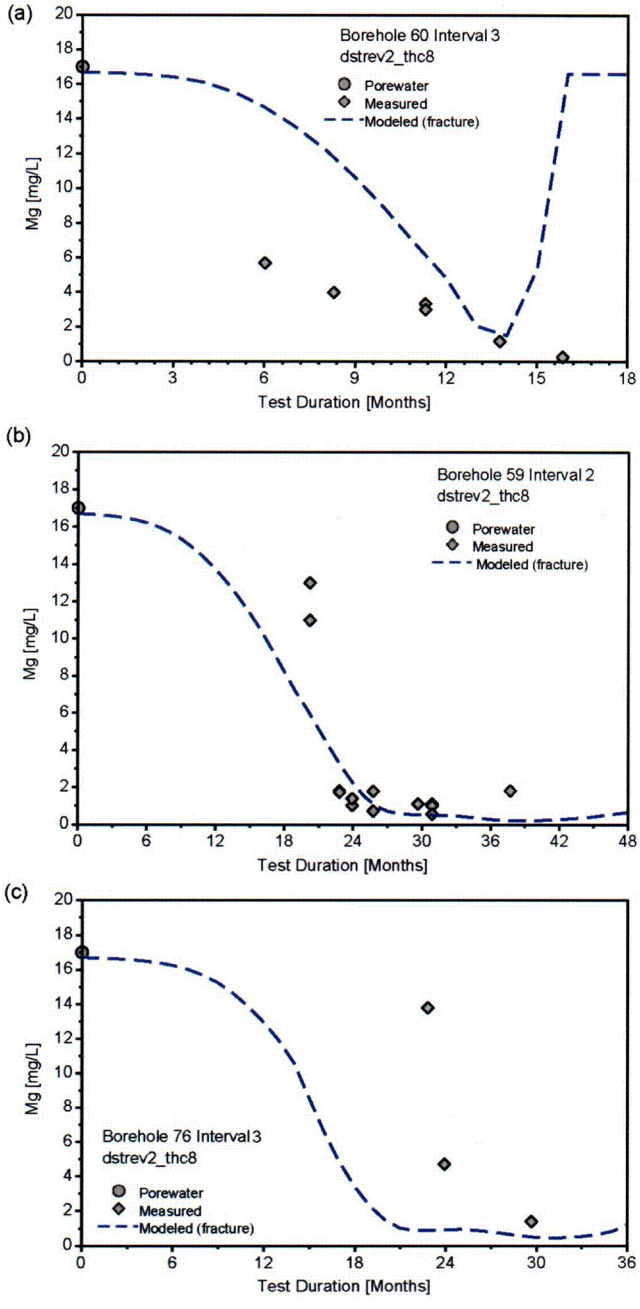

DTNs: LL020709923142.023 [161677] (measured),
LB0307DSTTHCR2.001 (modeled)

Figure 7.1-32. Mg^{2+} Concentrations (mg/L) in Water Samples Collected from Borehole Intervals (a) 60-3, (b) 59-2, and (c) 76-3 Compared to REV02 Modeled Fracture Water Mg^{2+} Concentrations

C129

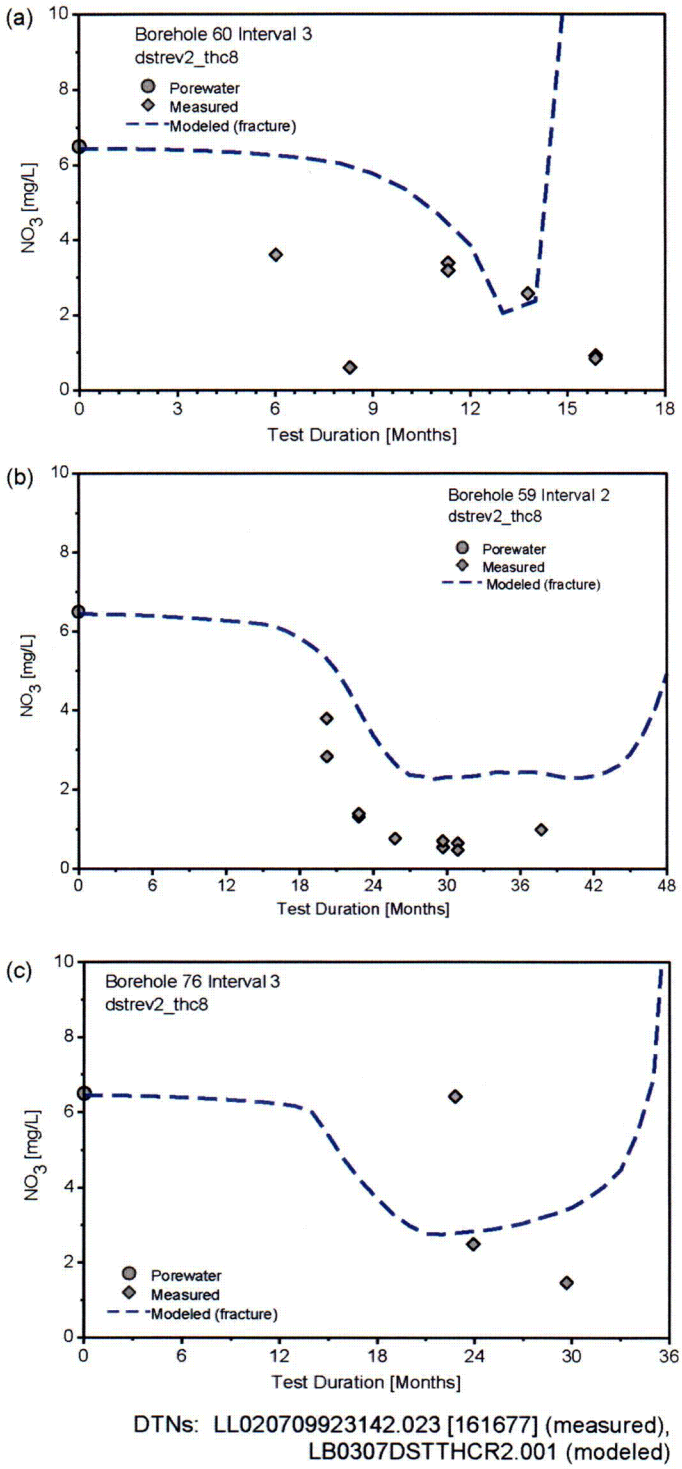

DTNs: LL020709923142.023 [161677] (measured),
LB0307DSTTHCR2.001 (modeled)

Figure 7.1-33. NO_3^- Concentrations (mg/L) in Water Samples Collected from Borehole Intervals (a) 60-3, (b) 59-2, and (c) 76-3 Compared to REV02 Modeled Fracture Water NO_3^- Concentrations

C130

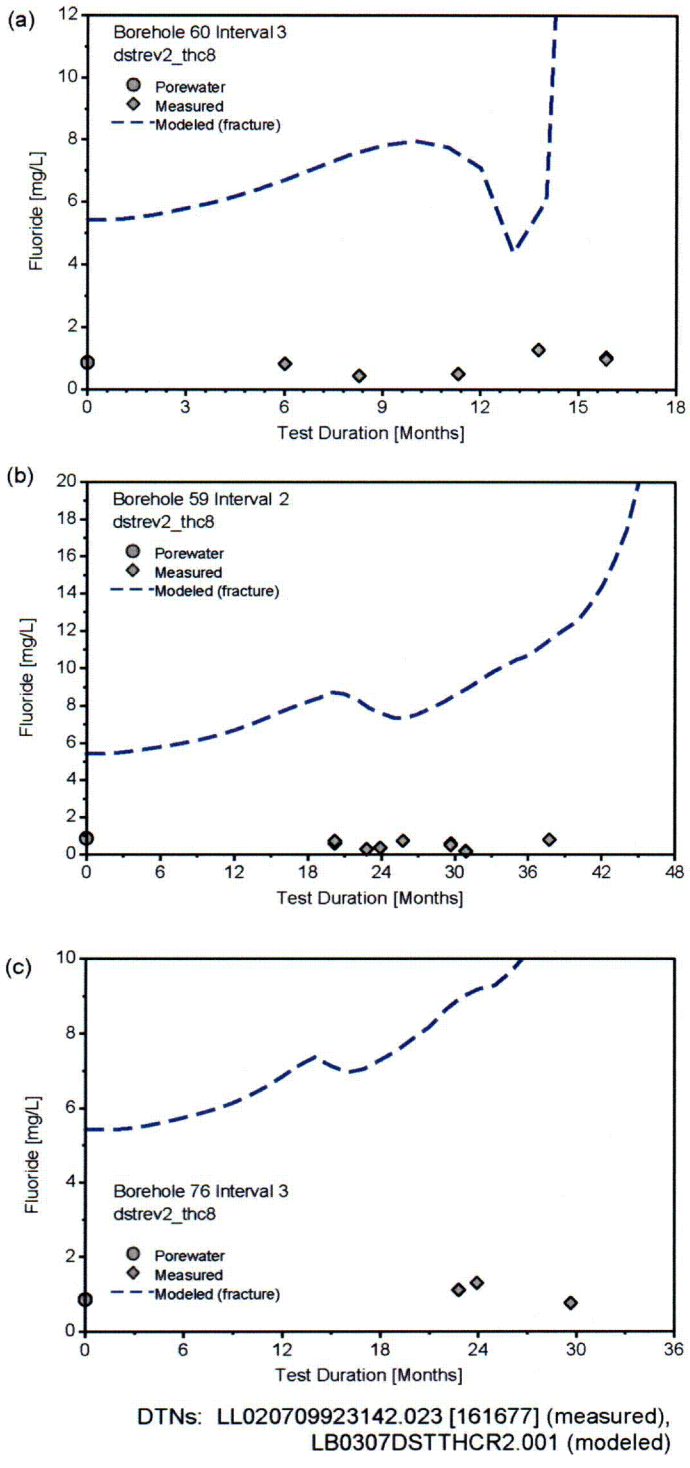

DTNs: LL020709923142.023 [161677] (measured),
LB0307DSTTHCR2.001 (modeled)

Figure 7.1-34. F^- Concentrations (mg/L) in Water Samples Collected from Borehole Intervals (a) 60-3, (b) 59-2, and (c) 76-3 Compared to REV02 Modeled Fracture Water F^- Concentrations

C131

Measured Mg^{2+} concentrations (from Figure 7.1-32) show initial concentrations closer to the pore-water value of about 17 mg/L, and then a considerable drop in all the borehole intervals. Modeled Mg^{2+} concentrations show a similar pattern and are close to the measured concentrations. The sharp drop in the modeled concentrations is related to a combination of dilution from condensate and the precipitation of sepiolite (a Mg-rich sheet silicate). It is not clear whether precipitation of an Mg-rich phase takes place in the boiling zone in the rock, because the extent of dilution of Mg^{2+} is roughly similar to that observed for the conservative species, such as Cl^-. Some Mg^{2+} is likely incorporated into calcite that is precipitated as the condensate water above the heaters drains down and boils, although this may have a minimal effect on Mg^{2+} concentrations. The thermodynamic model for calcite does not include Mg^{2+}, and therefore, another Mg-bearing phase (i.e., sepiolite) take up some of the Mg^{2+}. Most samples fall within an order of magnitude of the model results, thus meeting the validation requirements.

Nitrate (NO_3^-) was added to the list of modeled species for the REV02 simulation, owing to its importance for the evolution of final salt compositions in potential seepage waters. Nitrate is highly soluble, and there are no nitrate minerals initially present in the tuff. The pore water has somewhat more variable nitrate concentrations compared to Cl^- and SO_4^{2-}. The greater variability in pore-water concentrations may be a result of biologically mediated nitrogen reduction, possibly after sample collection. Measured and modeled nitrate concentrations are shown in Figure 7.1-33. Concentrations measured in waters collected from the hydrology boreholes are almost all lower than those from the pore water, showing a similar pattern as Cl^- and SO_4^{2-}. This finding suggests that over the time scale of the experiment, nitrate acts as a conservative species and may not have been affected significantly by biological activity in the rock. REV02 modeled concentrations capture the measured pattern of nitrate concentrations quite well, although the dilution effect is not as strong; this effect is similar to that seen for most other weakly reactive or nonreactive species. Model validation requirements for NO_3^- were met, both in terms of the trend and range of values (except for a few samples).

Fluorite was added to the initial mineral assemblage for the REV02 simulations. Fluorite is observed sporadically in the Yucca Mountain tuffs, and fluoride concentrations should reflect the presence of this mineral. However, fluoride concentrations in the pore water measured around the DST (see Table 7.1-3) are less than 1 mg/L, much lower than the equilibrium solubility of fluorite (around 4-5 mg/L at ambient temperatures). In addition, almost all waters from the hydrology boreholes have measured fluoride concentrations of around 1 mg/L or less, with only one sample at about 4 mg/L. The measured values are shown in Figure 7.1-34 for borehole intervals 59-2, 60-3, and 76-3, compared to the REV02 model results. The modeled fluoride concentrations quickly rise from the initial concentration of less than 1 mg/L to several mg/L, eventually attaining much higher values as increasing temperatures result in much higher fluorite solubility. The increase is also related to the fast dissolution rate of fluorite. Thus, simulations using the REV01 mineral assemblage, without fluorite as a initial mineral phase, capture the change in fluoride concentrations more closely around the DST than the REV02 simulation results. Even though the REV02 model results do not capture the trend in the fluoride concentrations, many of these samples meet the validation requirement for an order-of-magnitude deviation. They also bound the upper limit for the repository units and exemplify the sensitivity of the model to the initial starting conditions.

7.1.12 Mineralogical Changes

As the last few sections have documented, marked changes have taken place in the water and gas chemistry in the DST, owing to thermal-hydrological processes as well as mineral-water-gas reactions. The total amount of minerals precipitated or dissolved, though, may be exceedingly small, even though the effect on the water composition is quite strong. The strong effect on the water composition is related to the water/rock ratio, which is very low in the unsaturated low-porosity fractured tuff. The system is also characterized by an exceedingly low percolation flux of only a few millimeters per year or less, and therefore the ambient water has a long residence time. This section documents the predicted changes in mineralogy over the heating phase of the DST and compares the results to a few measurements made from *in situ* sidewall core samples obtained from above-boiling zones. First, REV01 results are discussed, for which no measurements were available, although they act as a prediction because they were performed prior to the measurements. Following the discussion of the REV01 results, REV02 simulated changes in mineral abundances are compared to the sidewall core samples.

Although calcite is not a major phase in the tuffs at Yucca Mountain, its rapid reaction rate, pH sensitivity, strong effect on pH, and presence almost entirely in fracture coatings make it an important mineral phase. REV01 predicted changes in calcite volume percent in fractures after three years of heating are shown in Figure 7.1-35. The simulated changes in calcite abundances show a well-defined region of precipitation in the fractures above and to the margins of the Heated Drift and wing heaters. Strong dissolution is evident below the wing heaters, especially in the drainage zones. Precipitation in the matrix is driven mainly by increasing temperature and pH, whereas in the fractures there is continuous boiling of condensate waters as they drain back to the heat source from the overlying condensation zone. These waters pick up Ca^{2+} through interaction with calcite and from mixing of ambient fracture pore water. The continuous process of condensate formation and drainage leads to a well-defined zone of calcite precipitation in the fractures above the heaters. The results are also consistent with the decrease in Ca^{2+} seen in the condensate waters over time (Table 7.1-3, see also Section 7.1.11.2).

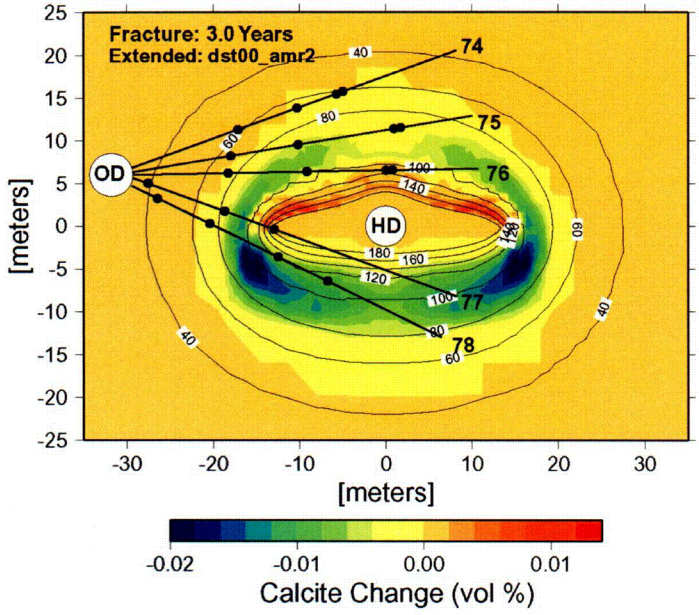

DTN: LB0011DSTTHCR1.002 [161282]

NOTE: Modeled temperature contours are overlain, as well as boreholes and approximate locations of temperature sensors.

Figure 7.1-35. Modeled (REV01) Volume Percent Change in Calcite in Fractures after 3 Years of Heating

Areas of modeled amorphous silica precipitation are shown in Figure 7.1-36 for the extended system (cc kin). Silica concentrations are closest to measured values (Figure 7.1-26) in the extended system, and therefore amounts of amorphous silica precipitated should be closer to those in the rock than the amounts produced by the base-case system model simulations. Like calcite, amorphous silica precipitation is concentrated in the reflux zones above the heaters. However, because silica phases have increased solubility at higher temperatures, the zone of amorphous silica precipitation is confined to regions where the temperatures are at or above boiling and evaporation was the primary mechanism for mineral precipitation. Although the volumetric percentage of amorphous silica that has precipitated is small, the greatest amount of precipitation occurs at the outer edge of the wing heaters (where flow is focused into boiling regions).

C132

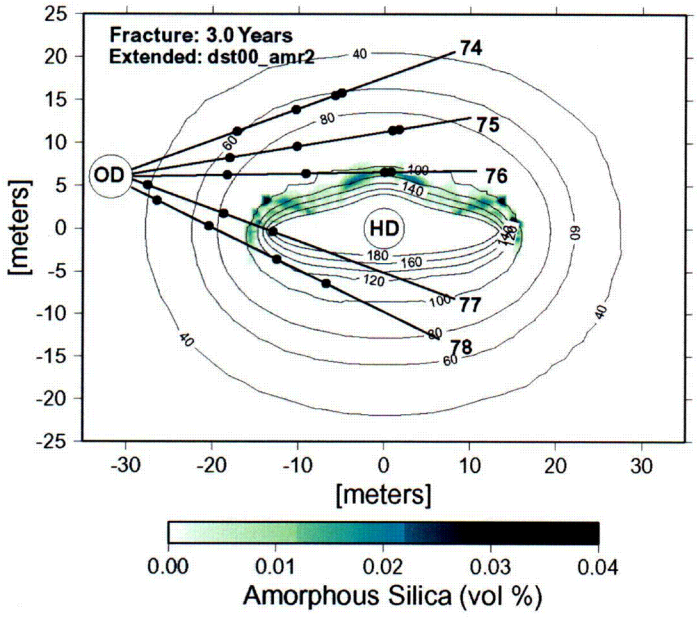

DTN: LB0011DSTTHCR1.002 [161282]

NOTE: Modeled temperature contours are overlain, as well as boreholes and approximate locations of temperature sensors.

Figure 7.1-36. Modeled (REV01) Volume Percent Amorphous Silica in Fractures after 3 Years of Heating

Since the last revision of this Model Report, a series of small core samples was analyzed for evidence of mineral alteration during the heating phase of the DST. The first set of samples was obtained in November 2000 by sidewall coring of fractures in "chemistry" boreholes 53 and 54, which were originally designed for water sampling. However, the SEAMIST pad system employed in those boreholes failed to provide uncontaminated water samples owing to the engineering materials in the boreholes and the unknown compositions of the pads. The collection and analyses of the rock samples are documented in BSC (2002 [160771], Section 6.3.4.3). Chemical analyses, identification, and description of mineral alteration products for a few of the samples are given in DTN: LA0201SL831225.001 [158426]. Because only a small portion of the core has been analyzed and only a few results are available, the comparisons to model results are limited. The data submitted represent observations and analyses from two locations taken about 1 m apart in an above-boiling region above the heaters.

Calcite, amorphous silica, and a calcium sulfate phase (tentatively identified as gypsum) are the only phases in these samples identified so far as products of the processes taking place during the DST (DTN: LA0201SL831225.001 [158426]). Amorphous silica was common in both samples, whereas calcite and gypsum were only described from the sample further into the above-boiling zone (the other sample was from the outer edge). Although anhydrite is thermodynamically more stable than gypsum under the conditions of the DST, gypsum was observed in analyses of borehole surfaces from the Single Heater Test (DTN: LA0009SL831151.001 [153485]). On the basis of this identification, the calcium sulfate phase observed in the DST sidewall core samples was considered to be gypsum (BSC 2002 [160771], Section 6.3.4.3).

C133

From these descriptions, amorphous silica was the dominant phase precipitated during boiling, with much lesser amounts of calcite and gypsum. Amorphous silica appears as glassy coatings covering larger areas of the surface, commonly in the form of thin curled sheets and fine tubules. Calcite typically is found as scattered, small late-stage mounds, with gypsum as very late-formed scattered crystals on top of other phases. The actual percentage of mineral precipitates in the fracture system could not be determined from this type of localized analysis. Some of the silica coatings were approximately 10–20 μm thick, with discrete gypsum crystals up to 80 μm long. Given a uniform 10 μm thick layer of mineral precipitates on one side of all fractures, with a hypothetical range in fracture aperture of 100 to 1,000 μm, the proportion of fracture volume filled would range from 1 to 10%. Because many of the coatings are much less than 10 μm thick and do not cover all areas of every fracture, the volume filled is likely to be less than 1%.

Figures 7.1-37 through 7.1-39 show the REV02 modeled distributions of calcite, amorphous silica, and gypsum in the DST at the time the samples were collected. This time (35 months) is nearly the same as the three-year REV01 results presented above, so the comparison of the different model results can also be made. The location of borehole 54 is plotted, as well as the sites where the mineral was observed in a sidewall core sample. The modeled distributions of other, much more minor phases are not shown, because it is not possible yet to validate their abundances.

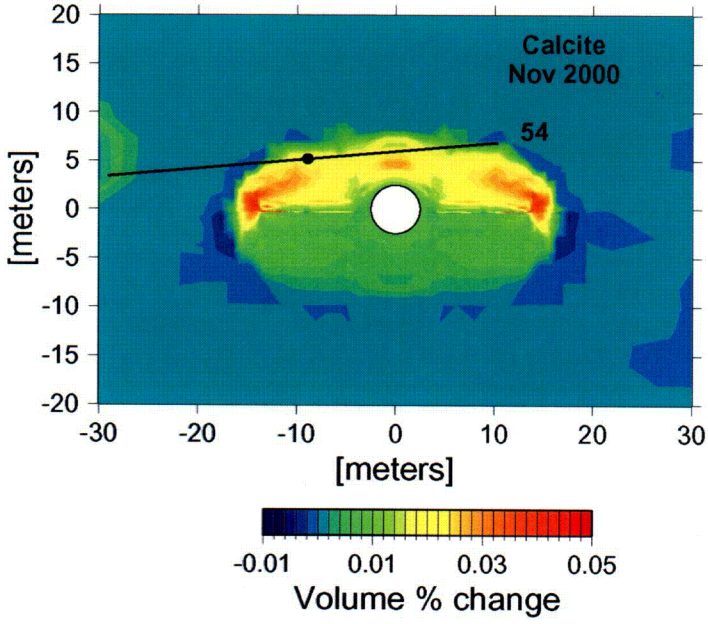

DTNs: LB0307DSTTHCR2.001 (modeled),
LA0201SL831225.001 [158426] (measured)

NOTE: Chemistry borehole 54 is shown, with location of observed calcite (filled circle) formed during DST.

Figure 7.1-37. Modeled Volume Percent Change in Calcite in Fractures as of November 2000 (35 Months of Heating)

C134

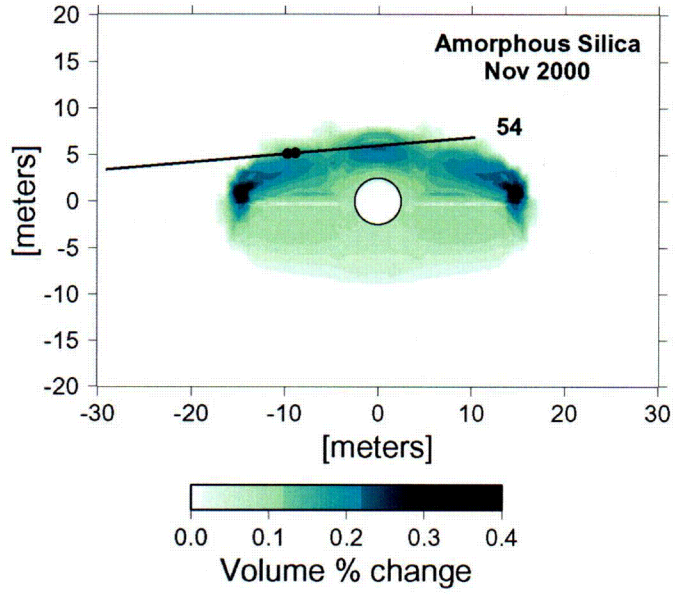

DTNs: LB0307DSTTHCR2.001 (modeled),
LA0201SL831225.001 [158426] (measured)

NOTE: Chemistry borehole 54 is shown, with location of observed amorphous silica (filled circle) formed during DST.

Figure 7.1-38. Modeled Volume Percent Amorphous Silica in Fractures as of November 2000 (35 Months of Heating)

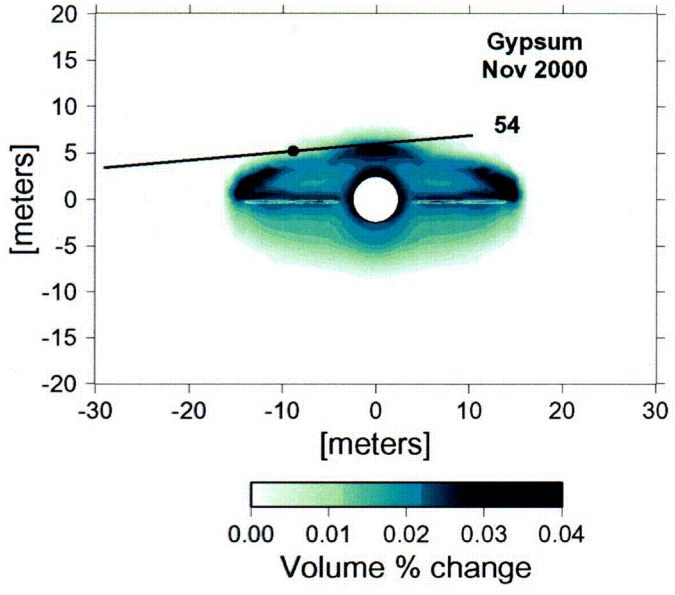

DTNs: LB0307DSTTHCR2.001 (modeled),
LA0201SL831225.001 [158426] (measured)

NOTE: Chemistry borehole 54 is shown, with location of observed gypsum (filled circle) formed during DST.

Figure 7.1-39. Modeled Volume Percent Gypsum in Fractures as of November 2000 (35 Months of Heating)

C135

The modeled distribution of calcite in the REV02 simulation (Figure 7.1-37) is similar to the REV01 results (Figure 7.1-35), but calcite abundances in the precipitation zone above the heaters are higher. This increase in calcite precipitation is primarily a result of an improved mass-conservation formulation for mineral precipitation at the boiling front that was implemented in TOUGHREACT V3.0 (LBNL 2002 [161256]). Another less important factor is the somewhat lower fracture porosity in the REV02 hydrological property set. Although calcite dissolution appears to be minor, it is similar to that presented in the REV01 simulation. It is, however, volumetrically less than precipitation in the REV02 simulation. The location of modeled calcite precipitation matches the location of observed calcite in the sidewall core sample.

Like calcite, the modeled distribution of amorphous silica in the REV02 simulation (Figure 7.1-37) is similar to the REV01 results (Figure 7.1-35), but the abundances in the precipitation zone above the heaters are higher. This increase in amorphous silica precipitation is mainly a combined effect of the much higher aqueous silica concentrations in the REV02 simulated water compositions, which are much closer to measured values, (see Figure 7.1-27) and the improved mass conservation formulation in TOUGHREACT V3.0 (LBNL 2002 [161256]). The net result is an increase of about a factor of ten in the maximum volume change in amorphous silica. The maximum amount of amorphous silica precipitated is about 0.4% after 3 years and less than about 1% for the entire duration of the DST. There is also an excellent correspondence in the region of modeled amorphous silica precipitation and the observed amorphous silica in the sidewall core samples from borehole 54. Although the observations of mineral coatings on a few samples cannot be used to judge the total amount of mineral precipitated, the small volumes precipitated in the model are consistent with the generally thin coatings observed.

Precipitation of gypsum is localized to the zones where modeled sulfate concentrations become very high as a result of boiling (Figure 7.1-39). The observed location of gypsum in the sidewall core sample is consistent with the model results, which show this sample to be just within the edge of the modeled zone of precipitation. Further sampling through the center of the boiling zone should help delineate the pattern of mineral precipitation for all the phases.

The observation of significantly greater amorphous silica precipitation compared to calcite and gypsum, with the latter phases occurring in roughly equivalent amounts, is also consistent with the REV02 model results. Although the maximum amount of amorphous silica precipitated is about an order of magnitude greater than calcite, there are not enough samples to determine the spatial distribution of these phases and whether areas exist where the relative proportions differ. One additional borehole has been drilled through the boiling zone, and two others planned, to examine the distribution of mineral alteration and the effects on matrix pore-water composition. These boreholes will allow for a systematic examination of fracture mineral alteration away from the localized TH effects induced by open boreholes. Given that the three observed mineral phases are in the locations predicted by the model simulations, the validation criteria have been met.

7.1.13 Porosity and Permeability Changes

The predicted maximum change in fracture porosity in the REV01 simulations was about 0.1%. Although the simulations were carried out with a feedback between mineral

dissolution/precipitation and porosity, permeability, and capillary pressure changes, the effect on the latter parameters and on fluid flow was negligible. The greatest change took the form of a few-meters-wide zone of decreased porosity a few meters above the Heated Drift and wing heaters.

The predicted amorphous silica abundances are about an order of magnitude greater in the REV02 simulations than in the REV01 simulations (Section 7.1.12). Consequently, fracture porosity changes are expected to be about one order of magnitude higher. Figure 7.1-40 shows the change in fracture porosity after 4 years of heating in the DST. The areas above the Heated Drift and near the edges of the wing heaters show the greatest reduction in fracture porosity, reaching somewhat less than -0.8%. This is nearly a factor of ten greater than in the REV01 simulations. Areas of slight fracture porosity increases in the model results can be found in the outer condensation zones, yet they are not evident in the contour plot.

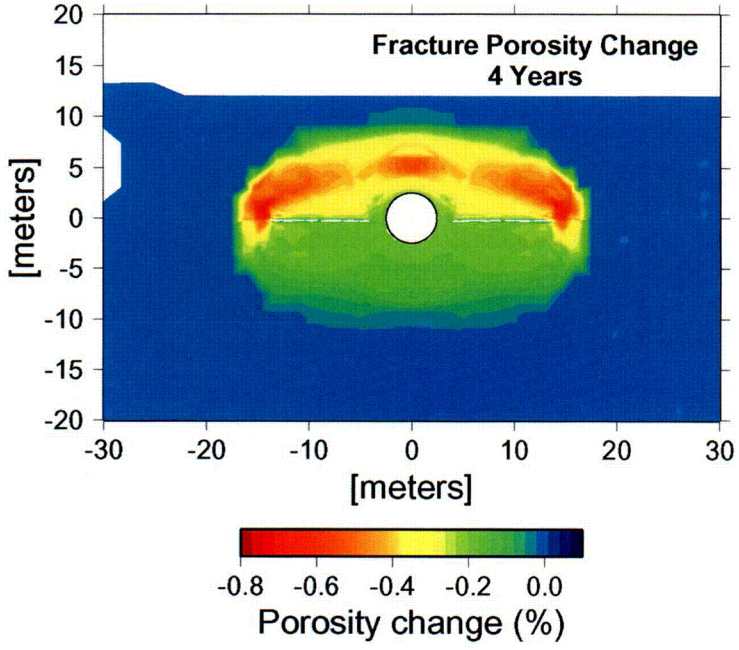

Output-DTN: LB0307DSTTHCR2.001

NOTE: Negative values indicate a net porosity reduction resulting from mineral precipitation, and positive values indicate a net porosity increase resulting from mineral dissolution.

Figure 7.1-40. Change in Fracture Porosity after Four Years of Heating

As discussed in the preceding section, several factors are responsible for the modeled increased mineral volume changes in fractures. The increase in aqueous silica concentrations from the addition of opal as a starting mineral phase, changes in the thermodynamic data, a reduction of the initial fracture porosity to 0.0085 from 0.01, and the improved-mass balance formulation at the boiling front in TOUGHREACT V3.0 (LBNL 2002 [161256]) are all contributing factors.

Changes in matrix porosity after four years of heating are shown in Figure 7.1-41. Reductions in matrix porosity are limited solely to the dryout zone where mineral precipitation accompanied boiling of the *in situ* pore water. Increases in matrix porosity are actually greater than the

C136

reductions and are evident throughout the condensation zones, where imbibition of dilute water must have led to mineral dissolution. Areas of strong fracture drainage around the outer edges of the heated zone apparently led to the highest level of matrix imbibition and mineral dissolution in the matrix. The porosity increase in the matrix is, however, approximately two orders of magnitude less than the porosity decrease in the fractures.

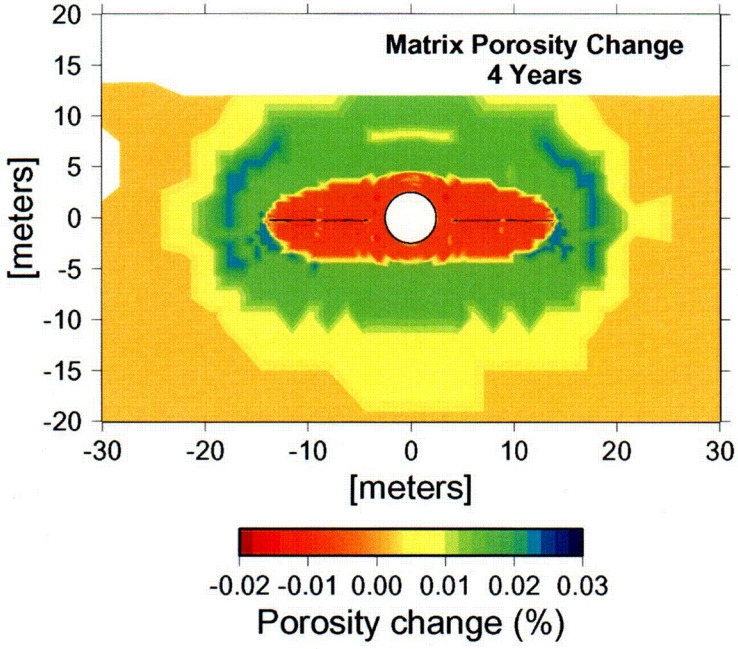

Output-DTN: LB0307DSTTHCR2.001

NOTE: Negative values indicate a net porosity reduction resulting from mineral precipitation, and positive values indicate a net porosity increase resulting from mineral dissolution.

Figure 7.1-41. Change in Matrix Porosity after Four Years of Heating

Fracture permeability changes resulting from mineral precipitation and dissolution are tied to changes in porosity and more directly to fracture aperture changes. Changes in fracture porosity of less than 1% of the original value would have a correspondingly small effect on fracture permeability. These results are consistent with the observations of minimal changes in air permeability during the DST, which have been attributed predominantly to water saturation changes (mostly in the condensation zones, where mineral precipitation is negligible) (BSC 2002 [160771], p. 6.3-15).

7.1.14 Isotopic Compositions of Gases and Water: Model Corroboration Using ^{14}C in CO_2

Gas-phase CO_2 concentrations and stable isotopic ratios ($\delta^{13}C$, $\delta^{18}O$, δD, and ^{14}C) were measured from gases pumped from hydrology boreholes (BSC 2002 [160771], Table 6.3.4.2-1). For the gas-phase compositions, direct comparisons of model results have been made only to CO_2 concentrations. Isotopic ratios of carbon ($\delta^{13}C$), oxygen ($\delta^{18}O$), and hydrogen (δD) are sensitive to fractionation effects between the liquid and gas phases as well as to diffusive fractionation, owing to the differing masses of the isotopes. Thus, they are useful in interrogating

C137

thermal-hydrological transport processes. These fractionation effects are pronounced at lower temperatures, such that the relatively minor extent of water-rock interaction is strongly masked. Thus, they are less useful for directly investigating mineral alteration during the DST.

Relative to the stable carbon isotopes (^{12}C and ^{13}C), carbon-14 (^{14}C) abundances are minimally affected by fractionation because their activities vary over a large range, owing to the geologically short time for the radioactive decay of this species ($t_{1/2} \approx 5{,}000$ years). The virtual lack of ^{14}C in carbonate minerals at Yucca Mountain (because these materials are predominantly tens of thousands to millions of years old) allows for a sensitive indicator of the dissolution of calcite. Fortuitously, ^{14}C activities in the gas phase in the rock, at approximately the level of the Tptpmn unit, are close to 0.5 (fraction modern carbon) for several measurements done in different areas (BSC 2002 [160247], Table 20 (p. I-39), Figure 44 (p. II-46)). The convention "fraction modern carbon" refers to the activity of ^{14}C prior to atmospheric testing of nuclear weapons. Thus, the present-day activity of atmospheric ^{14}C is somewhat greater than one, because of the addition of ^{14}C through weapons testing. In the subsurface at Yucca Mountain, therefore, any addition of atmospheric CO_2 to the rock gas will drive its ^{14}C activity from about 0.5 towards 1.0, whereas dissolution of calcite will drive the activity to close to zero.

Measured ^{14}C activities in CO_2 from several hydrology borehole intervals (BH74-3, BH75-3, BH76-3, and BH78-3) are shown in Figure 7.1-42 over much of the heating phase of the DST. Unfortunately, an initial, unperturbed gas sample was not analyzed; however, the earliest samples collected had ratios around 0.4. All of the zones show a significant drop-off over time to values below 0.2 and several to around 0.1 or less. By projecting the trajectories of these early slopes back to time zero, the zones appear to converge to an initial activity close to 0.5. Note that all of the samples analyzed from rock gas (over 40 measurements) had activities below 0.5. Two measurements of gas from the Heated Drift (taken after about 12 and 44 months) were also analyzed and show nearly identical values of about 0.98, which is almost entirely atmospheric in composition. Thus, it is clear that the gas in the Heated Drift is exchanging freely with the atmosphere, even though the pore water in the rock is generating abundant CO_2 with low ^{14}C activities.

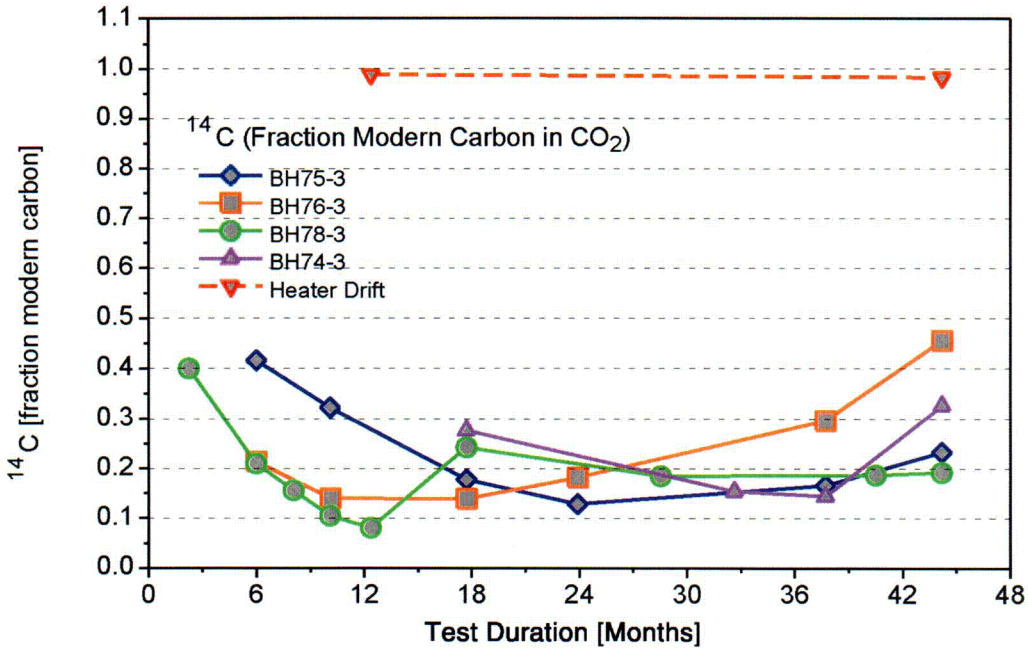

Source: BSC 2002 [160771], Table 6.3.4.2-1.

NOTE: Two samples collected from the Heater Drift were also analyzed.

Figure 7.1-42. Measured Activities of ^{14}C (Expressed as a Fraction of Modern Carbon) in CO_2 from Gas Collected in Several Hydrology Boreholes over Most of the Heating Phase of the DST

It can be concluded from these data that little atmospheric CO_2 has affected the CO_2 in the rock gas. Although atmospheric gas has undoubtedly been introduced into the system through gas-permeability testing and drilling, the relatively low CO_2 concentration in atmospheric air ($\approx$ 400 ppmv) compared to the ambient rock gas ($\approx$ 1,000 ppmv) and to the large concentrations generated during heating ($>$ 10,000 ppmv) make atmospheric contamination of CO_2 more difficult.

The strong drop-off of ^{14}C in the gas over time is caused primarily by the dissolution of calcite having little or no ^{14}C. The pore water could also be heterogeneous with respect to ^{14}C, the interiors of the matrix blocks having "older" water than the exterior. The latter explanation, though, is implausible, owing to the rapid diffusivity of CO_2 in the gas phase in the unsaturated matrix and the rapid equilibration of CO_2 with bicarbonate in the aqueous phase. Furthermore, this possibility is not supported by the gradual return in all of the measured borehole intervals to higher ^{14}C activities. Finally, ^{14}C activities as low as 0.08 have not been observed in the gas phase in the UZ at Yucca Mountain and would imply isolated water with ages of close to 15,000 years.

Another aspect to the trend in ^{14}C activities can be found by examining their relation to the CO_2 in the gas phase. The abundance of ^{14}C in the gas is governed by the equilibrium between HCO_3^- in the water and CO_2 in the gas phase. Under closed conditions, the gas should be in equilibrium with the water. This is assumed in modeling the CO_2 concentrations in the DST, where there is excellent correspondence between modeled and measured values. The overall trend in ^{14}C activities seen in Figure 7.1-42 is inversely related to the changes in CO_2 concentrations

C138

observed in these intervals. The timing of the peak in CO_2 concentration and the low in ^{14}C activity is also very close (see Figure 7.1-11). A comparison of measured CO_2 (corrected for water-vapor removal) and ^{14}C is shown for three borehole intervals in Figure 7.1-43. It is apparent that at the highest CO_2 concentrations reached in each zone, the ^{14}C activities are also among the lowest.

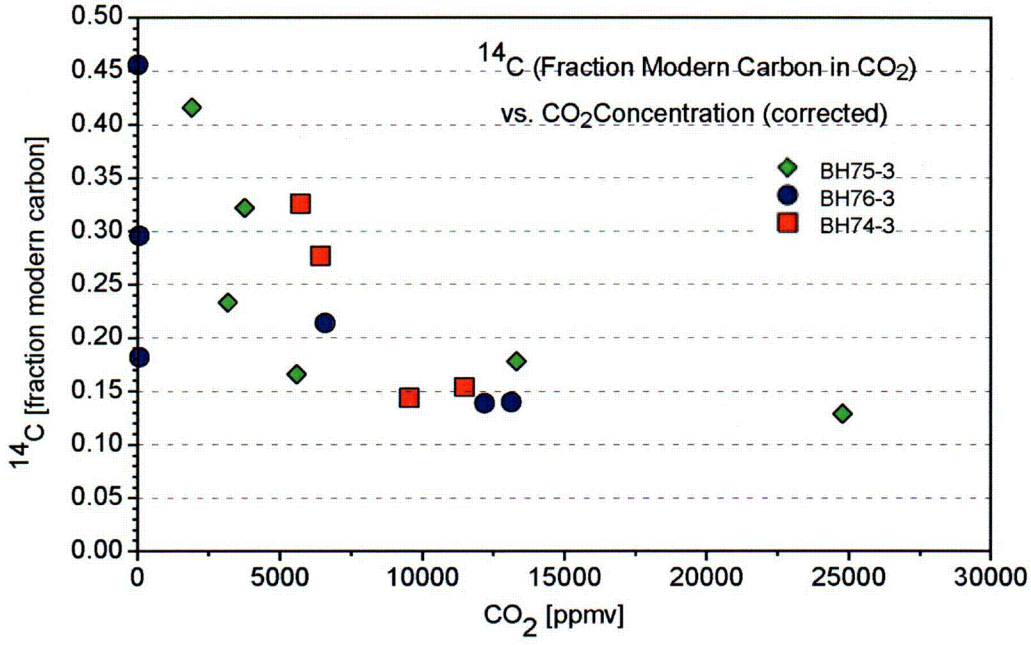

Source: BSC 2002 [160771], Table 6.3.4.2-1.

Figure 7.1-43. Measured Activities of ^{14}C (Expressed as a Fraction of Modern Carbon) Compared to Measured CO_2 (Corrected for Water Vapor Removal) from Gas Collected in Some Hydrology Boreholes over Most of the Heating Phase of the DST

The peak in CO_2 concentrations observed in the model results, and in the measured values, takes place at temperatures of close to 60°C, well below boiling and prior to the dilution of the gas phase by significant quantities of water vapor. This temperature region is characterized by some vapor condensation (Figure 7.1-5), a lowering of pH (Figure 7.1-14), and calcite dissolution (Figures 7.1-35 and 7.1-37) in the model simulations. Therefore, the trend to low ^{14}C activities in the areas where calcite is predicted to dissolve is consistent with the model results and with the aqueous- and gas-phase chemical data that have been used to validate the model.

C139